UNIVERSITY OF BIRMINGHAM

Feature Extraction from Reconfigurable Antenna

Author:
Yuming BAI

Supervisor:
Prof. Peter GARDNER

A thesis submitted to
College of Engineering and Physical Sciences,
Universityof Birmingham,
for the degree of Doctor of Philosophy

Department of Electronic, Electrical, & System Engineering,
University of Birmingham, Edgbaston,
Birmingham, B15 2TT, UK.

June 16, 2022

Abstract

The work in this thesis concerns generic surrogate modelling techniques for a reconfigurable antenna based on any mechanisms. To make sure of the universality of the generic surrogate model, several new perspectives: related to field operating and circuit operating; feature extraction from the antenna; and reconfigurable antenna, are proposed to be a foundation and to provide guidance for the subsequent theory and applications. Additionally, the mathematical derivation of non-linear function fitting and the corresponding equivalent circuit/network is presented as the basic theory. Furthermore, three applications to corresponding antennas are presented to demonstrate the feasibility and effectiveness of the surrogate modelling techniques. Specifically, the first application contains two traditional antennas. They are a chassis antenna with two resonators and a band-notched ultra-wideband pyramidal monopole antenna. The second application to a frequency reconfigurable UWB antenna with a tunable notched-band is to obtain a data-driven surrogate model. The third application to the same reconfigurable UWB antenna is to obtain a physics-based surrogate model. In these applications, the surrogate modelling approach has many advantages. The approach is reliable and efficient. It has the flexibility for widespread use in many complicated scenarios, because of its elastic order and its adaptable weighting factor. It has fewer extracted parameters with better precision.

These surrogate modelling techniques could be applied to integrate the reconfigurable antenna into a communication system. Furthermore, the approach could also be helpful in the microwave area auto design. Primarily, it could combine artificial intelligence (AI) algorithms to realize future wireless communication such as Smart Antenna, Software Defined Radio and Cognitive Radio.

The novelty and contributions are summarized as follows: (1) This work proposes a completed systematic approach, including fundamental principles, rigorous mathematical derivation and feasible application verification. (2) The approach has the property of generalizability to cover all frequency reconfigurable antennas. (3) As a post-processing approach, it can convert the discrete data of CAD simulation and VNA measurement to a surrogate model with analytical function and equivalent circuit. (4) Some traditional antennas and reconfigurable antennas are taken as examples to demonstrate that the approach is feasible, effective, and precise. (5) The approach has the flexible ability to adapt to strict requirements and complicated scenarios.

Acknowledgements

First of all, my first debt of gratitude must go to my supervisor Professor Peter Gardner. He patiently provided the vision, encouragement and advice necessary for me to proceed through the doctoral program and complete my thesis.

I also want to express my deep gratitude to my brilliant colleagues, Dr Long Shen, Dr Peter Kihogo, Dr Muhammad Saqib Rabbani, and Dr Thomas Thatapudi. They have been very supportive and generous in sharing their knowledge.

I am very grateful to Mr Alan Yates for providing all the technical support and teaching me how to use many kinds of equipment.

Special thanks to Mr John Ashford, Mr Wencheng Li, Dr Yang Xiao, and Dr Xiaofei Ren for their excellent help and friendship. With all their support, encouragement, and help, my study life at the University of Birmingham became happy, especially during the tough time after Covid-19.

Last but not least, I would like to thank my beloved parents for their endless love, support, encouragement, understanding and sacrifices.

Publications

Published

1. **Y. Bai** and P. Gardner, "Rational fitting with weighted iteration (RFWI) with application to chassis antenna," *2021 51st European Microwave Conference (EuMC)*, pp. 502-505, 2022.

In Press

1. **Y. Bai** and P. Gardner, "Rational fitting with weighted iteration (RFWI) with application to band-notched UWB pyramidal antenna," *2021 CIE International Conference on Radar (CIE Radar 2021)*, in press.

Submitted

1. **Y. Ba**i and P. Gardner, "A Surrogate Modeling Approach for Frequency Reconfigurable Antennas," submitted to *IEEE Antennas and Wireless Propagation Letters*, 2022.

2. **Y. Ba**i and P. Gardner, "Surrogate model based on network analysis for frequency reconfigurable antenna with electronic loading," submitted to *IEEE Transactions on Antennas and Propagation*, 2022.

Contents

List of Figures

List of Tables

List of Abbreviations

AI	**A**rtificial **I**ntelligence
API	**A**pplication **P**rogram **I**nterface
ASM	**A**ggressive **S**pace **M**apping
BEM	**B**oundary **E**lement **M**ethod
BST	**B**arium **S**trontium **T**itanate
CAD	**C**omputer-**A**ided **D**esign
CCCS	**C**urrent-**C**ontrolled **C**urrent **S**ource
CF	**C**ontinued **F**raction
CR	**C**ognitive **R**adio
CST	**C**omputer **S**imulation **T**echnologies
DAE	**D**ifferential **A**lgebraic **E**quation
DTM	**D**irectly **T**ranslated **M**ethod
EM	**E**lectro **M**agnetic
EMC	**E**lectro **M**agnetic **C**ompatibility
FCC	**F**ederal **C**ommunication **C**ommission
FDTD	**F**inite-**D**ifference **T**ime-**D**omain
FE	**F**inite **E**lement
FET	**F**ield **E**ffect **T**ransistor
FITD	**F**inite-**I**ntegration **T**ime-**D**omain
IPMC	**I**onic **P**olymer **M**etal **C**omposite
KCL	**K**irchhoff's **C**urrent **L**aw
KVL	**K**irchhoff's **V**oltage **L**aw
MEMS	**M**icro-**E**lectro **M**echanical **S**ystems
MIMO	**M**ultiple-**I**nput **M**ultiple-**O**utput
MM	**M**ode-**M**atching
MNA	**M**odified **N**odal **A**nalysis
MoM	**M**ethod **o**f **M**oments
MOR	**M**odel **O**rder **R**eduction
NIC	**N**egative **I**mpedance **C**onverter
ODE	**O**rdinary **D**ifferential **E**quation
OS	**O**perating **S**ystem
PE	**P**arameter **E**xtraction

PFE	**P**artial **F**raction **E**xpansion
RF	**R**adio **F**requency
SA	**S**mart **A**ntenna
SDR	**S**oftware **D**efined **R**adio
SM	**S**pace **M**apping
SM	**S**pectral **M**ethod
TDR	**T**ime-**D**omian **R**eflectometry
TLM	**T**ransmission **L**ine **M**ethod
TRM	**T**ransverse **R**esonant **M**ethod
UWB	**U**ltra-**W**ide**B**and
VCCS	**V**oltage-**C**ontrolled **C**urrent **S**ource
VCVS	**V**oltage-**C**ontrolled **V**oltage **S**ource
VNA	**V**ector **N**etwork **A**nalyzer
VSWR	**V**oltage **S**tanding **W**ave **R**atio

Chapter 1

Introduction

1.1 Background

Two decades ago, pioneer researchers conceived of the future wireless system [1], and many related notions were proposed, such as Cognitive Radio (CR), Software Defined Radio (SDR), Smart Antenna (SA), Reconfigurable Antenna, and Ultra-WideBand (UWB).

A Cognitive Radio (CR) is a wireless system with self-adaptive ability in different conditions. At the system level, Cognitive Radio involves various aspects, as shown in Figure 1.1, including practical sensors, cooperative sensing, enabling algorithms, approaches, and standards [2]. Unfortunately, many related aspects generate an enormous challenge to CR's realization, such as hardware requirements, hidden primary user problems, decision fusion, and security.

Software Defined Radio (SDR) is a technology that fulfilled CR requirements well. Such technology is heavily weighted in favour of the software aspect. Joseph Mitola proposed the term 'Software Radio' in [3], whose final target was communicating with desired operation frequency, impedance bandwidth, modulation and data rate by controlling proper software. In a software framework level description,

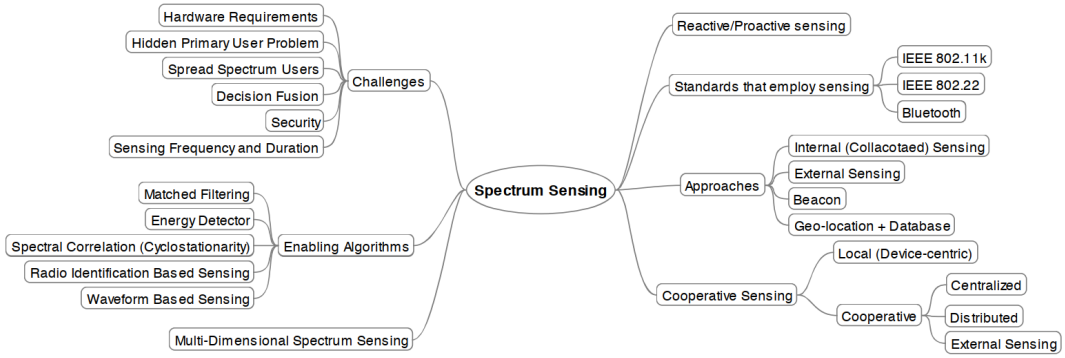

FIGURE 1.1: Various aspects related to Cognitive Radio in [2].

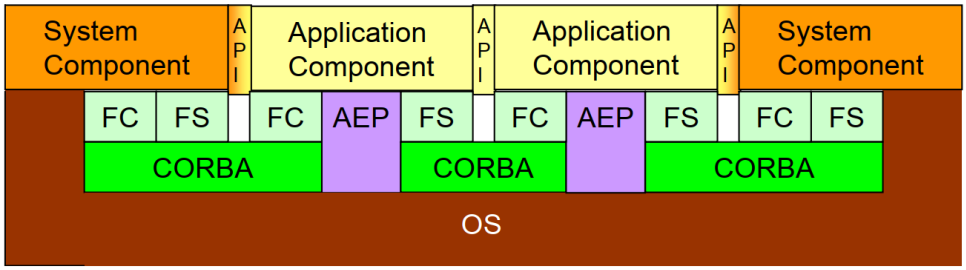

FIGURE 1.2: A visualization frame of Software Defined Radio in [6].

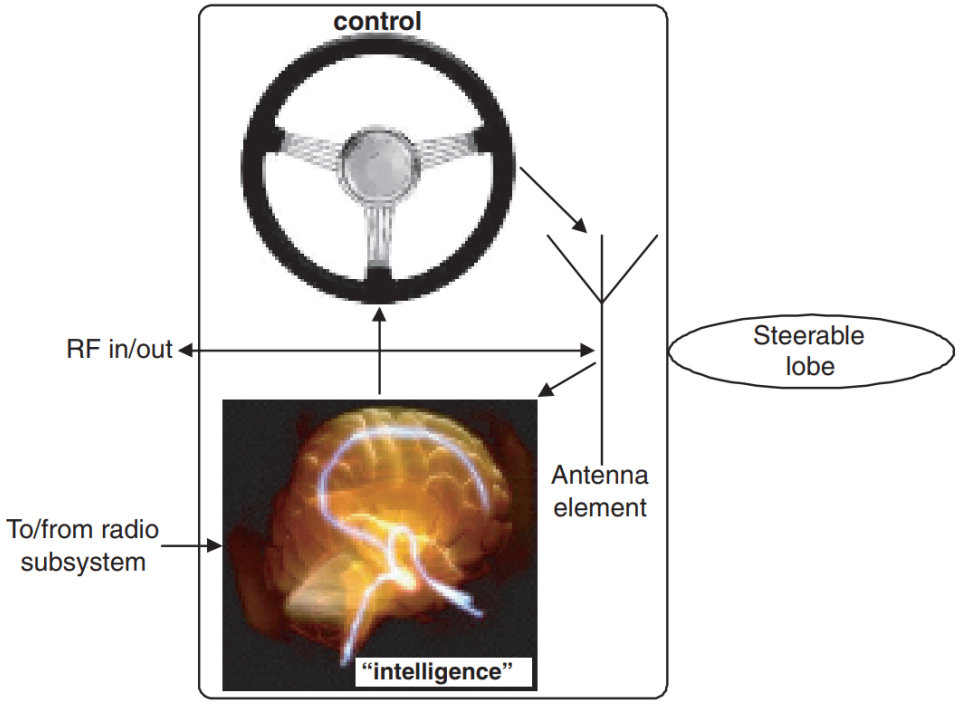

FIGURE 1.3: Principle of a smart antenna system [7].

the concept of SDR features in many related systems, such as Software Based Radio [4], Reconfigurable Radio, Flexible Architecture Radio [5]. Figure 1.2 shows a visualization frame of SDR in [6]. It can be seen that SDR involves Operating System (OS), system components, Application Program Interface (API), and application components.

Smart Antenna (SA) is a leading technology at the physics level to maximize system capacity, improve quality and coverage of network [8], and suppress interference [9]. The principle of the Smart Antenna is illustrated in Figure 1.3. The antenna's radiation pattern can be changed to adapt to the environment. For instance, this ability can avoid directing towards the interference source to improve communication quality, and the tunable pattern can centralize towards the desired direction to reduce power consumption. Of course, the implementation of this functionality depends on not only the reconfigurable ability of antennas and sensors in the hardware aspect, but

also the related algorithms of signal processing to control such antennas and sensors in the software aspect [7].

From a framework-scale perspective, CR is regarded as an extension of the SDR [10], just as the SDR is the extension of the Smart Antenna. Compared with Smart Antenna, both Cognitive Radio and Software Defined Radio are at a system level, and their realization necessarily depends on the development of the front end. Thus, they make requests for antenna design. Especially among such requests, a reconfigurable antenna is the fundamental and significant one desired by all.

A reconfigurable antenna can alter its own electromagnetic properties, including working frequency, impedance bandwidth, polarization, and radiation pattern, in a controlled and reversible manner. The opposite of a reconfigurable antenna is a non-reconfigurable antenna, which is also called a traditional antenna. The reconfigurable antenna can accommodate more complicated environments than the traditional antenna. Thus, antenna reconfiguration offers many advantages in practical application. For instance, in a frequency reconfigurable antenna, several different operating frequency bands can be integrated into a single antenna. Another example is that the pattern reconfigurable antenna can radiate its signal towards the target to reduce the power consumption. Indeed, with the extension of reconfiguration, the applications and the benefits of reconfigurable antennas become more and more. To date, many reconfigurable antennas have been developed within a lot of novel technologies and components in mechanical and material areas. For example, researchers have proposed a reconfigurable frequency antenna with movable metal posts [11], a tunable beam antenna with a simple phase shifter [12], and a reconfigurable microstrip patch antenna on tunable liquid crystal substrate [13]. At the same time, other techniques are utilized, such as Micro-Electro-Mechanical-Systems (MEMS) devices [14]. For the development of reconfigurable antennas, the next stage is to integrate more functionality into one single terminal to fulfil harsh requirements in complicated scenarios. As the essential part of a wireless system, the diversity of reconfigurable antennas provides possibility and convenience for realising CR, SDR, and Smart Antenna [15], [16].

Additionally, Ultra-WideBand (UWB) spectrum has always caught researchers' attention as a communication standard, since the Federal Communication Commission (FCC) declared the frequency spectrum of 3.1-10.6 GHz as UWB communication in 2002 [17]. UWB antennas have the advantages of broad bandwidth, miniaturized electrical size, low cost, low energy consumption and high data rate. Figure 1.4 illustrates the normalized energy consumptions of Bluetooth, UWB, ZigBee, and Wi-Fi, respectively. Among them, the UWB technique shows the lowest power for both transmitting and receiving. Even the normalized energy consumption of UWB

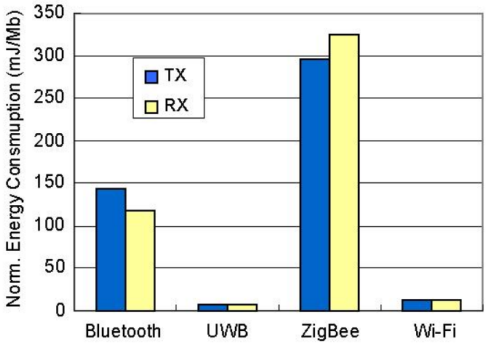

FIGURE 1.4: Comparison of the normalized energy consumption in [19].

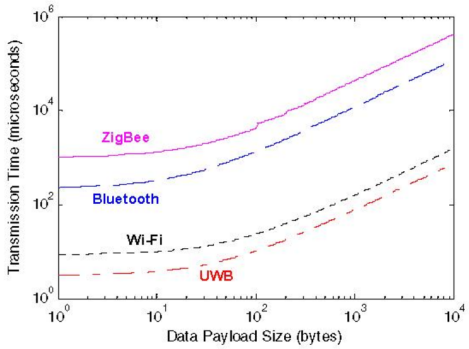

FIGURE 1.5: Comparison of the transmission time versus the data size in [19].

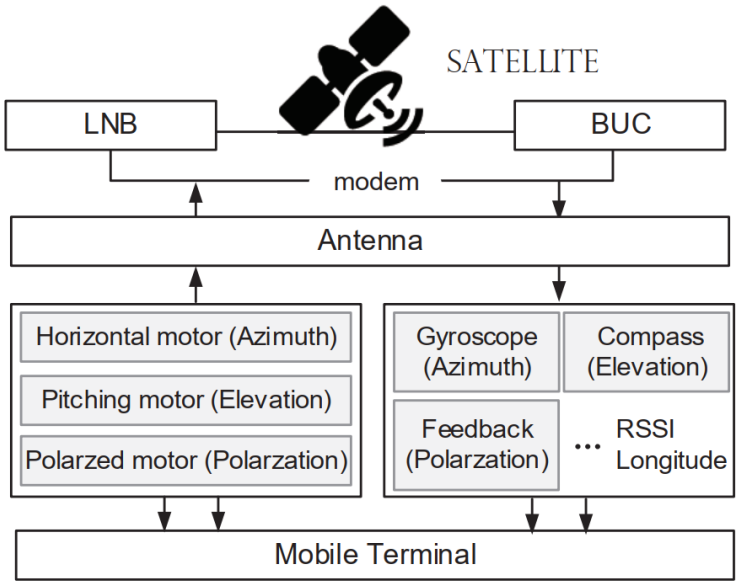

FIGURE 1.6: The AI-based multi-layer network framework of the satellite communication system in [20].

is less than 3% of ZigBee. Figure 1.5 plots the transmission time of 4 popular communication standards in logarithmic coordinate. Compared with ZigBee, Bluetooth and Wi-Fi, the transmission time of the UWB technique is the least with the same data size. Even the transmission time of the UWB is less than 1% of ZigBee. Since such tremendous benefits, UWB antennas are good platforms combined with other techniques, such as UWB antenna with notch-band. [18].

Recently, Artificial Intelligence (AI) has become a new frontier of academic research in many scientific areas. In microwave and radio frequency (RF) areas, there are special issues from *IEEE Transactions on Antennas and Propagation* in 2021 [21] and from *IEEE Transactions on Microwave Theory and Techniques* in 2021 [22]

devoted to such scientific topics, Machine Learning in antenna design, a communication system based on AI. Many successful AI-based applications in communication systems have been proposed, as shown in Figure 1.6. With the development of Computer-Aided Design (CAD) and Vector Network Analyzer (VNA), the antenna design and measurement have been improved dramatically during the past twenty years, so the design and fabrication of traditional antennas do not pose any difficulties. The increasing usage of CAD and VNA results in a new trend of antenna design, based on combination with new techniques from computer algorithms. AI algorithms have widespread potential applications in the microwave area, because of the design dependence on the computer. Moreover, new techniques in AI, such as Deep Learning, may have the capacity to "learn" from pre-existing antennas to optimize further and to realize the auto design in the microwave and RF [23].

1.2 Challenges

Several challenges arise with further research and become a hot topic. Undoubtedly, the successful resolution of such challenges will promote tremendous progress in microwave and communication areas.

1.2.1 Challenges from Ultra-Wide Band

Due to its broad spectrum coverage, the UWB spectrum is easily affected by different interfering frequency bands shown in Figure 1.7. For this issue, the effective solution is to add a notched band in the UWB spectrum to avoid interference from the specific frequency band. For the interference from multiple frequencies simultaneously, the UWB antennas within dual, triple, quadruple, and quintuple notched-bands are

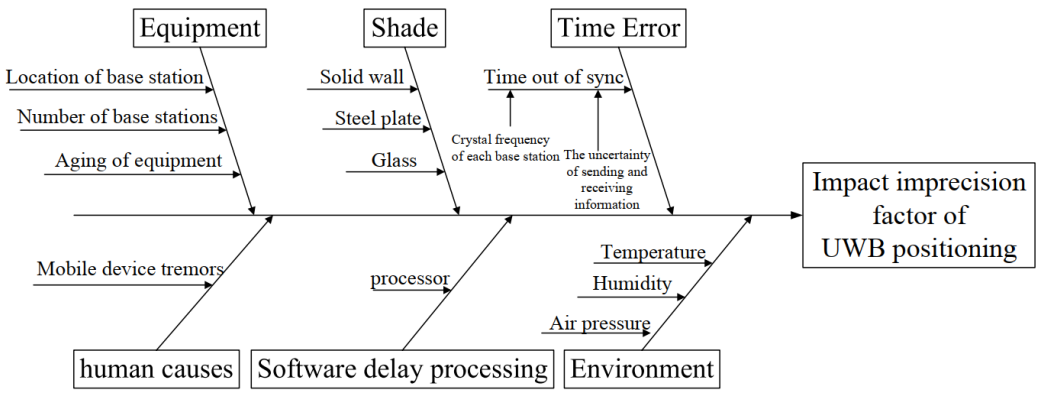

FIGURE 1.7: A fishbone diagram model of the relationship between UWB positioning accuracy in [24].

proposed [25], [26]. From the perspective of filter, this solution is also regarded as integrating the filtering functionality into the original UWB antenna [27]. The final response of the filtering UWB antenna is also the UWB spectrum with a notched band. The interference problem can be solved well by integrating notched-band or filtering functionality into the UWB antenna, but a new challenge arises. The system response of a notched-band UWB antenna is a broad working band except for one or several narrow stop-band(s). Therefore, it requires that the surrogate modelling technique must be able to accurately recognize the very narrow notched band from the UWB spectrum. That is the new challenge from the UWB antenna with a notched band.

1.2.2 Challenges from Reconfigurable Antenna

Many reconfigurable antennas based on various mechanisms provide more choices. Simultaneously, the diversity of their mechanisms brings a tremendous challenge to integrating the reconfigurable antennas into a communication system. The solution is to find an efficient generic description that could cover all kinds of reconfigurations, so the describable diversity will no longer be a problem. However, the generic description is difficult to find, because it is not just applicable to the electromagnetic area but also requires involving all possible physical areas, such as mechanical structure and material physics.

In order to describe a reconfigurable antenna, a surrogate modelling method is the best solution. The surrogate model is a simple model extracted from the complicated simulation model. Thus, it can replace the expensive original simulation model by approximating the input variables and the output responses [28]. There have been many successful surrogate modeling techniques for non-reconfigurable antennas, such as Genetic Algorithm [29], Vector Fitting [30], Passive Macromodeling [31], and Space Mapping [32], [33] in Figure 1.8. However, these surrogate models are unavailable for reconfigurable antennas. Thus, a generic description based on the surrogate modelling method is needed.

Among the surrogate models, an analytical function in mathematics is the best method to substitute the original reconfigurable antenna. The analytical function can continuously describe and quantify the antenna properties, such as antenna responses, spatial radiation pattern, and polarization. Additionally, the analytical function has fewer extracted features than other types of surrogate models. The extracted features/parameters could rebuild the antenna properties. Therefore, fewer extracted

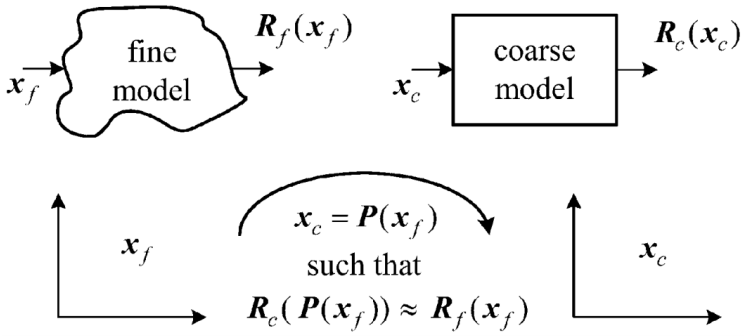

FIGURE 1.8: Illustration of the fundamental notation of Space Mapping Method in [34].

features/parameters mean higher model efficiency. The direct method to get the analytical function is to fit the discrete data from Computer-Aided Design (CAD) simulation or Vector Network Analyzer (VNA) measurement. The result of the fitting process is a fitting function, which is an analytical function to approximate the antenna property. During the process of fitting the system response to obtain the completed analytical function of frequency, the complex number field property of the system responses needs to be considered. If only considering the response magnitude, the outcome without the phase information is meaningless for the subsequent analysis and application. On this basis of the analytical function, the transforms and operations in mathematics are available, so it is possible to integrate the reconfigurable parameters into the analytical function as the input variables to obtain a surrogate model of the reconfigurable antenna.

The whole process, including an immense amount of details, is a systematic model, which is the challenge.

1.3 Objective

The primary object of this work is fitting analytical functions, extracting features from a complicated reconfigurable antenna, and obtaining a proper surrogate model to overcome the challenges described above. The study is classified into several areas as follows:

1. Mathematical derivation of function fitting and parameter extraction from system response of electromagnetic devices.

2. Function fitting and parameter extraction for traditional antenna, demonstrated by the applications to a chassis antenna and a UWB antenna with fixed notched-band.

3. Equivalent circuit and network analysis after obtaining the analytical rational function.

4. Function fitting and parameter extraction for reconfigurable antenna and obtaining the corresponding surrogate model, revealed by the application to a reconfigurable UWB pyramidal monopole antenna with tunable notched-band.

5. A physics-based surrogate modelling approach of reconfigurable antenna combining network analysis method, verified by a reconfigurable UWB antenna with tunable notched-band.

1.4 Novelty and Contribution

The novelty and contributions of this work are summarized as follows:

1. This work proposes a completed systematic approach, including fundamental principles, rigorous mathematical derivation and feasible application verification.

2. The approach has the property of generalizability to cover all frequency reconfigurable antennas.

3. As a post-processing approach, it can convert the discrete data of CAD simulation and VNA measurement to a surrogate model with analytical function and equivalent circuit.

4. Some traditional antennas and reconfigurable antennas are taken as examples to demonstrate that the approach is feasible, effective, and precise.

5. The approach has the flexible ability to adapt to strict requirements and complicated scenarios.

1.5 Thesis Outline

The thesis consists of nine chapters. A brief introduction to the background, challenges, objective, novelty and thesis layout is presented in Chapter 1.

In Chapter 2, the reviewed literature about UWB antennas, reconfigurable antennas and surrogate models are reported and summarised.

In Chapter 3, some new perspectives of field, circuit, feature extraction and reconfigurable antenna are discussed. Such perspectives are guidelines for this research work.

In Chapter 4, the mathematical derivation of precise rational function fitting specifically used in microwave and RF is presented.

In Chapter 5, several methods converting rational function to the equivalent circuit are proposed. An approach combining rational function fitting with the network analysis method is also presented to obtain an equivalent network from scattering parameters of the multi-port system.

In Chapter 6, two applications of parameter extraction from traditional antennas are performed. One is a chassis antenna with two coupling elements, and the other is a UWB pyramidal antenna with a fixed notched band.

In Chapter 7, an application obtaining a proper surrogate model of the reconfigurable antenna is discussed. It is a reconfigurable UWB pyramidal monopole antenna with a tunable notched band.

In Chapter 8, an application obtaining a physics-based surrogate model within equivalent network analysis of a reconfigurable antenna is discussed. It is a reconfigurable UWB antenna with a tunable notched band.

Finally, Chapter 9 summarises this thesis and presents some promising academic topics in future.

Chapter 2

Literature Review

2.1 Ultra-Wide Band Antenna

Ultra-WideBand (UWB) antennas have the benefits of broad bandwidth, low cost, low energy consumption and high data rate. For example, in 2001, IEEE 802.15, bit rates up to 500 Mbps [26] were specified as a new standard on a physical layer of the UWB spectrum. Based on this, many UWB antennas have been proposed [35]. At the same time, the UWB antenna is a good platform for combining other techniques, such as Multiple-Input Multiple-Output (MIMO) and notched band. In order to further improve data rate, Multiple-Input Multiple-Output (MIMO) technology is usually utilized on UWB antenna [36].

However, due to its broad spectrum, the UWB antenna is easily interfered with by other electromagnetic signal sources. In order to avoid such interference, one of the solutions is to etch a slot on the UWB antenna to obtain a notched band. There are many kinds of slots [37], [38], [39], such as U-shape slot in Figure 2.1, L-shape slot in Figure 2.2, circle-shape slot in [40], and complicated slot in Figure 2.3.

To obtain multiple notched bands in one single antenna to eliminate interference

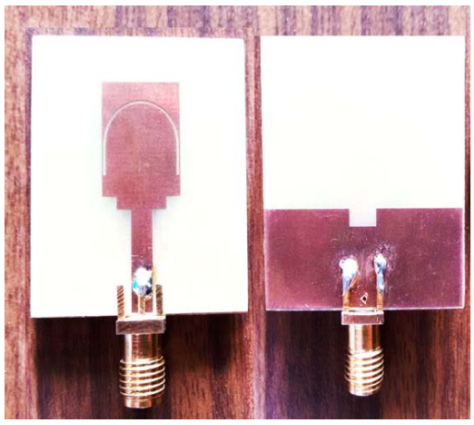

FIGURE 2.1: UWB antenna with U-shape slot in [18].

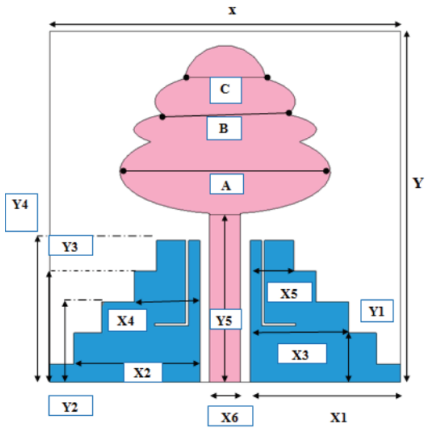

FIGURE 2.2: UWB antenna with L-shape slot in [25].

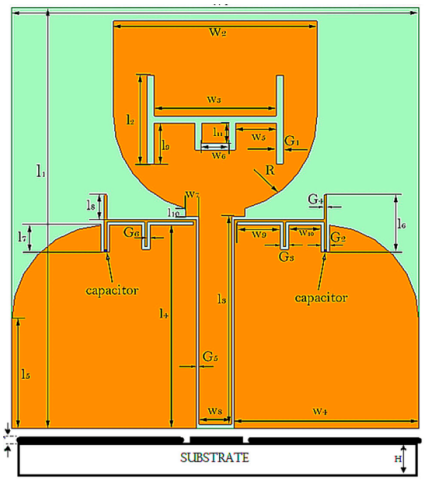

FIGURE 2.3: UWB antenna with complicated slot in [26].

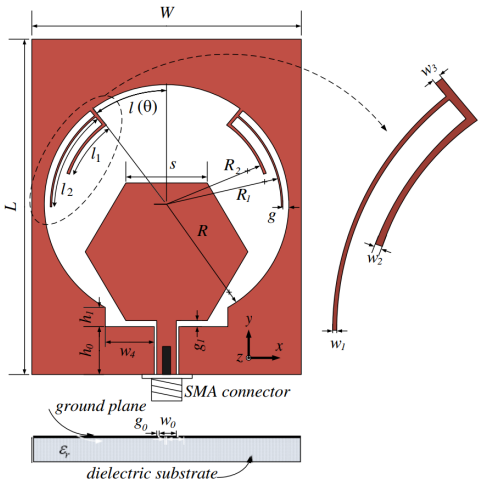

FIGURE 2.4: Geometry of UWB antenna with parasite branches in [41].

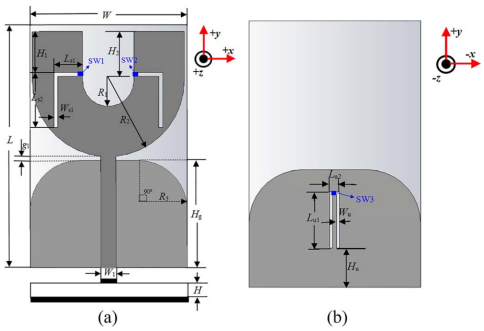

FIGURE 2.5: Geometry of the UWB band-notched antenna with switches in [46].

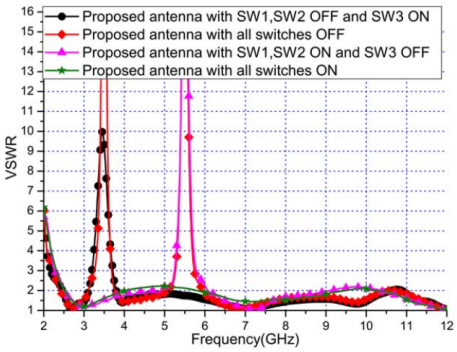

FIGURE 2.6: VSWR of the UWB band-notched antenna with switches in [46].

from several frequency bands, the UWB antenna is etched with several slots [42], [43].

In addition, other approaches to obtaining notched-band in the UWB antenna include parasitic strip, filtering integration, and defected ground structure (DGS) [41], [44], [45]. In [41], parasite branches are used to generate the notched band in the UWB antenna, its geometry shown in Figure 2.4.

Furthermore, the passive electronic elements, including switches, PIN diodes, varactors and MEMS, are mounted on slots in UWB antennas to obtain the UWB spectrum within switchable or tunable notched-band. Of course, they belong to the reconfigurable antenna from a reconfiguration point of view.

In [46], a band-notched UWB monopole antenna has L-shape slots loaded on the radiating part and U-shape slot loaded on the ground part, shown in Figure 2.5. Three switches are mounted in the slots, so this antenna can choose different notched bands. Its Voltage Standing Wave Ratio (VSWR) is shown in Figure 2.6, where it can be clearly seen that this antenna has four states controlled by these switches.

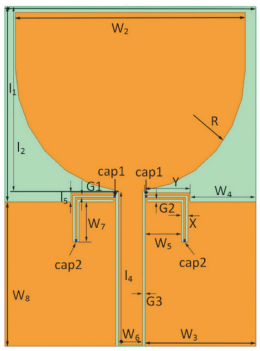

FIGURE 2.7: Geometry of the UWB band-notched antenna with varactors in [48].

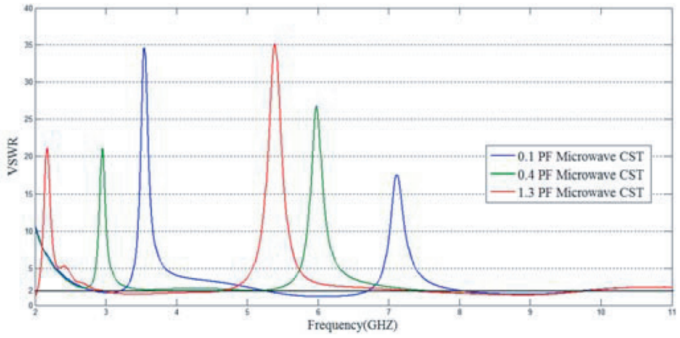

FIGURE 2.8: VSWR of the UWB band-notched antenna with varactors in [48].

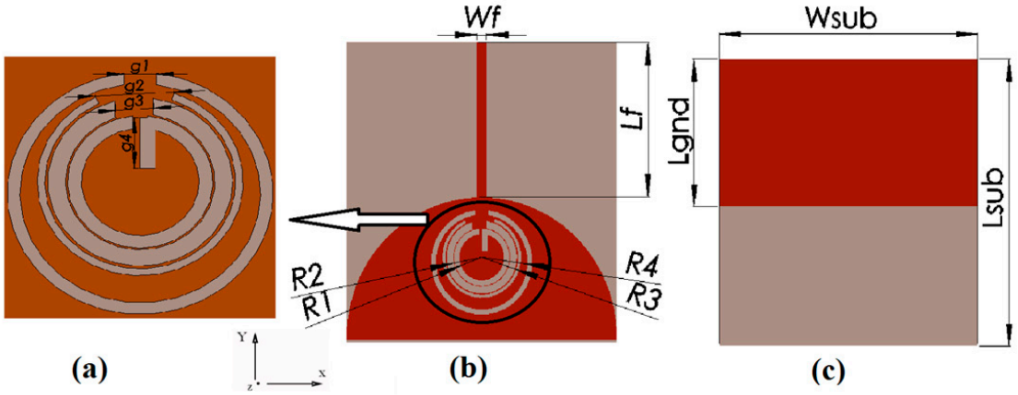

FIGURE 2.9: Geometry of the UWB antenna with circle-slots in [49].

In [47], a band-notched UWB antenna with varactors is proposed. In [48], the band-notched UWB antenna has four varactors in slots to obtain tunable notched bands. Its geometry is shown in Figure 2.7. From its response in Figure 2.8, it can be seen that the two notched bands of this antenna could be changed by tuning the value of varactors.

In [49], four circle-shaped slots are etched on the monopole antenna, shown in Figure 2.9. It has four notched bands to block the interference, and its VSWR is plotted in Figure 2.10. Each narrow notched band could be associated with a simple equivalent circuit consisting of resistor, capacitor and inductor. Thus, the equivalent circuit of circle-slots in this antenna is plotted in Figure 2.11. The equivalent circuit method is very effective in analysing the antenna. In Chapter 5, equivalent circuit methods and equivalent network analysis are presented.

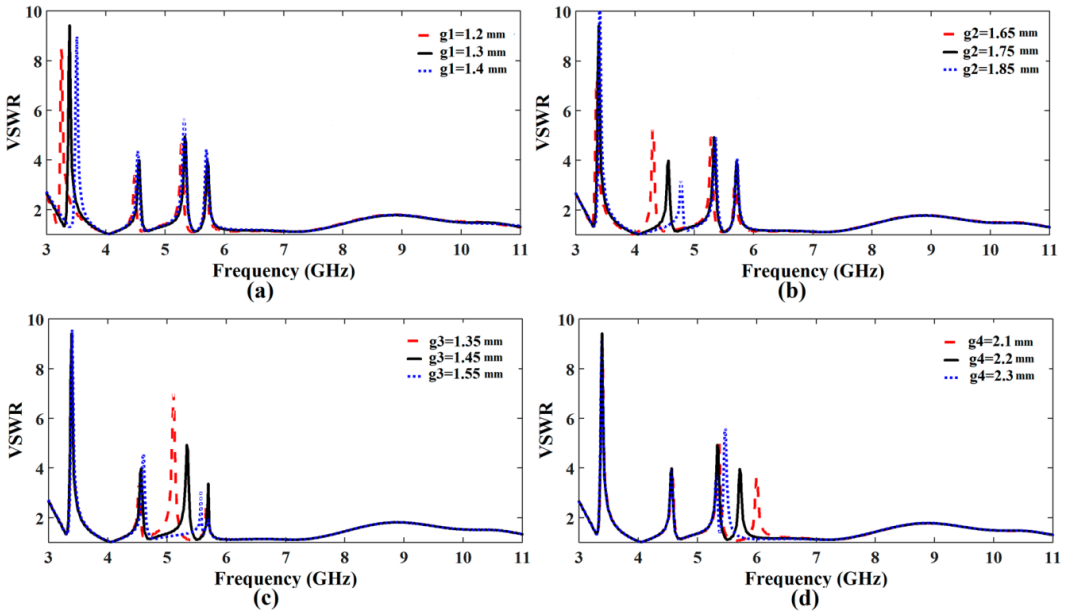

FIGURE 2.10: VSWR of the UWB antenna with circle-slots in [49].

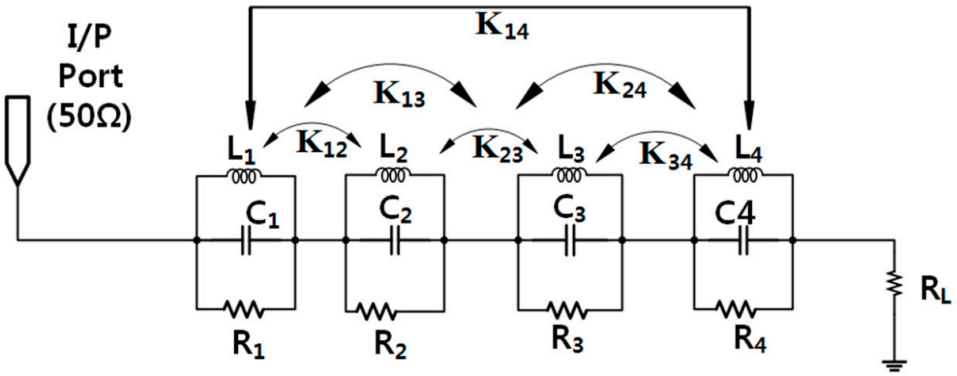

FIGURE 2.11: Equivalent circuit of the circle-slots part in [49].

2.2 Reconfigurable Antenna

A reconfigurable antenna has the ability to change an individual radiator's fundamental operating characteristics, such as working frequency, impedance bandwidths, radiation pattern and polarization. From this definition, it can be seen that the reconfigurable antenna could be any kind of antenna, for example, microstrip antenna [50], band-notched UWB antenna [46], [47], [48], cavity-backed slot antenna [11], and Vivaldi antenna [51].

The major types of reconfigurable antennas, categorized according to their reconfigurable characteristics, are frequency reconfiguration, radiation pattern reconfiguration, polarization reconfiguration, and hybrid reconfiguration. The original purpose of the reconfigurable antennas would be to independently change each of their individual fundamental characteristics to fulfil various requirements. In fact, it is a

TABLE 2.1: Common Types of Reconfigurable Antenna Techniques.

Type	Implemented Component or Material
physical change	structural alteration
material change	ferrites, liquid crystal
electrical change	RF-MEMS, PIN-diode, varactor
hybrid techniques	several techniques above

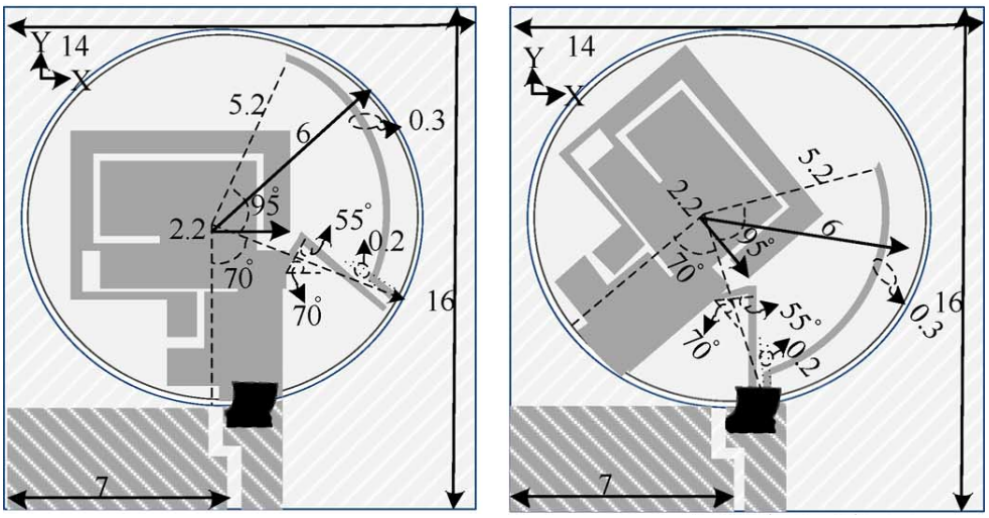

FIGURE 2.12: Mechanical reconfigurable antenna with rotation in [53].

challenge to obtain the desired change in antenna functionality without altering other characteristics [52].

The antenna reconfiguration can be obtained by the change of current distribution, the change of the antenna's physical structure, the change of the antenna radiating edges, or the change of the feeding network. Each parameter of the antenna characteristics can mutually affect others. Thus, all the antenna characteristics have to be analyzed simultaneously during the design process. To integrate new dynamic parameters into the initial traditional antenna, many factors such as complicated fabrication procedures, feedback circuitry, and control line design, should be considered.

In general, the reconfiguration is realized through the widespread techniques, which are categorized into four types, listed in Table 2.1.

2.2.1 Mechanical Reconfiguration

Antennas with mechanical reconfiguration change the effective electrical length of the resonant antenna or the resonant part by mechanical methods, so that the operation frequency would be changed. Of course, these mechanical methods often make

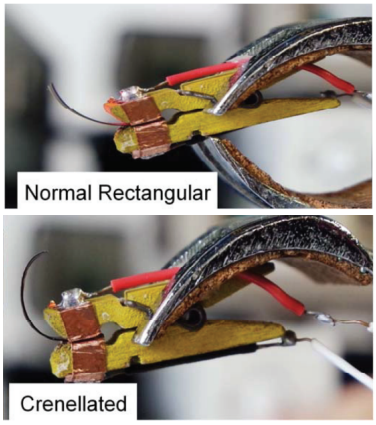

FIGURE 2.13: Different States of IPMC actuator in [14].

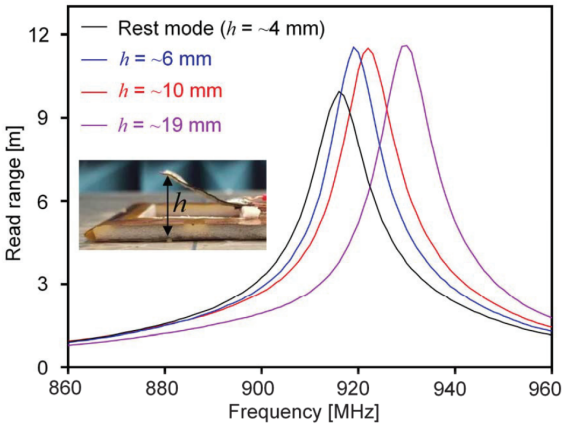

FIGURE 2.14: Resonant frequency with different states of IPMC actuator in [14].

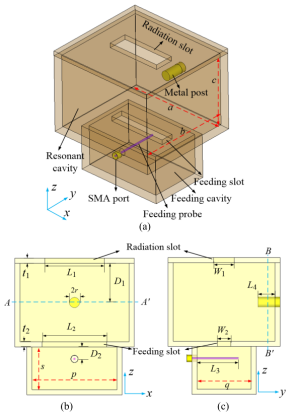

FIGURE 2.15: Reconfigurable cavity-backed slot antenna using movable metal post in [11]. (a) 3-D view. (b) Side view at *xz*-plane. (c) Side view at *yz*-plane.

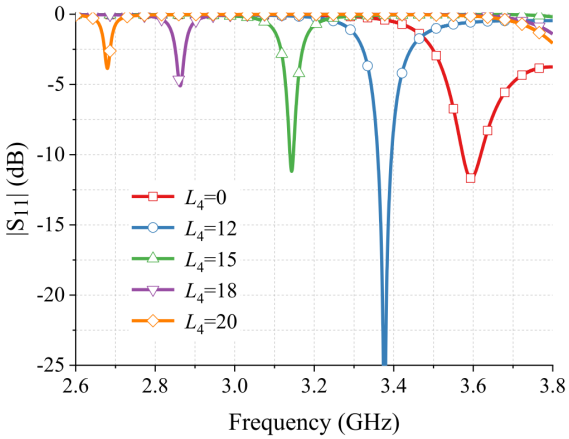

FIGURE 2.16: Antenna response with tunable metal post in [11].

use of electronic components to accomplish.

In [53], the primary radiation part of the reconfigurable antenna can be rotated, as shown in Figure 2.12, so that it can alter between two working states through rotation.

In [14], Ionic Polymer Metal Composite (IPMC) is used as an actuator, shown in Figure 2.13. The actuator can change its bend degree by tuning its bias voltage, its result shown in Figure 2.14. This reconfigurable antenna makes use of a bias circuit to change the shape of resonant metal.

In [11], a reconfigurable full-metal cavity-backed slot antenna is proposed, shown in Figure 2.15. A movable metal post controls its resonant frequency in Figure 2.16. The equivalent circuit model in Figure 2.17 clearly indicates the reconfigurable antenna's mechanism and the movable post's effect.

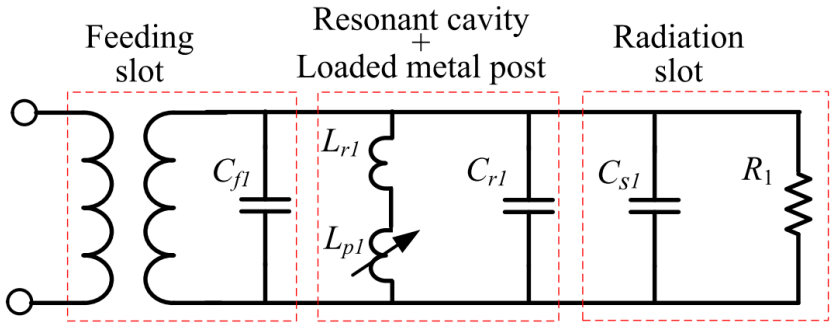

FIGURE 2.17: Equivalent circuit model of the reconfigurable slot antenna in [11].

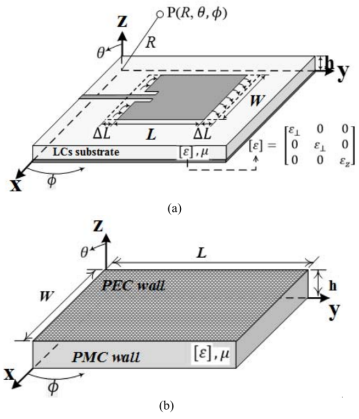

FIGURE 2.18: Geometry of patch antenna with liquid crystal substrate in [13]. (a) Rectangular patch antenna. (b) Theoretical cavity model.

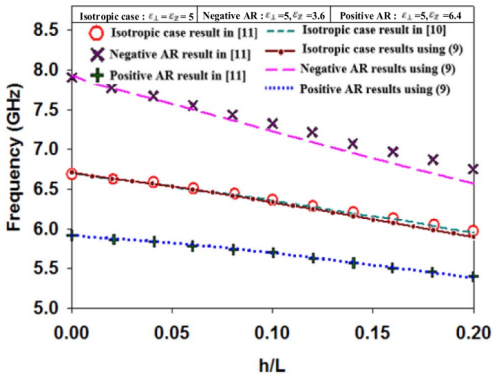

FIGURE 2.19: Resonant frequency as function of substrate thickness when ε_z changed in [13].

2.2.2 Material Reconfiguration

As an essential part of antennas, the change of substrate material could affect the antenna characteristics. Therefore, this property is utilized to design a reconfigurable antenna with material changes. For example, a ferro-electric material with changeable relative permeability [54], [55] and a ferrite material with changeable relative permeability [56], [57] are popularly applied as substrate materials of reconfigurable antennas. However, the notable drawback of the material reconfigurable is the high cost.

In [58], ferroelectric thin-film technology is used for tunable microwave devices, such as phased array antennas. In [59], barium strontium titanate (BST) thin film technology is used in a tunable filter and a phase shifter.

Additionally, the liquid crystal has been used as substrate material recently. In [13], a rectangular microstrip patch antenna utilizes liquid crystal as its substrate material, shown in Figure 2.18. Because the molecule orientations of liquid crystals are directional, the permittivity of liquid crystals is a tensor in physical expression. That

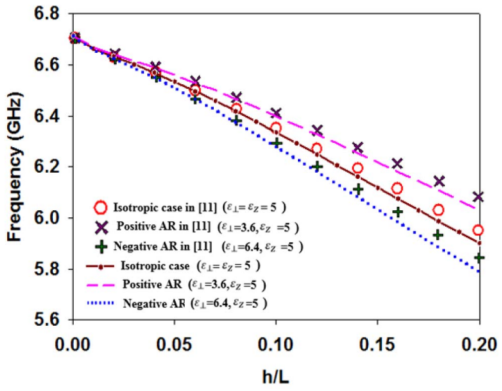

FIGURE 2.20: Resonant frequency as function of substrate thickness when $\varepsilon_{\perp}$ changed in [13].

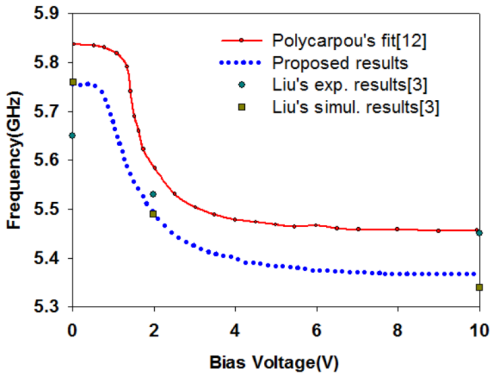

FIGURE 2.21: Antenna resonant frequency versus bias voltage in [13].

results in different permittivity with bias voltage on a different axis. The relations among bias direction, substrate thickness, and resonant frequency are shown in Figure 2.19 and Figure 2.20. The final dynamic frequency range of the reconfigurable antenna with tunable bias voltage is shown in Figure 2.21.

2.2.3 Electrical Reconfiguration

Antennas with electrical reconfiguration are loaded with electronic components, including switch, PIN diode, GaAs FET, MEMS, and varactors. These electronic components change the effective electrical length or current path so as to obtain the original antenna's reconfiguration. In addition, these components have their own practical properties, which could be suitable for different scenarios.

A switch is used to obtain alternation among several specific frequency bands or several specific radiation directions. That means the reconfiguration with switches is not continuous but discrete. In [60], two silicon photo switches in a dipole antenna are used to alter the length of dipole arms.

A diode is commonly used as a switch. Due to extra forward bias DC to control RF current, its power efficiency is low. A PIN diode is a popular product widely used in an RF circuit because of its low cost. In [51], there are many PIN diodes mounting on a Vivaldi antenna, shown in Figure 2.22. It can be seen that the initial Vivaldi antenna is cut into several pieces to configure enough independent bias circuits for each PIN diode. That causes big trouble during design and fabrication since it leads to fragility and vulnerability when used.

Because FET has the capacity of voltage-controlled-current, it has the benefit of low power consumption without biased current. Nevertheless, FET has poorer linearity and higher loss than PIN diode and varactor. GaAs FET is the popular

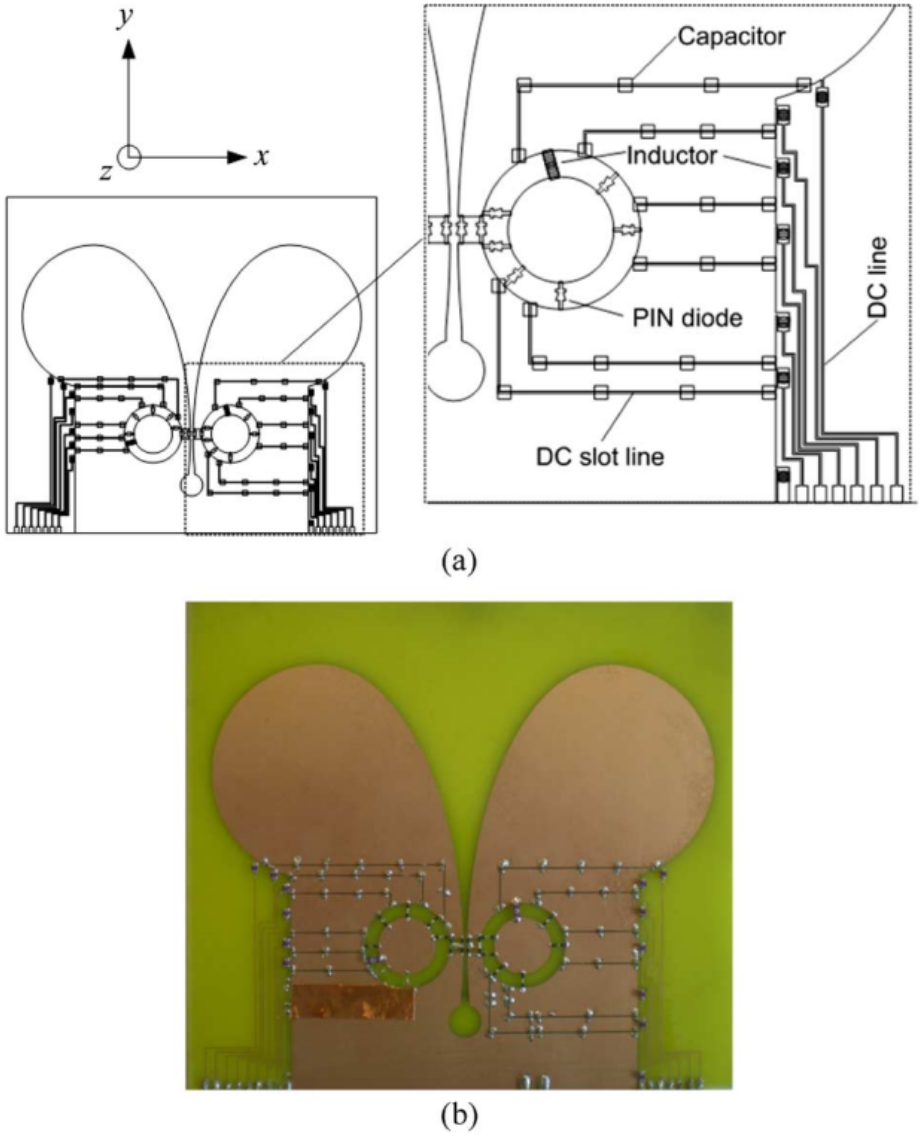

FIGURE 2.22: Geometry of the reconfigurable Vivaldi antenna in [51].
(a) Antenna design diagram. (b) The practical antenna.

product used in a reconfigurable antenna. In [61], two FET components are loaded into a slot to change the reactance.

A varactor diode can offer continuous tunable current, while its disadvantage is poor linearity. In [62], a dual-band reconfigurable slot antenna is designed to load a varactor.

MEMS device has the advantages of very low loss, wide bandwidth and low power consumption. However, at the same time, its disadvantages are higher operating voltage, higher cost and lower reliability than other semiconductor devices [16].

Negative impedance converters are developed in frequency reconfigurable antennas, in [15], [63].

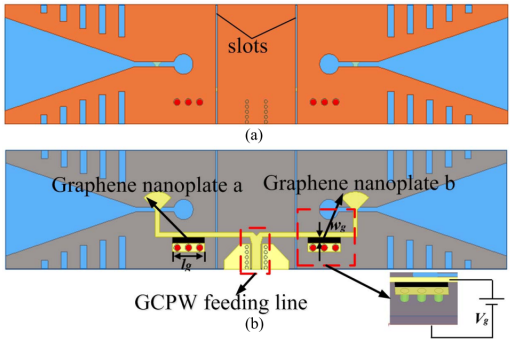

FIGURE 2.23: Configuration of the pattern reconfigurable Vivaldi antenna in [64]. (a) Top view. (b) Bottom view.

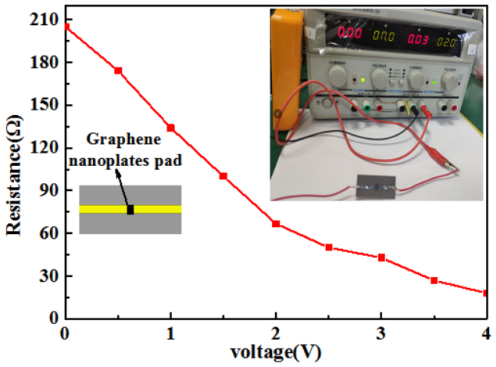

FIGURE 2.24: Sample graphene nanoplates and the resistance test results of graphene nanoplate pad in [64].

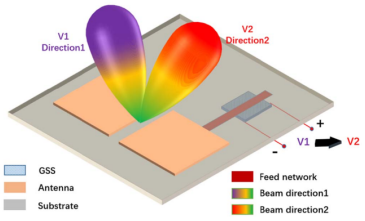

FIGURE 2.25: Schematic of the pattern reconfigurable antenna in [12].

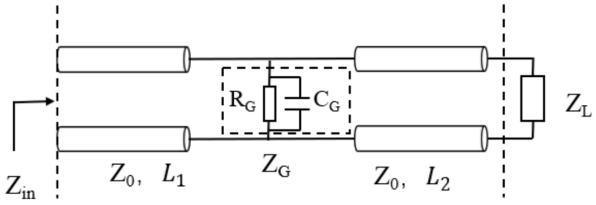

FIGURE 2.26: Equivalent circuit model of microstrip line in the pattern reconfigurable antenna in [12].

Additionally, other electronic components associated with new materials are developed. In [64], the tunable resistors based on graphene nanoplate are used in the Vivaldi antenna to obtain reconfiguration. The antenna configuration is shown in Figure 2.23 and the tunable resistor with bias voltage is shown in Figure 2.24.

Besides the frequency reconfiguration, the electronic components are also used for pattern reconfiguration. In [12], graphene is used in a radiation pattern reconfigurable antenna. The antenna schematic is shown in Figure 2.25. The equivalent circuit model of its crucial microstrip line is shown in Figure 2.26. With the illustration of the equivalent circuit, its reconfiguration mechanism can be easily understood.

2.3 Surrogate Model

Simulation using Computer-Aided Design (CAD) has been widely used to design and fabricate complicated systems. The CAD simulation can predict the system performance, so researchers and engineers can easily optimize the design and fabricate the product. There has been much commercial software in microwave and RF areas,

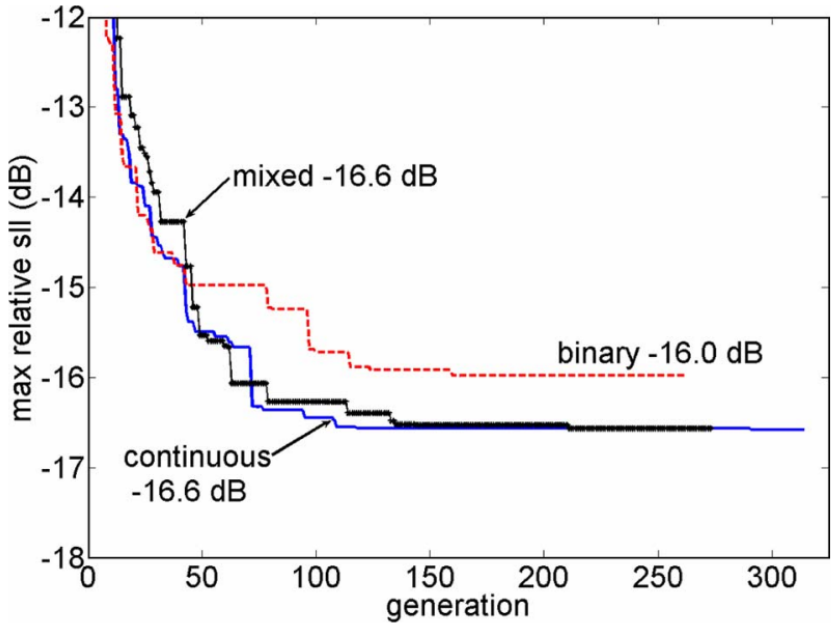

FIGURE 2.27: Convergence rates of Genetic Algorithm Model for the best out of 20 independent runs in [29].

including CST, HFSS, Sonnet, FeKo, Maxwell Eminence, Pspice, IE3D, Momentum, and Artemis Modal. They are based on different algorithms, including Finite-Difference Time-Domain (FDTD), Finite-Integration Time-Domain (FITD), Method of Moments (MoM), Finite Element (FE), Boundary Element Method (BEM), Spectral Method (SM), Transmission Line Method (TLM), Mode-Matching Method (MM), and Transverse Resonant Method (TRM). Therefore, suitable software with proper algorithms will simulate accurately and quickly for different conditions and requirements.

With the capacity of computers increasing continuously, computers will take on more complicated tasks for simulation. Even so, it is still impractical to model a full-wave simulation with every detail and to obtain overall relationships between all the parameters and the system performance [65]. A full-wave simulation is to calculate the EM field of the whole space using Maxwell's Equations. In the microwave area, the full-wave simulation of a large-scale complex system is always regarded as a full-wave high-fidelity simulation. However, the full-wave simulation needs to be reduced and simplified considering the time cost of practical design.

An effective way to reduce the computational runtime is to utilize surrogate models, also named approximation models [66]. The surrogate model is a simple model extracted from the complicated simulation model. Thus, it can replace the expensive original simulation model by approximating the input variables and the output

responses [28]. The surrogate model could also realize electromagnetic design optimization [67], [68], [69].

The quality of the surrogate modelling depends on the computational runtime and the computer's capability. Just as shown in Figure 2.27, the approximation performance of the Genetic Algorithm Model is better with longer runtime. Various applications based on different physical mechanisms are suited for different surrogate models.

There are many popular surrogate modelling techniques, such as Genetic Algorithm Model [29], Neural Network Model [70], Space Mapping, Vector Fitting [30], and Passive Macromodeling [31], [71].

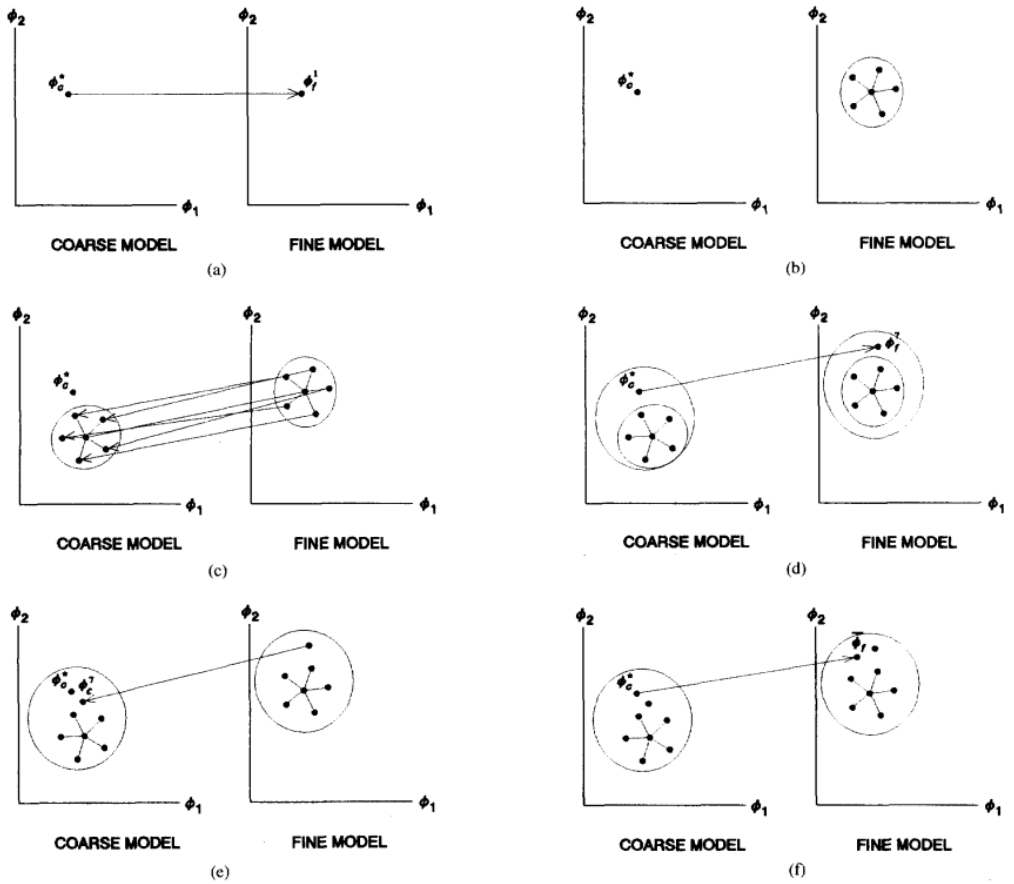

FIGURE 2.28: Illustration of Space Mapping in [72].

2.3.1 Space Mapping

Space Mapping (SM) is one of the most popular optimization techniques as a surrogate model in microwave engineering. In 1994, SM was first proposed in [72]. The foundation of SM based on multi-dimensional continuous space is that the continuously changed input variable leads to the continuously changed function's output, as

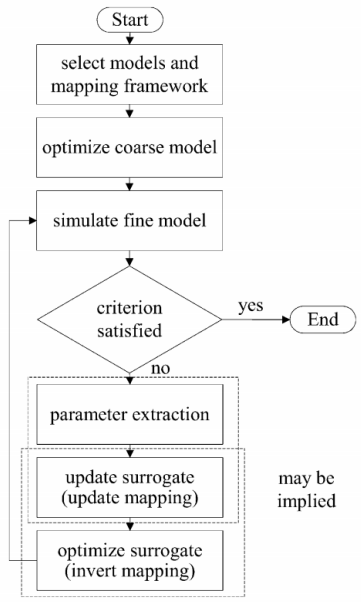

FIGURE 2.29: General Space Mapping flow chart in [34].

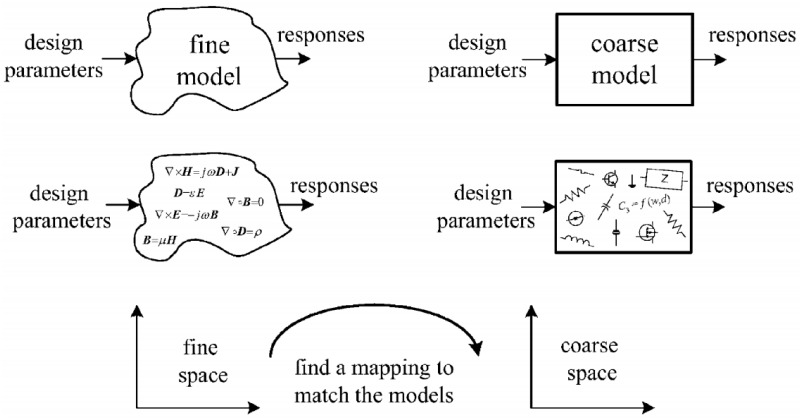

FIGURE 2.30: Linking companion coarse (empirical) and fine (EM) models through a mapping in [34].

shown in Figure 2.28. In order to improve the approximation precision, an iterative process is used, as shown in Figure 2.29.

SM technique is meaningful to obtain a linkage between coarse (empirical) model and fine (EM) model, shown in Figure 2.30. In particular, an equivalent circuit model as a coarse model is significant for system analysis in microwave and RF. The equivalent circuit model will help to reduce the difficulty, using circuit theory rather than full-wave EM analysis. Unfortunately, precise equivalent circuit models are not so easy to obtain from many systems, particularly broadband antenna [73] and substrate integrated structure [74]. Another issue for SM is the convergence of the iteration process. Because the mathematical space of SM is a multi-dimensional continuous

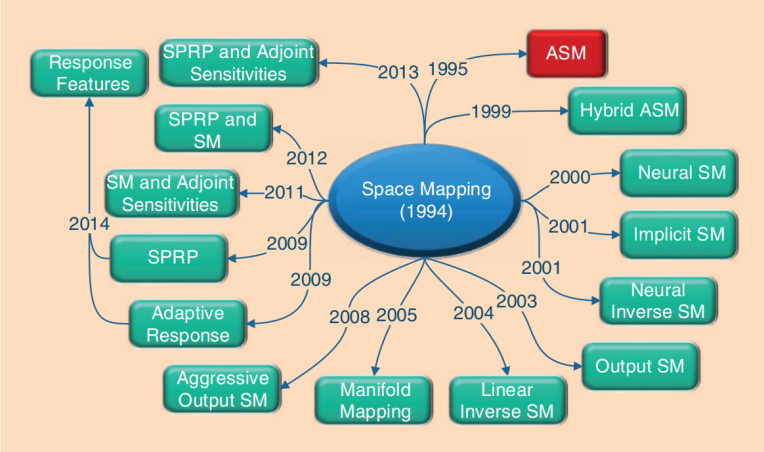

FIGURE 2.31: Derivation of Space Mapping in [32].

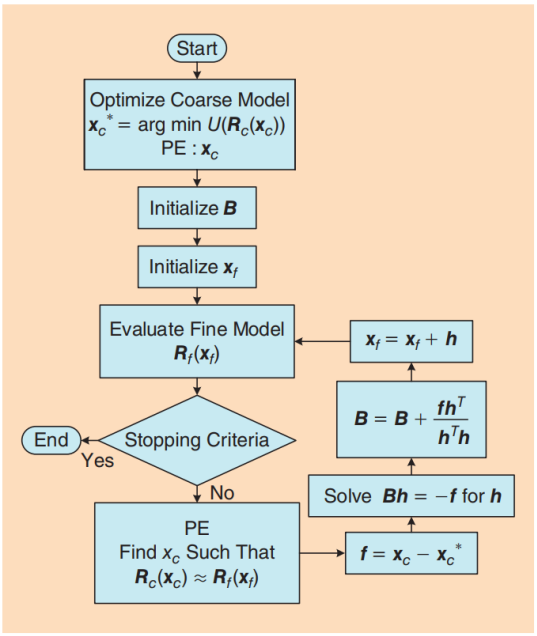

FIGURE 2.32: Flow diagram of the Aggressive Space Mapping (ASM) algorithm in [32].

space, the extreme value problem of the performance function with all extracted parameters is complicated even in a very tiny space. It causes the convergence issue, leading to the iterative process taking a long runtime without finding a good result with acceptable precision.

SM has been successfully utilized in many applications of microwave and RF, including filter [72], [75], [76], [33], [77], impedance transformer [34] , and antenna [78], [79], [80].

With the development of the SM technique, the concept of parameter extraction (PE) is mentioned in SM and highlighted gradually, shown in Figure 2.29. Parameter extraction is significant for Artificial Intelligence, which has become a new trend and a hot topic in scientific research.

FIGURE 2.33: The first decade of Aggressive Space Mapping (ASM) evolution in [32].

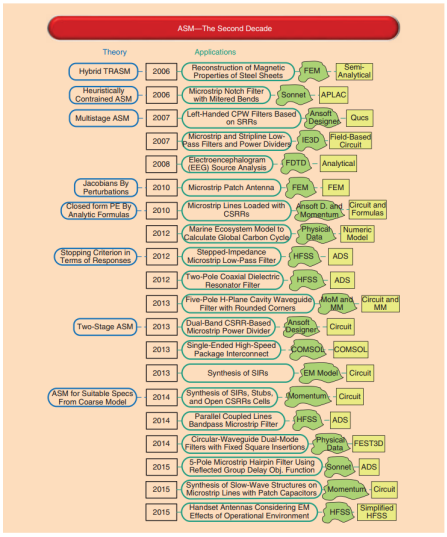

FIGURE 2.34: The second decade of Aggressive Space Mapping (ASM) evolution in [32].

SM has become one of the most widespread surrogate models because many other models are derived from the original SM algorithm, shown in Figure 2.31. It can be seen that the neural network could combine with the SM method. Among them, Aggressive Space Mapping (ASM) [81] is a successful derivation, and it is still developing. Figure 2.32 illustrates the difference between SM and ASM. In [32], the evolution history of ASM theory and applications are summarized in Figure 2.33 and Figure 2.34.

2.3.2 Passive Macromodeling

A simulation model on the computer containing all details of the large-scale system is impossible and unnecessary. The Macromodeling based on several extracted important parameters enables a feasible and effective simulation. The Marcomodel is a reduced-complexity behavioural description of a system or a collection system [71]. In other words, the Macromodel as an approximation method has to neglect some unimportant aspects of the system. Many approaches are derived from Macromodel, such as White-box Macromodeling, Gray-box Macromodeling, and Black-box Macromodeling.

Figure 2.35 shows the detailed Macromodeling flow based on model order reduction. The flow begins with the CAD data, which contains all geometry and material information of the overall system. Next, an electrical or electromagnetic system is configured by these CAD data as interface ports, so that a large-scale circuit is established with appropriate boundary conditions. At the same time, the differential

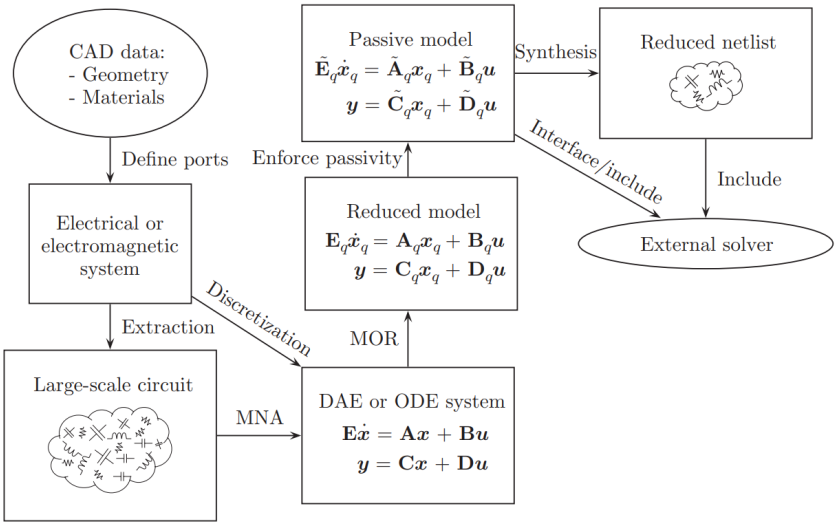

FIGURE 2.35: Macromodeling flow chart based on model order reduction in [71].

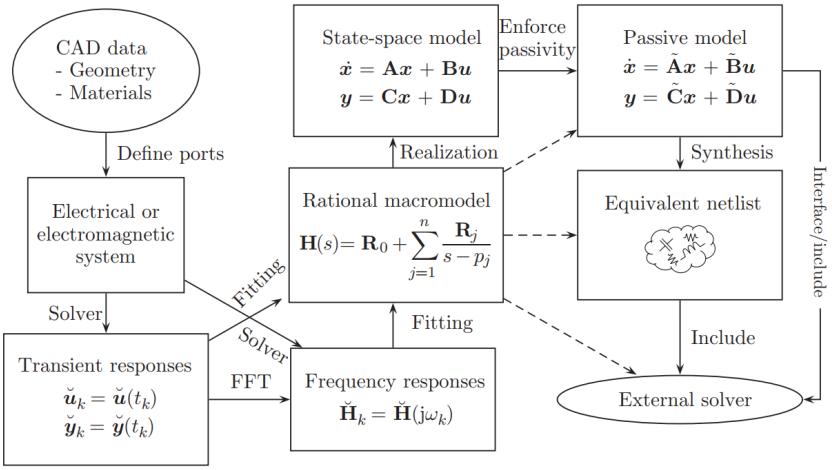

FIGURE 2.36: Macromodeling flow chart based on computed responses by full-wave solvers in [71].

algebraic equations (DAEs) or the ordinary differential equations (ODEs) are easily obtained using Maxwell's equations and Kirchhoff's Laws. Actually, the large-scale circuit can be equivalent to the DAE/ODE through standard modified nodal analysis (MNA). At this stage, both the circuit and the equations are large-scale, which could be compressed to reduce the size and complexity through model order reduction (MOR) while preserving its main input-output characteristics. The last step is to simulate the exported data using an external solver.

In [71], the second Macromodeling flow based on full-wave solvers is presented in Figure 2.36. It also begins with the CAD data, which contains all geometry and material information of the overall system. These CAD data configure an electrical or electromagnetic system as interface ports. From this data system, the transient

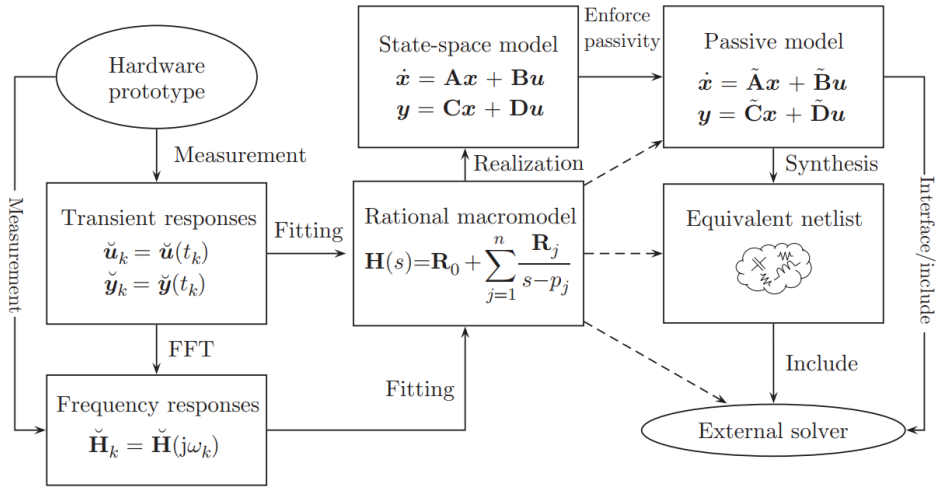

FIGURE 2.37: Macromodeling flow chart based on measurement responses in [71].

responses in the time domain or the system responses in the frequency domain can be obtained, which is different from the previous flow process. Actually, the transient responses and frequency responses are regarded as the same, because they could be mutually converted to each other through Fourier Transform or Inverse Fourier Transform. And then, through a fitting method, the rational macromodel can be built from these responses in the time domain or frequency domain. Based on the property of rational functions, the rational macromodel could connect to an external solver. The rational macromodel is so significant that a state-space model, passive model, and equivalent netlist model could be obtained directly from it. Of course, a pole-residue analysis can be done from the rational macromodel without going through a state-space realization.

The last Macromodeling flow is indeed a black box in Figure 2.37. In this flow process, the start point is from the measurement data of the practical hardware. The most common method is using Vector Network Analyzer (VNA) to export a set of the scattering parameters data of practical hardware in the frequency domain. Another method is using Time-Domain Reflectometry (TDR) triggered by an excitation pulse to record the transient responses of the practical hardware. The transient responses can be converted to frequency responses, or vice versa. And then, from these responses in the time or frequency domain, the essential rational macromodel can be extracted by a fitting method. The subsequent flow process is the same as the counterpart in Figure 2.36.

2.4 Summary

From this background study, several conclusions are drawn, and some issues are exposed. In the field of ultra-wideband antennas, it shows that many kinds of UWB antennas are available in the current literature. The UWB antenna with a notched band can avoid interference. However, it is difficult to extract features describing the antenna system, due to its broad working band with one or several narrow notched band(s). Thus, a precise surrogate modelling technique is required to accurately recognize the narrow notched band from the UWB spectrum. In reconfigurable antennas, many reconfiguration mechanisms are used to design the antenna. Compared with traditional antennas, the significant advantage of the reconfigurable antenna is its tunable performance. A proper surrogate model is required to connect the signal processing and practical antenna parts. Furthermore, due to the diversity, the surrogate model must be more generic to cover all kinds of reconfigurable antennas. In the field of surrogate models, several techniques are presented. However, none of them could be applied specifically in a reconfigurable antenna. Such surrogate modelling techniques are essential to integrating the reconfigurable antennas into a communication system. Addressing the above issues is the main objective of this PhD study.

Chapter 3

New Perspectives

In order to address such existing challenges mentioned in Chapter 1, new perspectives are proposed as the principles in the thesis, which is the starting point of this work and provides research direction. This chapter is the guideline of the whole work. The embodiment of such new perspectives are in the subsequent chapters, including analytical function fitting derivation in Chapter 4, equivalent circuit/network techniques in Chapter 5, and surrogate modelling applications in Chapter 6, Chapter 7 and Chapter 8.

3.1 Field & Circuit

Field and circuit are two common perspectives to analyse electromagnetic systems.

The field perspective is embodied in the full-wave electromagnetic analysis based on Maxwell's Equations. Over the last two decades, a lot of CAD software has been developed to facilitate such analysis. However, due to the large-scale and complicated structure, the simulation of the EM system related to the field takes enormous computer resources and long runtime, since the EM information in the total space has to be calculated.

Circuit operating uses the equivalent circuit or transmission line to simplify and reduce the full-wave EM system. The basic circuit theory is Kirchhoff's Voltage/Current Laws rather than Maxwell's Equations, because the circuit operating is more accessible and takes less runtime. Many basic books about microwave engineering [82] mention it and explain it clearly. It is worth noting that there are two limited conditions in the circuit operating. One is that the circuit operating works at low frequencies. The other is that the circuit dimensions are small relative to the wavelength. Both conditions require that the physical size of the EM system is small enough, so that the phase delay from one point in the circuit to another could be negligible [83].

For such an issue with broadband, a novel approach could obtain a rational function in the frequency domain to describe the system response.

The function of frequency describing the EM system performance could extend from a constant frequency to a frequency band, so that the function could describe the system with broadband. Additionally, if the function is in the complex domain, the phase information of the EM system could be expressed accurately. Thus the phase delay of a large-scale system will not be an intricate issue. Finally, the analytical function could be easily converted to the equivalent circuit, which is essential and valuable during design and analysis. Such examples and benefits will be shown in Chapter 5 and Chapter 8.

3.2 Feature Extraction from Antenna

In the last decade, Artificial Intelligence (AI) has become a new frontier of academic research and has generated a lot of successful processes in many areas, including machine perception, computer vision, and speech recognition. It also attracts researchers' attention in microwave and radio frequency (RF) areas. In 2021, there are special issues from *IEEE Transactions on Antennas and Propagation* [21] and *IEEE Transactions on Microwave Theory and Techniques* [22] to devote such scientific topics: Machine Learning in antenna design and communication system based on AI.

In AI algorithms, feature extraction is a significant notion. How to extract the features from the microwave system is a critical first step. A good feature extraction should contain two points. The first one is that the extracted features could include all or most of the system performances. In other words, using the extracted features could almost construct the original EM system. The second one is that the number of extracted features should be as few as possible. In order to evaluate the extracting efficiency, a compression ratio, which is the ratio between the number of extracted features and the number of original discrete data, is used.

3.3 Reconfigurable Antenna

A reconfigurable antenna can alter its own electromagnetic properties, including working frequency, impedance bandwidth, polarization, and radiation pattern, in a controlled and reversible manner [52]. The controllable components, such as mechanical actuators, tunable materials, RF switches, varactors and MEMS, are integrated into the original traditional antenna to provide a dynamic response.

Using the mathematical expression to describe the above concept is a new perspective on the reconfigurable antenna. For a traditional antenna, the observable response $\check{H}(s)$ could be approximated by an analytical fitting function $H(s)$. It is a

function of the only input variable, frequency (s or f). For a reconfigurable antenna, the additional variables (p_1, p_2, $\cdots$), named the input dynamic ranges of reconfiguration, are integrated into the response function. The additional variables (p_1, p_2, $\cdots$) leads that the input and output space has additional dimensions. The response function of the reconfigurable antenna becomes $H(s, p_1, p_2, \cdots)$, so it can display clearly the relationships between the antenna responses and the reconfigurable parameters.

Strictly speaking, $H(s)$ only represents the total responses of frequency without any spatial distributional information. To describe the pattern reconfigurable antenna, the radiation pattern of the traditional antenna could be denoted by $R(s, \theta, \phi)$. Likewise, with the integration of input dynamic ranges (p_1, p_2, $\cdots$), the new radiation pattern becomes $R(s, \theta, \phi, p_1, p_2, \cdots)$. The mathematical form shows clearly the relationship between the radiation pattern and the input dynamic ranges.

Furthermore, the response characteristic in detail should be taken into account. For example, the output of $H(s)$ is in a complex field, and $R(s)$ is a 2-dimensional complex function.

To sum up, the reconfiguration extends the dimensions of the input variables in mathematics.

3.4 Summary

Some perspectives have been developed as principles to guide the following research work, which is classified into two parts: theory and applications. The theory part contains the analytical function fitting in Chapter 4 and equivalent circuit methods and equivalent network analysis in Chapter 5. Chapter 4 is to extract the analytical response function through the fitting method. Chapter 5 converts the analytical function to equivalent circuit topology. The second part includes the application to traditional antennas in Chapter 6, a data-driven surrogate modelling approach of a reconfigurable antenna in Chapter 7, and a physics-based surrogate modelling approach of a reconfigurable antenna in Chapter 8. It is the practical application and verification of the theory. Both the theory part and the application part are embodiment and realization of the new perspectives in this chapter.

Chapter 4

Function Fitting

In this chapter, an analytical function is obtained from the discrete numerical data of the EM system response through the fitting method. A mathematical procedure for finding the optimal fitting function to a known set of data is to minimize the sum of the squares of the offsets between the known data set and the fitting function. During this procedure, the offset is named residuals. The evaluation criterion is "to minimize the sum of the squares of the offsets", which the name Least Square Method comes from.

The linear least squares fitting technique is the simplest and most commonly applied form of linear regression. It provides a solution to the problem of finding the best fitting polynomial function through some data, experiments, or observations. However, for a nonlinear function fitting to several unknown parameters, the linear least squares method must cooperate with an iterative process to achieve the accurate solution.

These principles and formulas in mathematics are basic and common, which could be found in previous research [84]. Based on these, extension from a real field to a complex field is derivated step by step in this thesis. Finally, a generic approach, Rational Fitting with Weighted Iteration (RFWI), is developed to specifically obtain analytical rational function in the complex field for microwave system. It is the theoretical foundation of subsequent work in this thesis.

4.1 Statistical Method

The Least Square Method is most famous as a fitting method to obtain an analytical function. In this thesis, polynomial functions and rational functions fit in both real and complex fields based on the least square method. To simplify the thesis structure, the general formulas of rational function fitting are shown in this chapter. At the same time, the basic formulas are in the Appendix A.

In the microwave area, the function in the complex field is essential since harmonic electromagnetic field, electronic components (such as capacitors, inductors),

and reflection coefficient are always expressed as complex functions. The rational function in a complex field is chosen as the target function of the fitting.

4.1.1 Rational Function in Real Field

In mathematics, a rational function is also named a rational fraction. Because it is a non-linear function, the least square method could not obtain an accurate fitting function. Luckily, it is still possible to optimize this problem by linearizing the non-linear function or by an iterative procedure. In the following, a simple linearizing approximation is presented. With the subsequent iterative procedure, it will lead to a precise solution.

I. (m, n)-order real rational function (General Expression)

From the basic formulas in Appendix A, it can be seen that with the higher order of the rational function, the unknown parameters become more and the final matrix equation becomes larger. The final matrix equations, such as Equation (A.12), Equation (A.16), Equation (A.20), are still regular. Based on the same process and such regulation, the general formula with arbitrary order in the rational function can be derived,

$$\begin{aligned} Y \approx Y_f =& \frac{X^m + b_1 X^{m-1} + \cdots + b_i X^{m-i} + \cdots + b_m}{a_1 X^n + a_2 X^{n-1} + \cdots + a_j X^{n+1-j} + \cdots + a_{n+1}} \\ =& \frac{X^m + \sum_{j=1}^{m} b_j X^{m-j}}{\sum_{j=1}^{n+1} a_j X^{n+1-j}} \end{aligned} \tag{4.1}$$

where Y is the observable output, Y_f is the output of the fitting function, and X is the observable input variable. In the fitting function, the unknown parameters in denominator polynomial and in numerator polynomial are $a_j (1 \leq j \leq n+1)$ and $b_i (0 \leq i \leq m)$, respectively. The orders of denominator polynomial and numerator polynomial are $n+1$ and m, respectively. In order to keep the uniqueness of the rational function, the coefficient of X^m in numerator polynomial is set 1 (or $b_0 = 1$).

To display the derivation of each parameter in detail, the expectation of the squared operator in statistics is used here. The expectation of the squared residual, labelled as e, is

$$
\begin{aligned}
e =& E[(Y\sum_{j=1}^{n+1} a_j X^{n+1-j} - X^m - \sum_{j=1}^{m} b_j X^{m-j})^2] \\
=& E[Y^2(\sum_{j=1}^{n+1} a_j X^{n+1-j})^2 + X^{2m} + (\sum_{j=1}^{m} b_j X^{m-j})^2 \\
& - 2X^m Y\sum_{j=1}^{n+1} a_j X^{n+1-j} - 2Y(\sum_{j=1}^{n+1} a_j X^{n+1-j})(\sum_{j=1}^{m} b_j X^{m-j}) + 2X^m\sum_{j=1}^{m} b_j X^{m-j}]
\end{aligned}
\tag{4.2}
$$

The least squares method is to find the optimal parameters by minimizing the expectation e. The fitting function contains $m+n+1$ unknown parameters, which are $(a_1, \cdots, a_i, \cdots, a_{n+1}, b_1, \cdots, b_j, \cdots, b_m)$. Thus, there are $m+n+1$ gradient equations, which are e on their partial derivatives, respectively. By setting each gradient equation to zero, a group of equations composed of the unknown parameters is obtained,

$$
\begin{cases}
0 = \dfrac{\partial e}{\partial a_i} = E[2X^{n+1-i}Y^2\sum\limits_{j=1}^{n+1} a_j X^{n+1-j} - 2X^{m+n+1-i}Y - 2X^{n+1-i}Y\sum\limits_{j=1}^{m} b_j X^{m-j}], \\
\qquad\qquad\qquad\qquad\qquad\qquad\qquad\qquad (1 \le i \le n+1) \\
0 = \dfrac{\partial e}{\partial b_i} = E[2X^{m-i}\sum\limits_{j=1}^{m} b_j X^{m-j} - 2X^{m-i}Y\sum\limits_{j=1}^{n+1} a_j X^{n+1-j} + 2X^{2m-i}], \\
\qquad\qquad\qquad\qquad\qquad\qquad\qquad\qquad (1 \le j \le m)
\end{cases}
\tag{4.3}
$$

The partial equation group can be expressed as the matrix equation,

$$
\boldsymbol{A}\cdot\boldsymbol{\Gamma} = \boldsymbol{B} \tag{4.4}
$$

where the unknown parameters (a_i, b_j) are spliced to form a new $(m+n+1)$-dimensional vector $\boldsymbol{\Gamma}$ as,

$$
\boldsymbol{\Gamma}^T = [a_1, a_2, \cdots, a_{n+1}, b_1, b_2, \cdots, b_m]. \tag{4.5}
$$

$\boldsymbol{A}$ and $\boldsymbol{B}$ composed of observable data (X, Y) are matrix and vector, respectively,

$$
\begin{aligned}
\boldsymbol{B}^T =& [E[X^{m+n}Y], E[X^{m+n-1}Y], \cdots, E[X^{m+n-i}Y], \cdots, E[X^m Y], \\
& E[X^{2m-1}], E[X^{2m-2}], \cdots, E[X^{2m-j}], \cdots, E[X^m]]; \quad (0 \le i \le n; 1 \le j \le m)
\end{aligned}
\tag{4.6}
$$

$$\boldsymbol{A} = \begin{bmatrix} \boldsymbol{A}_{11} & \boldsymbol{A}_{12} \\ \boldsymbol{A}_{21} & \boldsymbol{A}_{22} \end{bmatrix} \tag{4.7}$$

$$\begin{aligned} \boldsymbol{A}_{11}(i,j) &= E[X^{2n+2-i-j}Y^2] && (1 \le i \le n+1; 1 \le j \le n+1) \\ \boldsymbol{A}_{12}(i,j) &= -E[X^{m+n+1-i-j}Y] && (1 \le i \le n+1; 1 \le j \le m) \\ \boldsymbol{A}_{21}(i,j) &= E[X^{m+n+1-i-j}Y] && (1 \le i \le m; 1 \le j \le n+1) \\ \boldsymbol{A}_{22}(i,j) &= -E[X^{2m-i-j}] && (1 \le i \le m; 1 \le j \le m) \end{aligned} \tag{4.8}$$

II. (m, n)-order real rational function (for Programme)

Although the general matrix equation looks regular and tidy in mathematics, a programme-friendly expression is more useful in practical applications. Additionally, the programs have many build-in and ready-made mathematical operations, especially the software Matlab is very good at matrix calculation and has a partial derivative function.

$$\begin{aligned} Y \approx Y_f =& \frac{X^m + b_1 X^{m-1} + \cdots + b_i X^{m-i} + \cdots + b_m}{a_1 X^n + a_2 X^{n-1} + \cdots + a_j X^{n+1-j} + \cdots + a_{n+1}} \\ =& \frac{X^m + \sum_{j=1}^{m} b_j X^{m-j}}{\sum_{j=1}^{n+1} a_j X^{n+1-j}} = \frac{Numerator}{Denominator} \end{aligned} \tag{4.9}$$

After approximation, the expectation of squared residual is

$$e = E[(Y \cdot Denominator - Numerator)^2] \tag{4.10}$$

The $(m+n+1)$-dimensional vector $\boldsymbol{\Gamma}$ is

$$\boldsymbol{\Gamma}^T = [a_1, a_2, \cdots, a_{n+1}, b_1, b_2, \cdots, b_m] \tag{4.11}$$

Setting the gradient equations to zero can generate the equations to find out the unknown parameters,

$$0 = \frac{\partial e}{\partial \boldsymbol{\Gamma}_i} = \sum_{j=1}^{m+n+1} (\boldsymbol{\Gamma}_j \cdot \frac{\partial^2 e}{\partial \boldsymbol{\Gamma}_i \partial \boldsymbol{\Gamma}_j}) + \left.\frac{\partial e}{\partial \boldsymbol{\Gamma}_i}\right|_{\boldsymbol{\Gamma}=\boldsymbol{0}}, \quad (1 \le i \le m+n+1) \tag{4.12}$$

The matrix equation can be expressed as

$$\boldsymbol{A} \cdot \boldsymbol{\Gamma} = \boldsymbol{B} \tag{4.13}$$

$$\boldsymbol{A}_{ij} = \frac{\partial^2 e}{\partial \boldsymbol{\Gamma}_i \partial \boldsymbol{\Gamma}_j}; \qquad \boldsymbol{B}_i = -\frac{\partial e}{\partial \boldsymbol{\Gamma}_i}\bigg|_{\boldsymbol{\Gamma}=\mathbf{0}} \tag{4.14}$$

For the programs, the formulas do not need to simplify but keep the mathematical operations, such as Equation (4.12) and Equation (4.14). That is the main difference from the general mathematical expression.

4.1.2 Rational Function in Complex Field

In the microwave area, a complex rational function has more practical meaning and applications. For example, the complex rational function can be converted to an equivalent lumped circuit.

I. (m, n)-order complex rational function (for Programme)

The general matrix equation of the rational function in a complex field is complicated, while the programme formula looks tidy and easy to execute. Significantly, the software Matlab is very good at matrix calculation and has built-in functionality for the partial derivative function.

The fitting function Z_f with the observable input variable s and $m+n+1$ unknown parameters $(a_1, \cdots, a_{n+1}, b_1, \cdots, b_m)$, approximating the observable output Z, is,

$$\begin{aligned} Z \approx Z_f =& \frac{s^m + b_1 s^{m-1} + \cdots + b_i s^{m-i} + \cdots + b_m}{a_1 s^n + a_2 s^{n-1} + \cdots + a_j s^{n+1-j} + \cdots + a_{n+1}} \\ =& \frac{s^m + \sum_{j=1}^{m} b_j s^{m-j}}{\sum_{j=1}^{n+1} a_j s^{n+1-j}} = \frac{Numerator}{Denominator}. \end{aligned} \tag{4.15}$$

The subscript letter f of Z_f means fitting. Z_f is the function of s, so its complete expression is $Z_f(s)$. The notation s is related to frequency f or ω ($s = j2\pi f$, or $s = j\omega$) in Fourier transform and Laplace transform. The fitting function Z_f and observable output Z are in a complex field, and the input variable s is a pure imaginary number, while the unknown parameters (a_1, a_2) are in the real field. So, $Z, Z_f, s \in \mathbb{C}$ and $a_1, a_2 \in \mathbb{R}$. They can be expressed as

$$\begin{cases} Z = R + jX \\ s = j\omega \end{cases} \tag{4.16}$$

where R, X, and ω are real numbers ($R, X, \omega \in \mathbb{R}$). After approximation, the expectation of squared residual e is

$$e = E[|Z \cdot Denominator - Numerator|^2] \tag{4.17}$$

The $(m+n+1)$-dimensional vector $\mathbf{\Gamma}$ is

$$\mathbf{\Gamma}^T = [a_1, a_2, \cdots, a_{n+1}, b_1, b_2, \cdots, b_m] \tag{4.18}$$

Setting the gradient equations to zero can generate the equations to find out the unknown parameters,

$$0 = \frac{\partial e}{\partial \mathbf{\Gamma}_i} = \sum_{j=1}^{m+n+1} (\mathbf{\Gamma}_j \cdot \frac{\partial^2 e}{\partial \mathbf{\Gamma}_i \partial \mathbf{\Gamma}_j}) + \left.\frac{\partial e}{\partial \mathbf{\Gamma}_i}\right|_{\mathbf{\Gamma}=\mathbf{0}}, \quad (1 \le i \le m+n+1) \tag{4.19}$$

The matrix equation can be expressed as

$$\boldsymbol{A} \cdot \mathbf{\Gamma} = \boldsymbol{B} \tag{4.20}$$

$$\boldsymbol{A}_{ij} = \frac{\partial^2 e}{\partial \mathbf{\Gamma}_i \partial \mathbf{\Gamma}_j}; \qquad \boldsymbol{B}_i = -\left.\frac{\partial e}{\partial \mathbf{\Gamma}_i}\right|_{\mathbf{\Gamma}=\mathbf{0}} \tag{4.21}$$

For the programmes, the formulas do not need to simplify but keep the mathematical operations, such as Equation (4.19) and Equation (4.21).

4.2 Rational Fitting with Weighted Iteration (RFWI)

Based on the least squared method, the rational function fitting in the complex field can be executable, which is discussed in the last section. For the non-linear function, the approximation to linearize the function is necessary, and the previous fitting must combine with iteration to improve the precision. In the microwave area, it could take into account all steps as a whole, including the fitting in a complex field, compensatory correction and controllable iteration. Based on rigorous mathematical derivation, a novel approach named Rational Fitting with Weighted Iteration (RFWI) is developed.

4.2.1 Overdetermined Systems

To approximate the observable output of the system response $\check{H}(s)$ in the frequency domain, the fitting function $H(s;\boldsymbol{x})$ as the type of rational function is:

$$\check{H}(s) \approx H(s;\boldsymbol{x}) = \frac{N(s;\boldsymbol{x})}{D(s;\boldsymbol{x})} = \frac{s^m + b_1 s^{m-1} + \cdots + b_i s^{m-i} + \cdots + b_m}{a_1 s^n + a_2 s^{n-1} + \cdots + a_j s^{n+1-j} + \cdots + a_{n+1}}, \tag{4.22}$$

where $N(s;\boldsymbol{x})$ and $D(s;\boldsymbol{x})$ denote numerator polynomial and denominator polynomial, m and n are the degrees of the numerator and the denominator polynomials, also named as the order of rational function relating to the functional complexity and the precision limitation of the approximation function.

There are two reasons why the rational function is chosen as an approximation function. Firstly, the order of rational function can be extended or be shrunk easily with different precision requirements, which could get arbitrary accuracy if not considering computational runtime. Secondly, the rational function can be conveniently converted to an equivalent lumped circuit, or vice versa [85], which could be valuable for equivalent circuit and network analysis.

The unknown coefficients (a_i, b_j) are spliced to form a new (m+n+1)- dimensional vector $\boldsymbol{x}$ as

$$\boldsymbol{x} = (a_1, a_2, \cdots, a_{n+1}, b_1, b_2, \cdots, b_m)^T. \tag{4.23}$$

To avoid to confuse with $\boldsymbol{\Gamma}$ (reflection coefficient), the unknown coefficient vector $\boldsymbol{x}$ is used in the following. The unknown coefficient vector $\boldsymbol{x}$, determining the approximation rational function $H(s;\boldsymbol{x})$, belongs to the real number field, $\boldsymbol{x} \in \mathbb{R}^{m+n+1}$, while both input variable $s = j\omega$ and the fitting output $H(s;\boldsymbol{x})$ of system responses belong to the complex number field, $s \in \mathbb{C}$ and $H(s;\boldsymbol{x}) \in \mathbb{C}$.

The problem becomes finding an optimal solution to the non-linear mathematical system:

$$r(s;\boldsymbol{x}) = \check{H}(s) - H(s;\boldsymbol{x}), \tag{4.24}$$

$$\boldsymbol{x}_* = \arg\min_{\boldsymbol{x}} \|r(s;\boldsymbol{x})\|^2, \tag{4.25}$$

where $r(s;\boldsymbol{x})$ is the non-linear residual function, and $\boldsymbol{x}_*$ is the optimal solution to minimize the Euclidean norm in the complex number field.

In practical application, the outcome of system response collected from CAD simulation and VNA measurement is a set of discrete data in the frequency domain. The number of data is always much larger than the dimensions of the unknown coefficient vector $\boldsymbol{x}$. Thus, the problem is optimising of a non-linear overdetermined system in mathematics.

Unfortunately, in accordance with the principle of least squares, the direct solution of a non-linear system is computationally intractable. Here, an approximation method is used to keep the linearity of the residual function shown as:

$$r_m(s;\boldsymbol{x}) = \check{H}(s) \cdot D(s;\boldsymbol{x}) - N(s;\boldsymbol{x}), \tag{4.26}$$

$$\boldsymbol{x}_{m*} = \arg\min_{\boldsymbol{x}} \|r_m(s;\boldsymbol{x})\|^2, \tag{4.27}$$

where $r_m(s;\boldsymbol{x})$ is the modified linear residual function, and $\boldsymbol{x}_{m*}$ denotes the corresponding optimal solution.

With the practical discrete data to further solve this problem, Equation (4.26) can be expressed as the typical matrix form,

$$r_{m,i} = \check{H}(s_i) \cdot D(s_i;\boldsymbol{x}) - N(s_i;\boldsymbol{x}), (1 \le i \le K) \tag{4.28}$$

$$r_{m,i} = b_i - \sum_{j=1}^{m+n+1} a_{ij}x_j, \tag{4.29}$$

$$\boldsymbol{r}_m = \boldsymbol{b} - \boldsymbol{A} \cdot \boldsymbol{x}, \tag{4.30}$$

where $\boldsymbol{A} \in \mathbb{C}^{K\times(m+n+1)}$, $\boldsymbol{b} \in \mathbb{C}^K$, and K is the number of data in the frequency domain.

The least square method minimizes the cost function

$$\begin{aligned} f(x) &= \sum_{i=1}^{K} \left|r_i\right|^2 \\ &= \sum_{i=1}^{K} r_i \cdot r_i^* \\ &= \sum_{i=1}^{K} (b_i - \sum_{j=1}^{m+n+1} a_{ij}x_j) \cdot (b_i^* - \sum_{j=1}^{m+n+1} a_{ij}^* x_j) \end{aligned} \tag{4.31}$$

The minimum is attained when all partial derivatives of $f(x)$ with respect to each component x_k vanish,

$$\begin{aligned} 0 =& \frac{\partial f}{\partial x_k} \qquad (\forall k) \\ =& \sum_{i=1}^{K} (b_i^* - \sum_{j=1}^{m+n+1} a_{ij}^* x_j) \cdot (-a_{ik}) + \sum_{i=1}^{K} (b_i - \sum_{j=1}^{m+n+1} a_{ij}x_j) \cdot (-a_{ik}^*) \\ =& \sum_{i=1}^{K} \sum_{j=1}^{m+n+1} a_{ij}^* a_{ik} x_j + \sum_{i=1}^{K} \sum_{j=1}^{m+n+1} a_{ij} a_{ik}^* x_j - \sum_{i=1}^{K} \sum_{j=1}^{m+n+1} b_i^* a_{ik} - \sum_{i=1}^{K} \sum_{j=1}^{m+n+1} b_i a_{ik}^* \end{aligned} \tag{4.32}$$

Rearranging terms in a compact form as

$$\boldsymbol{A}^T\boldsymbol{A}^*\boldsymbol{x} + \boldsymbol{A}^H\boldsymbol{A}\boldsymbol{x} = \boldsymbol{A}^T\boldsymbol{b}^* + \boldsymbol{A}^H\boldsymbol{b} \tag{4.33}$$

If $\boldsymbol{A}$ has full column rank and the matrix $(\boldsymbol{A}^T\boldsymbol{A}^* + \boldsymbol{A}^H\boldsymbol{A})$ is invertible, the solution of Equation (4.33) is

$$\boldsymbol{x}_{m*} = (\boldsymbol{A}^T\boldsymbol{A}^* + \boldsymbol{A}^H\boldsymbol{A})^{-1} \cdot (\boldsymbol{A}^T\boldsymbol{b}^* + \boldsymbol{A}^H\boldsymbol{b}) \tag{4.34}$$

Subsequently, setting $\boldsymbol{A} = \boldsymbol{A}_1 + j\boldsymbol{A}_2$,$\boldsymbol{b} = \boldsymbol{b}_1 + j\boldsymbol{b}_2$, where $\boldsymbol{A}_1, \boldsymbol{A}_2 \in \mathbb{R}^{K\times(m+n+1)}$, and $\boldsymbol{b}_1, \boldsymbol{b}_2 \in \mathbb{R}^K$,

$$\boldsymbol{A}^T = \boldsymbol{A}_1^T + j\boldsymbol{A}_2^T \tag{4.35}$$

$$\boldsymbol{A}^* = \boldsymbol{A}_1 - j\boldsymbol{A}_2 \tag{4.36}$$

$$\boldsymbol{A}^H = \boldsymbol{A}_1^T - j\boldsymbol{A}_2^T \tag{4.37}$$

$$\boldsymbol{b}^* = \boldsymbol{b}_1 - j\boldsymbol{b}_2 \tag{4.38}$$

Equation (4.34) can be simplified and expressed only using real number notations,

$$\begin{aligned}\boldsymbol{x}_{m*} =& (\boldsymbol{A}^T\boldsymbol{A}^* + \boldsymbol{A}^H\boldsymbol{A})^{-1} \cdot (\boldsymbol{A}^T\boldsymbol{b}^* + \boldsymbol{A}^H\boldsymbol{b}) \\ =& [(\boldsymbol{A}_1^T + j\boldsymbol{A}_2^T)(\boldsymbol{A}_1 - j\boldsymbol{A}_2) + (\boldsymbol{A}_1^T - j\boldsymbol{A}_2^T)(\boldsymbol{A}_1 + j\boldsymbol{A}_2)]^{-1} \\ & \cdot [(\boldsymbol{A}_1^T + j\boldsymbol{A}_2^T)(\boldsymbol{b}_1 - j\boldsymbol{b}_2) + (\boldsymbol{A}_1^T - j\boldsymbol{A}_2^T)(\boldsymbol{b}_1 + j\boldsymbol{b}_2)] \\ =& 4 \cdot (\boldsymbol{A}_1^T\boldsymbol{A}_1^* + \boldsymbol{A}_2^T\boldsymbol{A}_2)^{-1} \cdot (\boldsymbol{A}_1^T\boldsymbol{b}_1 + \boldsymbol{A}_2^T\boldsymbol{b}_2)\end{aligned} \tag{4.39}$$

Therefore, $\boldsymbol{x}$ could be figured out as a real result from Equation (4.39) and it will take less runtime.

4.2.2 Weighting Correction

To offset the linear approximation without denominator polynomial in Equation (4.26), a compensatory weighting factor $\boldsymbol{W}_d$ is defined as a $K \times K$ diagonal matrix,

$$\boldsymbol{W}_d = diag\left\{\frac{1}{\left|D(s_i;\boldsymbol{x})\right|^2}\right\}. \tag{4.40}$$

Meanwhile, a relative weighting factor $\boldsymbol{W}_r$ is defined for particular research requirements, where some of the simulated or measured data may be treated with more significance than others. For example, in microwave and RF areas, the data at frequencies where return loss exceeds 10dB may be more important than others, because they are considered to be in the working band. The relative weighting factor $\boldsymbol{W}_r$ could be set as a $K \times K$ diagonal matrix, $\boldsymbol{W}_r = diag\left\{\frac{1}{\left|S_{11}(s_i;\boldsymbol{x})\right|^k}\right\}, (k > 1)$. For another example about notched-band, researchers always care more about the

stop-band region where the return loss value is approaching 0dB. Similarly, the relative weighting factor $\boldsymbol{W}_r$ could be set as $\boldsymbol{W}_r = diag\left\{\left|S_{11}(s_i;\boldsymbol{x})\right|^k\right\}, (k>1)$ to make the fitting curve in a notched-band region more accurate. Therefore, for various scenarios and different requirements, the relative weighting factor $\boldsymbol{W}_r$ is made variable to give this approach more flexibility.

Both the compensatory weighting factor $\boldsymbol{W}_d$ and the relative weighting factor $\boldsymbol{W}_r$ compose a weighting factor $\boldsymbol{W}$, as

$$\boldsymbol{W} = \boldsymbol{W}_d \cdot \boldsymbol{W}_r \quad . \tag{4.41}$$

After considering the hybrid number field and the weighting factor $\boldsymbol{W}$, the least squares optimal solution is

$$\boldsymbol{x}_{m*} = (\boldsymbol{A}_{\boldsymbol{w}}^T \boldsymbol{A}_{\boldsymbol{w}}^* + \boldsymbol{A}_{\boldsymbol{w}}^H \boldsymbol{A}_{\boldsymbol{w}})^{-1} \cdot (\boldsymbol{A}_{\boldsymbol{w}}^T \boldsymbol{b}_{\boldsymbol{w}}^* + \boldsymbol{A}_{\boldsymbol{w}}^H \boldsymbol{b}_{\boldsymbol{w}}), \tag{4.42}$$

where $\boldsymbol{A}_{\boldsymbol{w}} = \boldsymbol{W} \cdot \boldsymbol{A}$, and $\boldsymbol{b}_{\boldsymbol{w}} = \boldsymbol{W} \cdot \boldsymbol{b}$.

Subsequently, decomposing $\boldsymbol{A} = \boldsymbol{A}_1 + j\boldsymbol{A}_2$,$\boldsymbol{b} = \boldsymbol{b}_1 + j\boldsymbol{b}_2$, where $\boldsymbol{A}_1, \boldsymbol{A}_2 \in \mathbb{R}^{K\times(m+n+1)}$, and $\boldsymbol{b}_1, \boldsymbol{b}_2 \in \mathbb{R}^K$, Equation (4.42) can be simplified and be expressed only by real number notations,

$$\boldsymbol{x}_{m*} = 4 \cdot (\boldsymbol{A}_{\boldsymbol{1w}}^T \boldsymbol{A}_{\boldsymbol{1w}}^* + \boldsymbol{A}_{\boldsymbol{2w}}^T \boldsymbol{A}_{\boldsymbol{2w}})^{-1} \cdot (\boldsymbol{A}_{\boldsymbol{1w}}^T \boldsymbol{b}_{\boldsymbol{1w}} + \boldsymbol{A}_{\boldsymbol{2w}}^T \boldsymbol{b}_{\boldsymbol{2w}}), \tag{4.43}$$

where $\boldsymbol{A}_{\boldsymbol{1w}} = \boldsymbol{W} \cdot \boldsymbol{A}_1$, $\boldsymbol{A}_{\boldsymbol{2w}} = \boldsymbol{W} \cdot \boldsymbol{A}_2$, $\boldsymbol{b}_{\boldsymbol{1w}} = \boldsymbol{W} \cdot \boldsymbol{b}_1$, and $\boldsymbol{b}_{\boldsymbol{2w}} = \boldsymbol{W} \cdot \boldsymbol{b}_2$. Here the corresponding optimal solution $\boldsymbol{x}_{m*}$, totally expressed by notations in the real number field, could reduce computational runtime.

To quantify the fitting quality, variance σ^2 is defined as

$$\sigma^2 = \frac{1}{K}\sum_{i=1}^{K}\left|\check{H}(s_i) - H(s_i;\boldsymbol{x})\right|^2. \tag{4.44}$$

Whilst the variance σ^2 is merely related to the overall fitting performance, the detailed information of fitting performance has to be observed from the corresponding figures.

Since the weighting factor $\boldsymbol{W}$ is mutually determined by unknown coefficient vector $\boldsymbol{x}$, an iteration method has to be used to obtain their accurate value gradually. Figure 4.1 is a flow chart illustrating this iterative process, where the blue boxes can be set as a precision requirement and specific scenario.

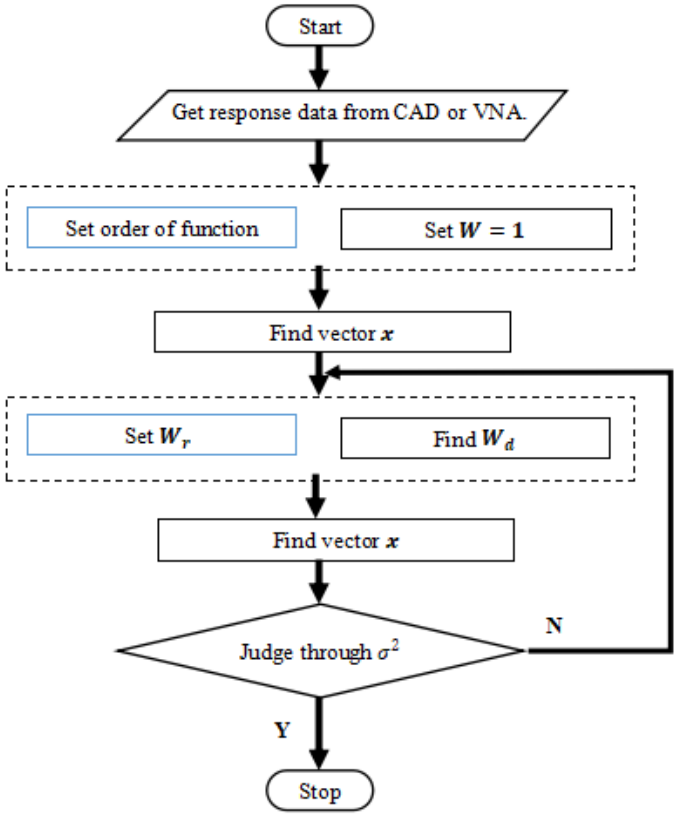

FIGURE 4.1: Flow chart of the iterative process.

4.3 Summary

A generic approach has been proposed to specifically obtain analytical rational function in the complex field for microwave systems. Based on linear least squares fitting and iteration, this approach is extended from real field to complex field step by step. Its flexible weighting factor and elastic order could adapt to the strict requirements and complicated scenarios, which could be seen from the antenna applications in Chapter 6, Chapter 7, and Chapter 8. Additionally, the analytical rational function is a bridge between discrete numerical data of system response and its corresponding equivalent circuit. In Chapter 5, some methods converting rational function to the equivalent circuit are further discussed.

Chapter 5

Equivalent Circuit & Network Analysis

An equivalent circuit/network is an important tool for analyzing the electromagnetic structure in the microwave area. The equivalent circuit model of a narrow band system is easily constructed, while the equivalent circuit model of a broadband system is too intricate to obtain.

This chapter proposes some methods of obtaining equivalent circuits from an analytical rational function. The analytical rational function is fitting to the discrete observable data in Chapter 4. The conversion from the rational function to an equivalent circuit is not unique. The converted equivalent circuit topologies and processes are various, while the conversion from the circuit topology to the rational function is unique. Furthermore, the multi-port equivalent network analysis is developed. The equivalent circuit method is applied in a chassis antenna in Chapter 6, and the equivalent network analysis is applied in a reconfigurable UWB antenna in Chapter 8.

5.1 Directly Translated Method

A novel method, named Directly Translated Method (DTM), has been developed among the methods for converting from the rational function to the equivalent circuit. It leads to the least number of lumped components in the equivalent circuit. The circuit topologies based on the Directly Translated Method are not unique but various, and they have many types of lumped components and different groups of the same type of components. To simplify the thesis structure, the general forms are only shown in this chapter, while the basic forms are shown in the Appendix B.1.

5.1.1 Group of Resistors and Capacitors

The resistor and capacitor are the standard lumped components. The equivalent circuit composed of resistor(s) and capacitor(s) is easy to realize on the computer and

in reality. The order of the rational function is an essential factor in determining the topology. The definition and the type of the rational function in Equation (4.15) is used in the following.

$m = n$ (General Formula)

The n-order rational function is as:

$$Z(s) = \frac{s^n + b_1 s^{n-1} + \cdots + b_i s^{n-i} + \cdots + b_n}{a_1 s^n + a_2 s^{n-1} + \cdots + a_j s^{n+1-j} + \cdots + a_{n+1}} \tag{5.1}$$

It can convert to the equivalent circuit topology within resistors and capacitors in Figure 5.1. Each branch's current of the equivalent circuit through Kirchhoff's Current/Voltage Laws is marked in Figure 5.2.

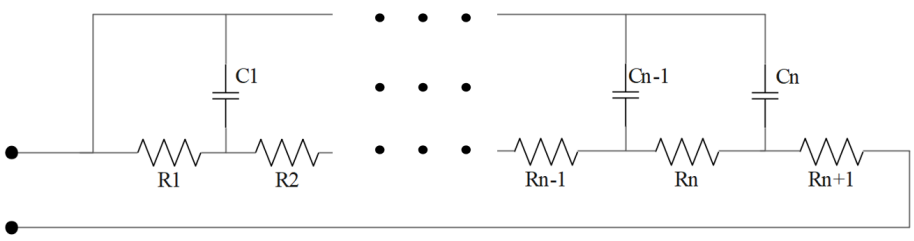

FIGURE 5.1: Equivalent circuit composed of resistors and capacitors for (n, n)-order rational function.

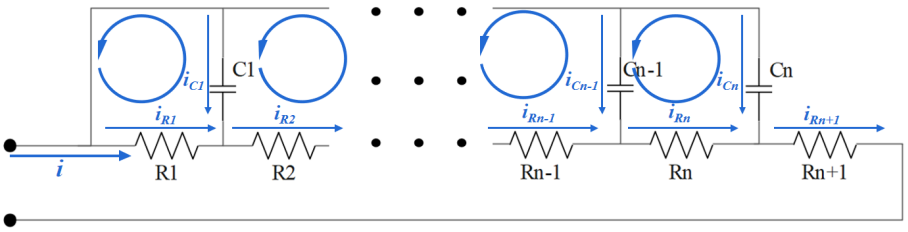

FIGURE 5.2: The current in equivalent circuit composed of resistors and capacitors for n-order rational function.

Based on Kirchhoff's Current Law (KCL), the equations are

$$\begin{cases} i_{R_{n+1}} = i \\ i_{C_1} + i_{R_1} - i_{R_2} = 0 \\ i_{C_2} + i_{R_2} - i_{R_3} = 0 \\ \vdots \quad \vdots \quad \vdots \qquad (1 \le j \le n) \\ i_{C_j} + i_{R_j} - i_{R_{j+1}} = 0 \\ \vdots \quad \vdots \quad \vdots \\ i_{C_n} + i_{R_n} - i_{R_{n+1}} = 0 \end{cases} \tag{5.2}$$

Based on Kirchhoff's Voltage Law (KVL), the equations are

$$\begin{cases} -\dfrac{1}{sC_1} i_{C_1} + R_1 i_{R_1} = 0 \\ \dfrac{1}{sC_1} i_{C_1} - \dfrac{1}{sC_2} i_{C_2} + R_2 i_{R_2} = 0 \\ \vdots \quad \vdots \quad \vdots \\ \dfrac{1}{sC_j} i_{C_j} - \dfrac{1}{sC_{j+1}} i_{C_{j+1}} + R_{j+1} i_{R_{j+1}} = 0 \qquad (1 \le j \le (n-1)) \\ \vdots \quad \vdots \quad \vdots \\ \dfrac{1}{sC_{n-1}} i_{C_{n-1}} - \dfrac{1}{sC_n} i_{C_n} + R_n i_{R_n} = 0 \end{cases} \tag{5.3}$$

To solve the problem clearly, Equations (5.2) and Equation (5.3) can be spliced together and expressed as the type of matrix equation,

$$\begin{bmatrix} & & & & & & & & & & & & 1 \\ 1 & & & & & & 1 & -1 & & & & & \\ & 1 & & & & & & 1 & -1 & & & & \\ & & \ddots & & & & & & \ddots & \ddots & & & \\ & & & \ddots & & & & & & \ddots & \ddots & & \\ & & & & & 1 & & & & & 1 & -1 & \\ -\frac{1}{sC_1} & & & & & & R_1 & & & & & & \\ \frac{1}{sC_1} & -\frac{1}{sC_2} & & & & & & R_2 & & & & & \\ & \ddots & \ddots & & & & & & \ddots & & & & \\ & & \ddots & \ddots & & & & & & \ddots & & & \\ & & & \frac{1}{sC_{n-1}} & -\frac{1}{sC_n} & & & & & & R_n & & \end{bmatrix} \begin{bmatrix} i_{C_1} \\ i_{C_2} \\ i_{C_3} \\ \vdots \\ i_{L_n} \\ i_{R_1} \\ i_{R_2} \\ i_{R_3} \\ \vdots \\ \vdots \\ i_{R_{n+1}} \end{bmatrix} = \begin{bmatrix} i \\ 0 \\ 0 \\ \vdots \\ \vdots \\ \vdots \\ \vdots \\ \vdots \\ \vdots \\ 0 \end{bmatrix} \tag{5.4}$$

The equivalent impedance of the circuit can be expressed by the lumped components,

$$Z(s) = \frac{\sum_j R_j i_{R_j}}{i}. \tag{5.5}$$

5.1.2 Group of Resistors and Capacitors II

To illustrate the diversity of the conversion from the rational function to its equivalent circuit, another circuit within resistors and capacitors but a different topology is discussed.

$m = n$ (General Formula)

The n-order rational function is as:

$$Z(s) = \frac{s^n + b_1 s^{n-1} + \cdots + b_i s^{n-i} + \cdots + b_n}{a_1 s^n + a_2 s^{n-1} + \cdots + a_j s^{n+1-j} + \cdots + a_{n+1}} \tag{5.6}$$

It can convert to the equivalent circuit topology within resistors and capacitors in Figure 5.3. Each branch's current of the equivalent circuit through Kirchhoff's Current/Voltage Laws is marked in Figure 5.4.

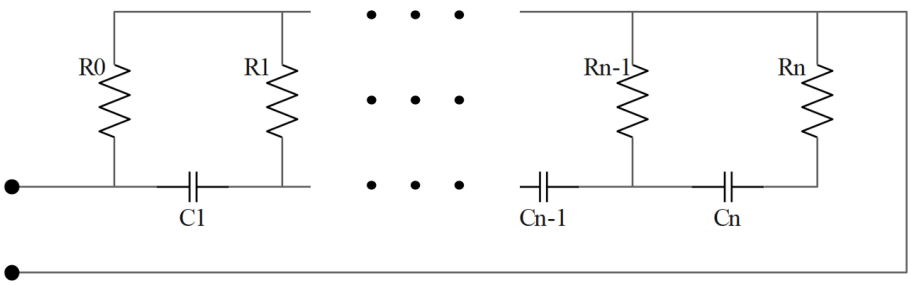

FIGURE 5.3: Equivalent circuit composed of resistors and capacitors for n-order rational function.

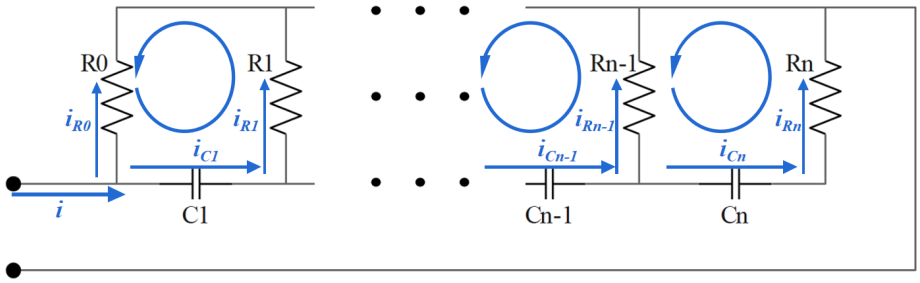

FIGURE 5.4: The current in equivalent circuit composed of resistors and capacitors for n-order rational function.

Based on Kirchhoff's Current Law (KCL), the equations are

$$\begin{cases} i_{C_1} + i_{R_0} = i \\ i_{C_1} - i_{C_2} - i_{R_1} = 0 \\ i_{C_2} - i_{C_3} - i_{R_2} = 0 \\ \quad \vdots \qquad \vdots \qquad \vdots \\ i_{C_j} - i_{C_{j+1}} - i_{R_j} = 0 \\ \quad \vdots \qquad \vdots \qquad \vdots \\ i_{C_{n-1}} - i_{C_n} - i_{R_{n-1}} = 0 \\ i_{C_n} - i_{R_n} = 0 \end{cases} \qquad (1 \le j \le (n-1)) \tag{5.7}$$

Based on Kirchhoff's Voltage Law (KVL), the equations are

$$\begin{cases} \frac{1}{sC_1} i_{C_1} - R_0 i_{R_0} + R_1 i_{R_1} = 0 \\ \frac{1}{sC_2} i_{C_2} - R_1 i_{R_1} + R_2 i_{R_2} = 0 \\ \quad \vdots \qquad\quad \vdots \qquad\qquad \vdots \\ \frac{1}{sC_j} i_{C_j} - R_{j-1} i_{R_{j-1}} + R_j i_{R_j} = 0 \\ \quad \vdots \qquad\quad \vdots \qquad\qquad \vdots \\ \frac{1}{sC_n} i_{C_n} - R_{n-1} i_{R_{n-1}} + R_n i_{R_n} = 0 \end{cases} \qquad (1 \le j \le n) \tag{5.8}$$

To solve the problem clearly, Equations (5.7) and Equation (5.8) can be spliced together and expressed as the type of matrix equation,

$$\begin{bmatrix} 1 & & & & & 1 & & & & & \\ 1 & -1 & & & & & -1 & & & & \\ & 1 & -1 & & & & & -1 & & & \\ & & \ddots & \ddots & & & & & \ddots & & \\ & & & 1 & -1 & & & & & -1 & \\ & & & & 1 & & & & & & -1 \\ \frac{1}{sC_1} & & & & & -R_0 & R_1 & & & & \\ & \frac{1}{sC_2} & & & & & -R_1 & R_2 & & & \\ & & \ddots & & & & & \ddots & \ddots & & \\ & & & \ddots & & & & & \ddots & \ddots & \\ & & & & \frac{1}{sC_n} & & & & & -R_{n-1} & R_n \end{bmatrix} \begin{bmatrix} i_{C_1} \\ i_{C_2} \\ i_{C_3} \\ \vdots \\ i_{C_n} \\ i_{R_0} \\ i_{R_1} \\ i_{R_2} \\ \vdots \\ \vdots \\ i_{R_n} \end{bmatrix} = \begin{bmatrix} i \\ 0 \\ 0 \\ \vdots \\ \vdots \\ \vdots \\ \vdots \\ \vdots \\ \vdots \\ 0 \end{bmatrix} \tag{5.9}$$

The equivalent impedance of the circuit can be expressed by the lumped components,

$$Z(s) = \frac{R_0 \cdot i_{R_0}}{i} \tag{5.10}$$

5.1.3 Group of Resistors and Inductors

The rational function is also converted to an equivalent circuit composed of the resistors and inductors.

$m = n$ (General Formula)

The n-order rational function is as:

$$Z(s) = \frac{s^n + b_1 s^{n-1} + \cdots + b_i s^{n-i} + \cdots + b_n}{a_1 s^n + a_2 s^{n-1} + \cdots + a_j s^{n+1-j} + \cdots + a_{n+1}} \tag{5.11}$$

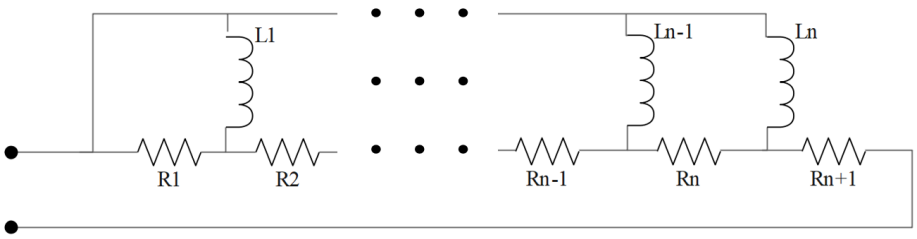

FIGURE 5.5: Equivalent circuit composed of resistors and inductors for n-order rational function.

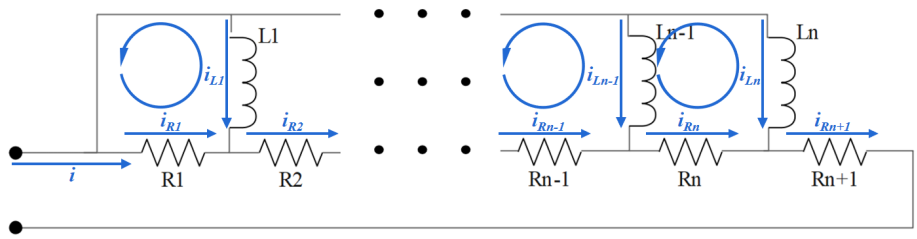

FIGURE 5.6: The current in equivalent circuit composed of resistors and inductors for n-order rational function.

It can convert to the equivalent circuit topology within resistors and inductors in Figure 5.5. Each branch's current of the equivalent circuit through Kirchhoff's Current/Voltage Laws is marked in Figure 5.6.

Based on Kirchhoff's Current Law (KCL), the equations are

$$\begin{cases} i_{R_{n+1}} = i \\ i_{L_1} + i_{R_1} - i_{R_2} = 0 \\ i_{L_2} + i_{R_2} - i_{R_3} = 0 \\ \vdots \quad \vdots \quad \vdots \qquad (1 \le j \le n) \\ i_{L_j} + i_{R_j} - i_{R_{j+1}} = 0 \\ \vdots \quad \vdots \quad \vdots \\ i_{L_n} + i_{R_n} - i_{R_{n+1}} = 0 \end{cases} \tag{5.12}$$

Based on Kirchhoff's Voltage Law (KVL), the equations are

$$\begin{cases} -sL_1 i_{L_1} + R_1 i_{R_1} = 0 \\ sL_1 i_{L_1} - sL_2 i_{L_2} + R_2 i_{R_2} = 0 \\ \quad \vdots \qquad\quad \vdots \qquad\quad \vdots \\ sL_j i_{L_j} - sL_{j+1} i_{L_{j+1}} + R_{j+1} i_{R_{j+1}} = 0 \\ \quad \vdots \qquad\quad \vdots \qquad\quad \vdots \\ sL_{n-1} i_{L_{n-1}} - sL_n i_{L_n} + R_n i_{R_n} = 0 \end{cases} \qquad (1 \le j \le (n-1)) \tag{5.13}$$

To solve the problem clearly, Equations (5.12) and Equation (5.13) can be spliced together and expressed as the type of matrix equation,

$$\begin{bmatrix} & & & & & & & & & & & & 1 \\ 1 & & & & & & 1 & -1 & & & & & \\ & 1 & & & & & & 1 & -1 & & & & \\ & & \ddots & & & & & & \ddots & \ddots & & & \\ & & & \ddots & & & & & & \ddots & \ddots & & \\ & & & & 1 & & & & & & 1 & -1 & \\ -sL_1 & & & & & & R_1 & & & & & & \\ sL_1 & -sL_2 & & & & & & R_2 & & & & & \\ & \ddots & \ddots & & & & & & \ddots & & & & \\ & & \ddots & \ddots & & & & & & \ddots & & & \\ & & & sL_{n-1} & -sL_n & & & & & & R_n & & \end{bmatrix} \begin{bmatrix} i_{L_1} \\ i_{L_2} \\ i_{L_3} \\ \vdots \\ i_{L_n} \\ i_{R_1} \\ i_{R_2} \\ i_{R_3} \\ \vdots \\ \vdots \\ i_{R_{n+1}} \end{bmatrix} = \begin{bmatrix} i \\ 0 \\ 0 \\ \vdots \\ \vdots \\ \vdots \\ \vdots \\ \vdots \\ \vdots \\ 0 \end{bmatrix} \tag{5.14}$$

The equivalent impedance of the circuit can be expressed by the lumped components,

$$Z(s) = \frac{\sum_j R_j i_{R_j}}{i} \tag{5.15}$$

5.2 Partial Fraction Expansion Method

Partial Fraction Expansion (PFE) is a common method in the microwave area [86], and it can also be used here to convert the rational function to an equivalent circuit. $Z(s)$ is a rational function of s to denote the equivalent impedance. When $m \ge n$, $Z(s)$ is improper; when $m < n$, $Z(s)$ is proper. The improper rational function

can become proper after separating a polynomial. The proper rational function can decompose into simple rational functions through PFE,

$$\begin{aligned} Z(s) =& \frac{Numerator(s,m)}{Denominator(s,n)} \\ =& \frac{Numerator(s,m)}{(S-\lambda_1)^{r_1}(s-\lambda_2)^{r_2}\cdots(s-\lambda_n)^{r_n}} \\ =& \frac{K(\lambda_1,r_1)}{(s-\lambda_1)^{r_1}} + \frac{K(\lambda_1,r_1-1)}{(s-\lambda_1)^{r_1-1}} + \cdots + \frac{K(\lambda_1,1)}{s-\lambda_1} \\ &+ \frac{K(\lambda_2,r_2)}{(s-\lambda_2)^{r_2}} + \frac{K(\lambda_2,r_2-1)}{(s-\lambda_2)^{r_2-1}} + \cdots + \frac{K(\lambda_2,1)}{s-\lambda_2} \\ &\cdots \qquad \cdots \qquad \cdots \\ &+ \frac{K(\lambda_n,r_n)}{(s-\lambda_n)^{r_n}} + \frac{K(\lambda_n,r_n-1)}{(s-\lambda_n)^{r_n-1}} + \cdots + \frac{K(\lambda_n,1)}{s-\lambda_n} \\ =& \sum_{i=1}^{n}\sum_{j=1}^{r_i} \frac{K(\lambda_i,j)}{(s-\lambda_i)^j} \end{aligned} \tag{5.16}$$

$$K(\lambda_i, r_i - j) = \frac{1}{j!}\cdot\frac{d^j}{ds^j}[(s-\lambda_i)^{r_i}\cdot Z(s)]\Big|_{s=\lambda_i} \tag{5.17}$$

Equation (5.16) is the sum of many simpler rational functions. In other words, the large-scale equivalent circuit of the initial complicated rational function is equal to a cascade of many small-scale equivalent circuits converted from the simpler rational functions.

Compared with the Directly Translated Method, the Partial Fraction Expansion Method has fewer steps. However, the equivalent circuit through the Partial Fraction Expansion Method contains more components than that through the Directly Translated Method.

5.3 Continued Fraction Method

Continued Fraction (CF) is also named: successive division, division algorithm, and Euclidean algorithm. It can also obtain the corresponding equivalent circuit [87]. The equivalent circuit topologies are still various through the Continued Fraction Method. To obtain the correct result, the process of Continued Fraction must follow the explicit topology. To simplify the thesis structure, the general forms are only shown here, while the basic forms are shown in the Appendix B.2.

n-order rational function (for Programme)

For n-order rational function, the equivalent circuit topology is as Figure 5.1, so the equivalent impedance is obtained from its lower-order equivalent impedance.

$$\begin{cases} Z^{(0)} = R_1 \\ Z^{(1)} = R_2 + \dfrac{1}{sC_1 + \dfrac{1}{Z^{(0)}}} \\ Z^{(2)} = R_3 + \dfrac{1}{sC_2 + \dfrac{1}{Z^{(1)}}} \\ \qquad \vdots \\ Z^{(i)} = R_{i+1} + \dfrac{1}{sC_i + \dfrac{1}{Z^{(i-1)}}} \end{cases} \tag{5.18}$$

For the rational function with the exact order number, the function could be determined by the coefficients of denominator polynomial and numerator polynomial. Thus, such coefficients are extracted to represent the initial rational function for the following calculation,

$$Z^{(i)} = \frac{N^{(i)}}{D^{(i)}} = \frac{[N_i^{(i)}, N_{i-1}^{(i)}, \cdots, N_j^{(i)}, \cdots, N_1^{(i)}, N_0^{(i)}]}{[D_i^{(i)}, D_{i-1}^{(i)}, \cdots, D_j^{(i)}, \cdots, D_1^{(i)}, D_0^{(i)}]}, \qquad (0 \le j \le i) \tag{5.19}$$

The lower-order rational function of the initial function is

$$Z^{(i-1)} = \frac{N^{(i-1)}}{D^{(i-1)}} = \frac{[N_{i-1}^{(i-1)}, N_{i-2}^{(i-1)}, \cdots, N_j^{(i-1)}, \cdots, N_1^{(i-1)}, N_0^{(i-1)}]}{[D_{i-1}^{(i-1)}, D_{i-2}^{(i-1)}, \cdots, D_j^{(i-1)}, \cdots, D_1^{(i-1)}, D_0^{(i-1)}]}, \quad (0 \le j \le (i-1)) \tag{5.20}$$

Based on the Continued Fraction Method, the resistor and capacitor in Figure 5.1 are

$$R_{i+1} = \frac{N_i^{(i)}}{D_i^{(i)}} \tag{5.21}$$

$$C_i = \frac{D_i^{(i)}}{N_{i-1}^{(i)} - R_{i+1} \cdot D_{i-1}^{(i)}} \tag{5.22}$$

After obtaining the resistor and capacitor in i-level, the rational function can be de-levelled,

$$N_j^{(i-1)} = N_j^{(i)} - R_{i+1} \cdot D_j^{(i)}, \qquad (0 \le j \le (i-1)) \tag{5.23}$$

$$D_j^{(i-1)} = D_j^{(i)} - C_i \cdot N_{j-1}^{(i-1)}, \qquad (1 \le j \le (i-1)) \tag{5.24}$$

$$D_0^{(i-1)} = D_0^{(i)} \tag{5.25}$$

So far, it accesses a new loop with the same operations until the last 1-order rational function.

The Continued Fraction looks easier than DTM and PFE since there is no huge matrix and partial calculation. However, its precision is not good for a high-order function because of the truncation error.

5.4 Additions

5.4.1 Hybrid Method

Because of the diversity of the conversion from the rational function to its equivalent circuit, there are many kinds of methods, not limited to DTM, PFE, and CF. Each of them could obtain the equivalent circuit. They have their own pros and cons. In practice, in order to obtain a specific circuit topology with less time, multiple methods could be chosen. The large-scale circuit could be cut into several small sections, and each section could use a particular method.

5.4.2 Order of Rational Function

The previous sections in this chapter have discussed the conversion from rational function to equivalent circuit. All of them are chosen the (n, n)-order rational function, which only covers part of orders. In the following, other possible orders are discussed.

I. $0 \le m < n$

(I.A) $0 < m < n$

The rational function is a proper fraction,

$$\begin{aligned} Z =& \frac{s^m + b_1 s^{m-1} + \cdots + b_i s^{m-i} + \cdots + b_m}{a_1 s^n + a_2 s^{n-1} + \cdots + a_j s^{n+1-j} + \cdots + a_{n+1}} \\ =& \frac{s^m + \sum_{j=1}^{m} b_j s^{m-j}}{\sum_{j=1}^{n+1} a_j s^{n+1-j}} \end{aligned} \tag{5.26}$$

(I.B) $0 = m < n$

The rational function is a proper fraction,

$$Z = \frac{1}{\sum_{j=1}^{n+1} a_j s^{n+1-j}} \tag{5.27}$$

II. $m = n$

(II.A) $m = n \neq 0$

The rational function could be simplified as the sum of one constant and one proper fraction,

$$Z = \frac{1}{a_1} + \frac{\sum_{j=1}^{n} (b_j - \frac{a_{j+1}}{a_1}) s^{n-j}}{\sum_{j=1}^{n+1} a_j s^{n+1-j}} \tag{5.28}$$

(II.B) $m = n = 0$

The rational function could be simplified as one constant,

$$Z = \frac{1}{a_1} \tag{5.29}$$

III. $m > n$

(III.A) $m > n > 0$

The rational function could be simplified as the sum of one polynomial and one proper fraction,

$$Z = \sum_{j=1}^{m-n+1} c_j s^{m-n+1-j} + \frac{\sum_{j=1}^{n} d_j s^{n-j}}{\sum_{j=1}^{n+1} a_j s^{n+1-j}} \tag{5.30}$$

(III.B) $m > n = 0$

The rational function could be simplified as one polynomial,

$$Z = \frac{s^m + \sum_{j=1}^{m} b_j s^{m-j}}{a_1} = \sum_{j=0}^{m} c_j s^{m-j} \tag{5.31}$$

For the proper fraction with arbitrary order, the method of obtaining an equivalent circuit is the same as the method of an m-order rational function in the case of some zero-coefficients. Therefore, the methods we have discussed before could cover all possible cases.

5.4.3 Negative Elements

The negative impedance converters (NIC) are proposed in reality and utilized in antenna design in [63]. NIC can generate negative capacitances and negative inductances by active elements in [15]. In this chapter, in order to make the theory succinct and clear, the negative impedance is not considered independently. The negative capacitance is regarded as inductance, and the negative inductance is regarded as capacitance. Although the negative element is easily dealt with in mathematics, it may become a problem in the simulation since some commercial software does not allow the electronic components to be negative. Therefore, for this issue, negative elements can be replaced by a group circuit within a controlled source.

For the broad frequency band system, negative elements would be common in the circuit analysis, so it is necessary to discuss them.

I. negative resistor

A general resistor is defined as Equation (5.32) and it is shown in Figure 5.7.

$$U = R \cdot I \tag{5.32}$$

The negative resistor could be replaced by a group circuit of one positive resistor and one voltage control current source (VCCS), shown in Figure 5.8.

In Figure 5.8, the port current I is

$$I = I_R - I_S, \tag{5.33}$$

where I_R and I_S are the current through the resistor and the source, respectively.

The current of VCCS, I_S, is

$$I_S = g \cdot U \tag{5.34}$$

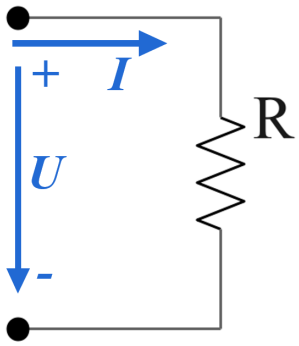

FIGURE 5.7: Definition of general resistor.

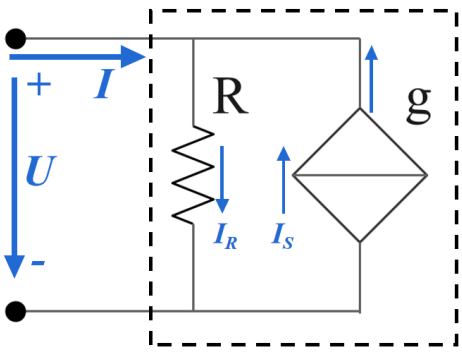

FIGURE 5.8: Group circuit of negative resistor.

The current of resistor I_R is

$$I_R = \frac{U}{R} \tag{5.35}$$

The equivalent resistance of the group composed of one positive resistor and one VCCS, R', is

$$R' = \frac{U}{I} = \frac{U}{\frac{U}{R} - g \cdot U} = \frac{R}{1 - g \cdot R} \tag{5.36}$$

If $g > \frac{1}{R}$, the equivalent resistance of the group circuit is negative, $R' < 0$.

II. negative capacitor

A general capacitor is defined as Equation (5.37) and it is shown in Figure 5.9.

$$I = C \cdot \frac{dU}{dt} \tag{5.37}$$

The negative capacitor could be replaced by a group circuit of one positive capacitor and one current-controlled current source (CCCS), shown in Figure 5.10.

In Figure 5.10, the port current I is

$$I = I_C - I_S \tag{5.38}$$

where I_C and I_S are the current through the capacitor and the source, respectively.

The current of the positive capacitor I_C is

$$I_C = C \cdot \frac{dU}{dt} \tag{5.39}$$

The current of the CCCS I_S is

$$I_S = \alpha \cdot I_C \tag{5.40}$$

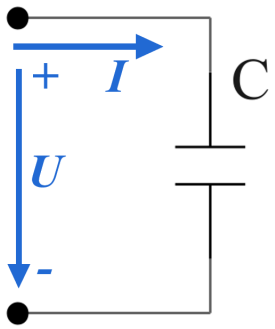

FIGURE 5.9: Definition of general capacitor.

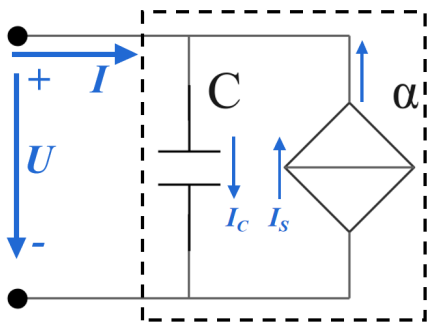

FIGURE 5.10: Group circuit of negative capacitor.

The port current could be expressed by the group circuit,

$$I = (1-\alpha)\cdot I_C = (1-\alpha)\cdot C\cdot\frac{dU}{dt} = C'\cdot\frac{dU}{dt} \tag{5.41}$$

The equivalent capacitance of the group circuit, C', is

$$C' = (1-\alpha)\cdot C \tag{5.42}$$

If $\alpha > 1$, the equivalent capacitance of the group circuit is negative, $C' < 0$.

III. negative inductor

A general inductor is defined as Equation (5.43) and it is shown in Figure 5.11.

$$U = L\cdot\frac{dI}{dt} \tag{5.43}$$

The negative inductor could be replaced by a group circuit of one positive inductor and one voltage control voltage source (VCVS), shown in Figure 5.12.

The voltage of the port is

$$U = L\cdot\frac{dI}{dt} \tag{5.44}$$

The voltage of the port U is also expressed by the voltage sum of the positive inductor and VCVS,

$$U = U_L - U_S \tag{5.45}$$

The voltage of the positive inductor is

$$U_L = L\cdot\frac{dI}{dt} \tag{5.46}$$

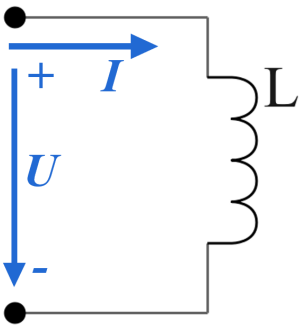

FIGURE 5.11: Definition of general inductor.

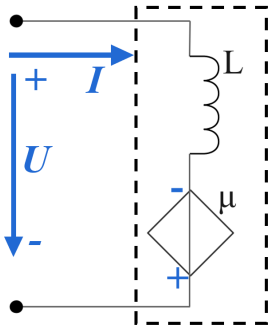

FIGURE 5.12: Group circuit of negative inductor.

The voltage of the VCVS U_S is

$$U_S = \mu \cdot U_L \tag{5.47}$$

The port voltage is also expressed as

$$U = (1-\mu) \cdot U_L = (1-\mu) \cdot L \cdot \frac{dI}{dt} = L' \cdot \frac{dI}{dt} \tag{5.48}$$

The equivalent inductance of the group circuit, L', is

$$L' = (1-\mu) \cdot L \tag{5.49}$$

If $\mu > 1$, the equivalent inductor of the group circuit is negative, $L' < 0$.

5.5 Multiport Equivalent Network

On the basis of conversion from rational function to equivalent circuit, the complicated electromagnetic structure could be researched by network analysis. From the perspective of the network, the system described by the rational function is a one-port network. For the multi-port network, the scattering matrix (S matrix) is an important tool to describe the system property. For instance, the S matrix of an n-port network is an $n \times n$ matrix. Especially, the rational function of the system response in the previous discussion is regarded as a 1×1 matrix. Therefore, the definition and the description of the system response are extended from one-port to multi-port network.

In [83], it indeed presents the method to denote the multi-port system, but its theory and examples are constant matrices. That means its system only works at a specific frequency or a very narrow band. When the constant elements of the S matrix are all extended to the functions of frequency, the S matrix can describe a broadband system. Each function of frequency could be obtained through the fitting method as the type of rational function. And then, on the basis of the conversion technique from rational function to an equivalent circuit, the multi-port equivalent circuit network is constructed to substitute the initial complicated broadband multi-port system.

5.5.1 Two-Port Network

For a two-port network, its scattering matrix (S matrix), impedance matrix (Z matrix) are 2×2 matrixes, and its equivalent network is configured in Figure 5.13, where Z_A, Z_B and Z_C are unknown functions.

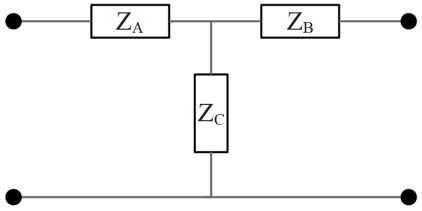

FIGURE 5.13: Equivalent circuit network of 2-port network.

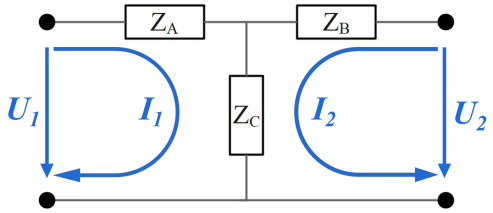

FIGURE 5.14: Current in equivalent circuit network of 2-port network.

The branch current and port voltage are marked in Figure 5.14. Based on Kirchhoff's Current/Voltage Laws, the equations are

$$\begin{cases} U_1 = Z_A \cdot I_1 + Z_C \cdot (I_1 + I_2) \\ U_2 = Z_B \cdot I_2 + Z_C \cdot (I_1 + I_2) \end{cases} \tag{5.50}$$

The equations are to rearrange terms as the port current (I_1, I_2)

$$\begin{cases} U_1 = (Z_A + Z_C) \cdot I_1 + Z_C \cdot I_2 \\ U_2 = Z_C \cdot I_1 + (Z_B + Z_C) \cdot I_2 \end{cases} \tag{5.51}$$

As the definition of impedance matrix (Z matrix) in [83], the Z matrix of the 2-port network in Figure 5.13 is

$$Z = \begin{bmatrix} Z_A + Z_C & Z_C \\ Z_C & Z_B + Z_C \end{bmatrix} \tag{5.52}$$

$$\begin{cases} Z_{11} = Z_A + Z_C \\ Z_{12} = Z_{21} = Z_C \\ Z_{22} = Z_B + Z_C \end{cases} \tag{5.53}$$

The elements of the Z matrix (Z_{11}, Z_{12}, Z_{21}, Z_{22}) are known conditions. In reality, the impedance matrix (Z matrix) could be obtained by measurement or by conversion from the scattering matrix (S matrix),

$$[Z] = ([U] + [S])([U] - [S])^{-1} \tag{5.54}$$

$$[S] = ([Z] + [U])^{-1}([Z] + [U]) \tag{5.55}$$

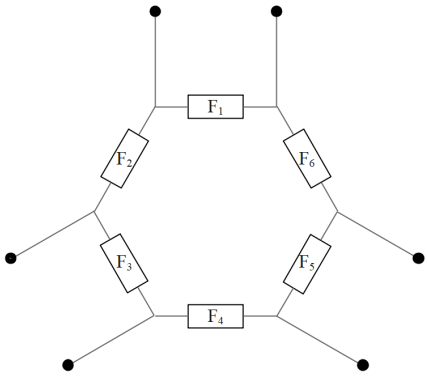

FIGURE 5.15: Equivalent circuit network of 3-port network.

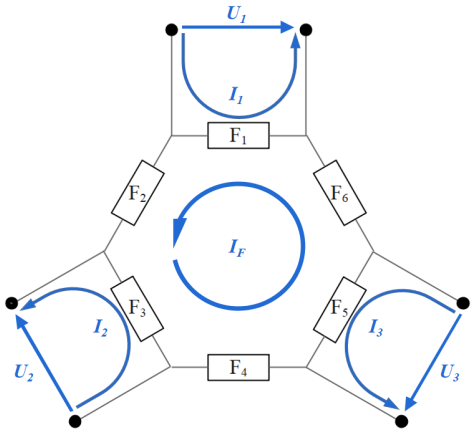

FIGURE 5.16: Current in equivalent circuit network of 3-port network.

Thus, the unknown functions (Z_A, Z_B, Z_C) can be expressed by these known elements (Z_{11}, Z_{12}, Z_{21}, Z_{22}),

$$\begin{cases} Z_A = Z_{11} - Z_{12} \\ Z_B = Z_{22} - Z_{12} \\ Z_C = Z_{12} \end{cases} \tag{5.56}$$

5.5.2 Three-Port Network

Likewise, for a three-port network, its scattering matrix (S matrix), impedance matrix (Z matrix) are 3×3 matrixes, and its equivalent network is configured in Figure 5.15, where there are 6 unknown functions (F_1, F_2, F_3, F_4, F_5, F_6).

The branch current and port voltage are marked in Figure 5.16. Based on Kirchhoff's Current/Voltage Laws, the equations are

$$\begin{cases} U_1 = F_1 \cdot (I_1 - I_F) \\ U_2 = F_3 \cdot (I_2 - I_F) \\ U_3 = F_5 \cdot (I_3 - I_F) \\ I_F \cdot \sum F_i = F_1 I_1 + F_3 I_2 + F_5 I_3 \end{cases} \tag{5.57}$$

The equations are to rearrange terms as the port current (I_1, I_2, I_3)

$$\begin{cases} U_1 = F_1 \cdot \dfrac{\sum F_i - F_1}{\sum F_i} \cdot I_1 - F_1 \cdot \dfrac{F_3}{\sum F_i} \cdot I_2 - F_1 \cdot \dfrac{F_5}{\sum F_i} \cdot I_3 \\ U_2 = -F_3 \cdot \dfrac{F_1}{\sum F_i} \cdot I_1 + F_3 \cdot \dfrac{\sum F_i - F_3}{\sum F_i} \cdot I_2 - F_3 \cdot \dfrac{F_5}{\sum F_i} \cdot I_3 \\ U_3 = -F_5 \cdot \dfrac{F_1}{\sum F_i} \cdot I_1 - F_5 \cdot \dfrac{F_3}{\sum F_i} \cdot I_2 + F_5 \cdot \dfrac{\sum F_i - F_5}{\sum F_i} \cdot I_3 \end{cases} \tag{5.58}$$

As the definition of impedance matrix (Z matrix) in [83], the Z matrix of the 3-port network in Figure 5.15 is

$$Z = \begin{bmatrix} \dfrac{F_1 \cdot (\sum F_i - F_1)}{\sum F_i} & -\dfrac{F_1 \cdot F_3}{\sum F_i} & -\dfrac{F_1 \cdot F_5}{\sum F_i} \\ -\dfrac{F_1 \cdot F_3}{\sum F_i} & \dfrac{F_3 \cdot (\sum F_i - F_3)}{\sum F_i} & -\dfrac{F_3 \cdot F_5}{\sum F_i} \\ -\dfrac{F_1 \cdot F_5}{\sum F_i} & -\dfrac{F_3 \cdot F_5}{\sum F_i} & \dfrac{F_5 \cdot (\sum F_i - F_5)}{\sum F_i} \end{bmatrix} \tag{5.59}$$

All elements of the Z matrix could be obtained by measurement or by conversion from the scattering matrix (S matrix) in Equation (5.54). Thus, the 6 unknown functions (F_1, F_2, F_3, F_4, F_5, F_6) can be expressed by the 6 known elements (Z_{11}, Z_{12}, Z_{13}, Z_{22}, Z_{23}, Z_{33}).

5.5.3 Multi-Port Network

Likewise, a multi-port network could be constructed. There is one matter worthy of attention. The topology of the multi-port network should take account into the degree of freedom in both known Z matrix and unknown functional components in topology. For example, Figure 5.17 shows a 4-port equivalent network, where F_9 and F_{10} are set to match the degree of freedom. Of course, the multi-port network topology is not unique.

5.6 Summary

The equivalent circuit model and equivalent network model have been developed on the basis of the rational function. Because of its graphical intuition, such equivalent models could be helpful in designing antennas and analyzing the electromagnetic property. Because the circuit and network follow the physical laws, such as

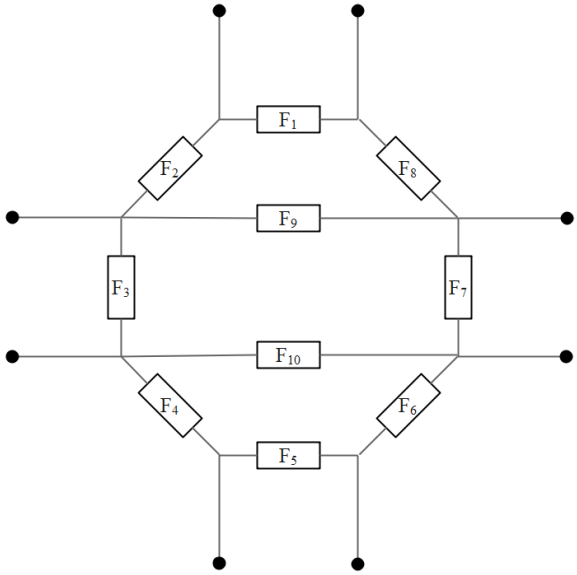

FIGURE 5.17: Equivalent circuit network of 4-port network.

Maxwell's Equations and Kirchhoff's Laws, it can be used to obtain a physics-based surrogate model in Chapter 8.

Chapter 6

Parameter Extraction from Traditional Antenna

A traditional antenna is simpler to analyse than a reconfigurable antenna since the traditional antenna does not have the complication of a tuning range. Therefore, deep research for a traditional antenna is valuable and necessary before researching the reconfigurable antenna.

In this chapter, there are two traditional antennas. One is a chassis antenna with two resonators, and the other is a band-notched ultra-wideband (UWB) pyramidal monopole antenna. Parameters and rational functions are extracted using the techniques developed in Chapter 4 and Chapter 5, and they can be used as surrogate models.

6.1 Application I

6.1.1 Antenna Design

The chassis antenna with a ground plane size of $100 \times 40mm^2$ and volumetric space of $40 \times 5 \times 7mm^3$ in [88], its structure shown in Figure 6.1, is composed of two resonators.

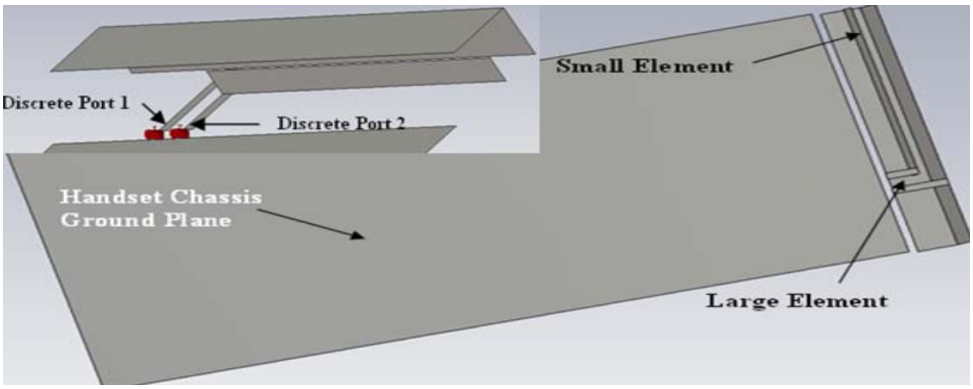

FIGURE 6.1: Geometry of the chassis antenna in [88].

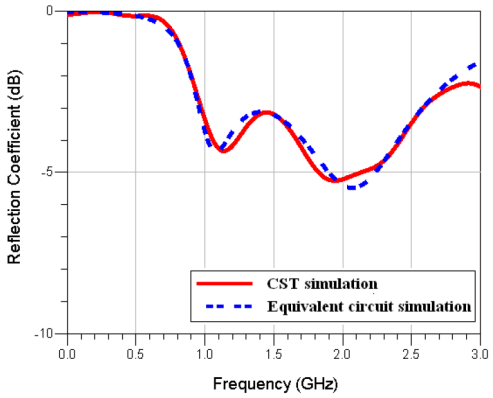

FIGURE 6.2: Reflection coefficient (dB) of the chassis antenna and equivalent circuit model in [88].

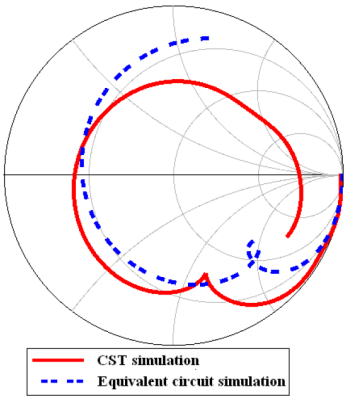

FIGURE 6.3: Smith chart of the chassis antenna and equivalent circuit model in [88].

TABLE 6.1: Unknown coefficient vector $\boldsymbol{x}$

Notation	a_1	a_2	a_3	a_4	a_5	a_6	a_7
Value	0.441	11.3	220	3751	22367	142906	23002
Notation	b_1	b_2	b_3	b_4	b_5	b_6	
Value	10.4	653	3588	82388	244445	2088511	

Due to coupling between resonators, the equivalent circuit becomes complicated, not simply assembling two independent equivalent circuits together. In [88], Dr Hu et al. plot the reflection coefficients of the chassis antenna in Figure 6.2 and Figure 6.3, and build the corresponding equivalent circuit through manual tuning. For this equivalent circuit, although the fitting of modulus in Figure 6.2 is acceptable, the fitting of the complex reflection coefficient on the Smith chart in Figure 6.3 deviates seriously from the electromagnetic simulation, which makes the equivalent circuit meaningless. Thus, a more accurate surrogate model is required.

6.1.2 Fitting and Extraction

For the rational function approximation, the higher-order function means the fitting can be better. However, considering the subsequent equivalent circuit analysis based on this fitting rational function, the lower-order rational function makes the equivalent circuit topology simpler. Moreover, the original discrete numerical data comes with the inevitable approximation and deviation during the simulation. Finally, to balance between fitting performance and equivalent circuit complexity, the order of the fitting rational function is set $m = n = 6$. The relative weighting factor $W_r = 1/|S_{11}^3|$ can emphasize the frequency band from $1GHz$ to $2.5GHz$.

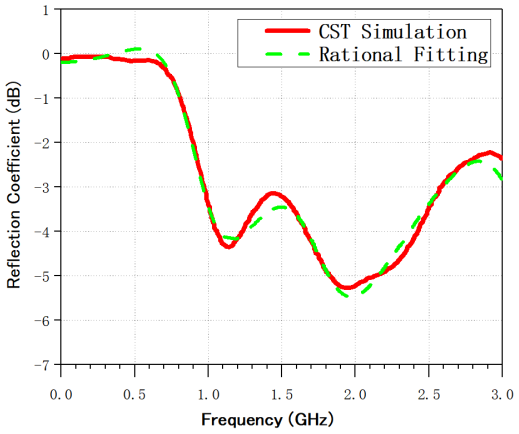

FIGURE 6.4: Reflection coefficient of fitting rational function and corresponding original simulation data.

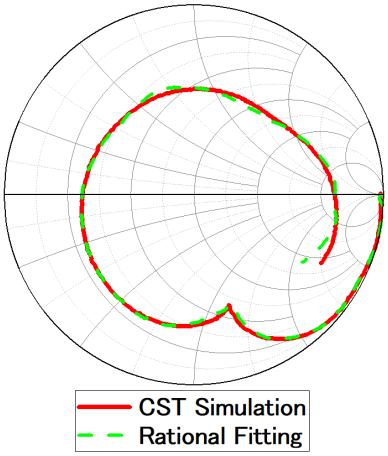

FIGURE 6.5: Smith chart of fitting rational function and corresponding original simulation data.

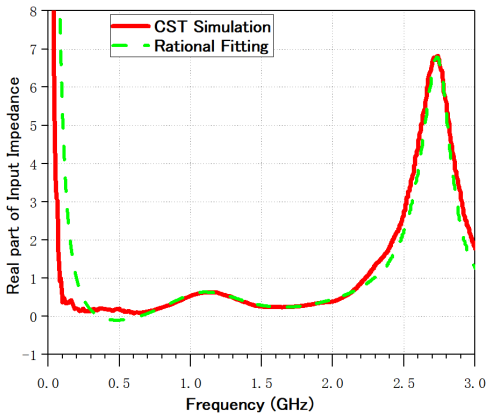

FIGURE 6.6: Real part of input impedance of fitting rational function and corresponding original data.

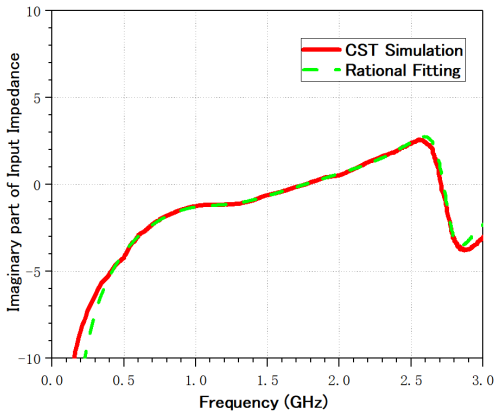

FIGURE 6.7: Imaginary part of input impedance of fitting rational function and corresponding original data.

After fitting and iteration process, the unknown coefficient vector $\boldsymbol{x}$ are listed in Table 6.1. The reflection coefficient and Smith chart of the fitting functions' curves are shown in Figure 6.4 and Figure 6.5, where the original data from the simulation are also plotted. Compared with Figure 6.2 and Figure 6.3, the fitting curves in Figure 6.4 and Figure 6.5 are optimized for both modulus and Smith chart of the antenna response. Especially, the curve of the Smith chart in Figure 6.5 fits so well in all the regions that the dispersion is eliminated when phase extraction is included.

Figure 6.6 and Figure 6.7 show the normalized input impedance of fitting rational function and original data from CAD simulation. In Figure 6.6 and Figure 6.7, the electronic components in the region $(1GHz - 2.5GHz)$ is fitting better than those in the region $(0 - 0.5GHz)$, because of the relative weighting factor $W_r = 1/|S_{11}^3|$. Thus, this rational function can be reliably used as a surrogate function in place of

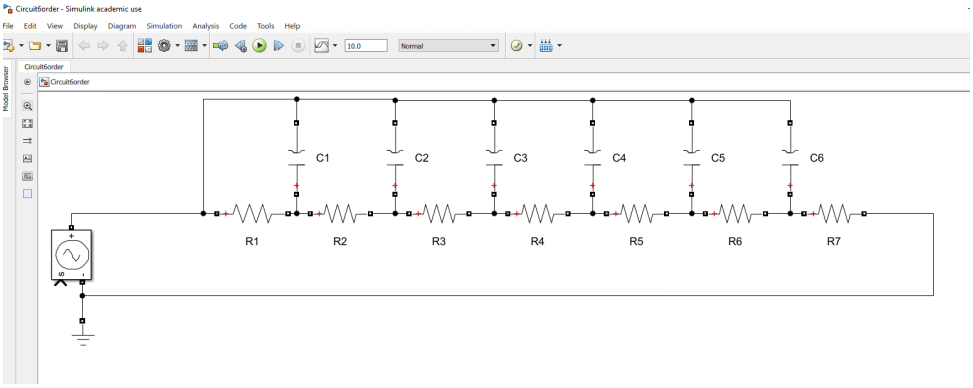

FIGURE 6.8: Equivalent circuit model of fitting rational function.

TABLE 6.2: Resistors and capacitors in the equivalent circuit

Notation	R_1	R_2	R_3	R_4	R_5	R_6	R_7
Value(Ω)	0.182	−0.0733	1.77	−1.09	5.83	−5.07	−2.58
Notation	C_1	C_2	C_3	C_4	C_5	C_6	
Value(F)	1.29	−1.24	0.0278	−0.1107	0.0031	−0.0232	

the original discrete data from the simulation.

To further verify the fitting rational function and to analyse the antenna property, an equivalent circuit composed of resistors and capacitors is constructed from this fitting rational function. Figure 6.8 shows the equivalent circuit topology, and the values of the electronic components are listed in Table 6.2. Since $m = n = 6$ in the rational function, the equivalent circuit in Figure 6.8 is composed of 7 resistors and 6 capacitors. There are several components with negative values, which do not exist alone in reality. They can be substituted by the group circuit of the positive electronic components and the controlled sources (CCCS, VCCS, VCVS), and the software Simulink allows to set negative components directly.

The normalized input impedance of the equivalent circuit using Simulink is shown in Figure 6.9 and Figure 6.10. The equivalent circuit curves are very close to the rational function curves in both the real and imaginary parts, demonstrating that the truncation error is limited here. Thus, this equivalent circuit can be reliably used as a surrogate circuit in place of the initial chassis antenna.

Therefore, the 13 extracted numbers in Table 6.1 could rebuild the antenna response, and the 13 components in Table 6.2 could be used as the surrogate circuit model. While the numbers of original discrete data from CST simulation are 1000, the compression ratio of parameter extraction is 1.3% (=13/1,000).

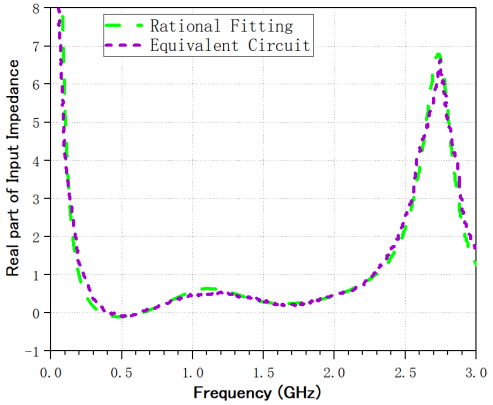

FIGURE 6.9: Real part of input impedance of the equivalent circuit in Simulink and fitting rational function.

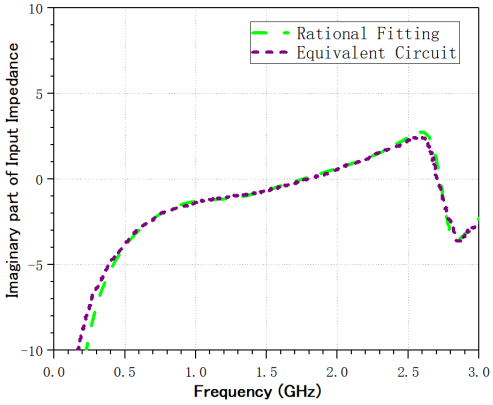

FIGURE 6.10: Imaginary part of input impedance of the equivalent circuit in Simulink and fitting rational function.

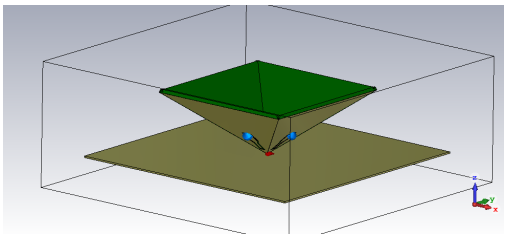

FIGURE 6.11: Geometry of the band-notched UWB pyramidal antenna in [89].

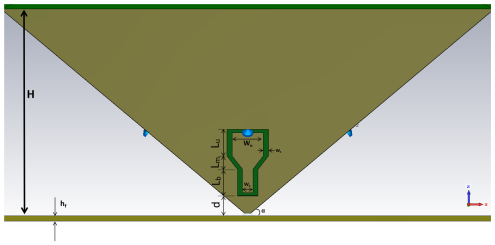

FIGURE 6.12: Dimension of the antenna with slot and capacitor in [89].

6.2 Application II

6.2.1 Antenna Design

A band-notched UWB pyramidal monopole antenna, its geometry shown in Figure 6.11, is taken as an application of the Rational Function with Weighted Iteration (RFWI) approach. The prototype of antenna design comes from [89], and this antenna is simulated using the transient solver in CST Microwave Studio® to achieve the desired completed antenna response, including its magnitude and phase information.

The band-notched UWB pyramidal monopole antenna is composed of four pieces

TABLE 6.3: The design specifications of antenna

Notation	Capacitor	H	h_f	α	d	W
Value	1pF	20.0mm	0.5mm	40°	3.0mm	80.0mm
Notation	W_u	W_b	W_s	L_u	L_m	L_b
Value	3.0mm	1.0mm	0.5mm	4.0mm	2.0mm	4.0mm

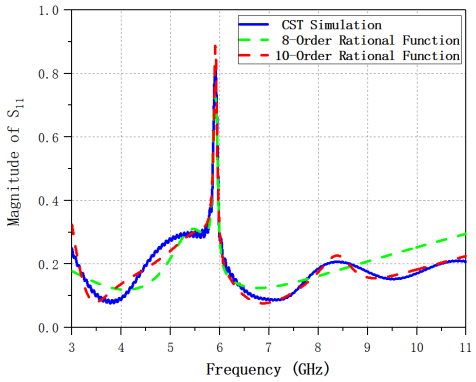

FIGURE 6.13: Magnitude of reflection coefficients of the band-notched UWB antenna.

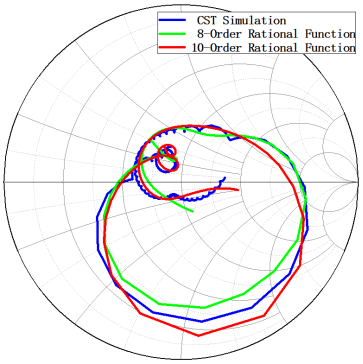

FIGURE 6.14: Smith chart of the band-notched UWB antenna.

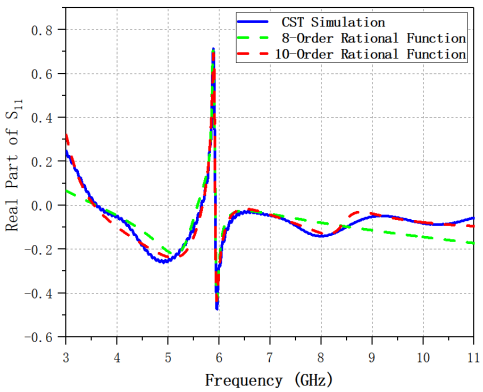

FIGURE 6.15: Real part of reflection coefficients of the band-notched UWB pyramidal antenna.

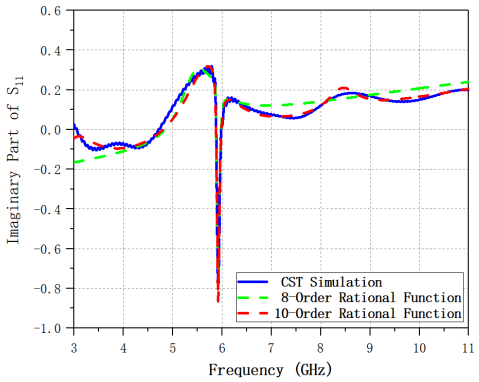

FIGURE 6.16: Imaginary part of reflection coefficients of the band-notched UWB pyramidal antenna.

of substrate TLY-3-0450-C5 (permittivity ε_r of 2.33, thickness of 1.143 mm). The pyramidal antenna is set on the centre of a copper ground plane ($80 \times 80 mm^2$). A slot is mounted with one 1pF capacitor in each face of the pyramidal monopole antenna. The dimension of the antenna with slots and capacitors is shown in Figure 6.12, and its corresponding design parameters are listed in Table 6.3.

To display accurately the system response in a complex number field, the modulus, real part, and imaginary part of reflection coefficient S_{11} are plotted in Figure 6.13 and Figure 6.15, and Figure 6.16, respectively. The Smith Chart representation is shown in Figure 6.14. It can be seen that this antenna works in the range of 3.00GHz-5.75 GHz and 6.00GHz-11.00 GHz with a notched-band of 5.75GHz-6.00 GHz at 10dB return loss.

TABLE 6.4: Unknown coefficient vector $\boldsymbol{x}$ of 10-order function

Notation	a_1	a_2	a_3	a_4
Value	3.51×10^{-1}	2.11×10^{2}	6.39×10^{3}	1.23×10^{6}
Notation	a_5	a_6	a_7	a_8
Value	2.44×10^{7}	2.31×10^{9}	3.39×10^{10}	1.60×10^{12}
Notation	a_9	a_{10}	a_{11}	
Value	1.90×10^{13}	2.80×10^{14}	4.27×10^{15}	
Notation	b_1	b_2	b_3	b_4
Value	-1.83×10^{1}	7.37×10^{3}	-1.43×10^{5}	2.06×10^{7}
Notation	b_5	b_6	b_7	b_8
Value	-3.59×10^{8}	2.73×10^{10}	-3.45×10^{11}	1.67×10^{13}
Notation	b_9	b_{10}		
Value	-1.01×10^{14}	3.53×10^{15}		

6.2.2 Fitting and Extraction

For fitting the rational function, the higher-order function leads to better approximation performance. Meanwhile, the tedious function with higher order would lead to longer computational runtime and result in more superfluous work when subsequently building an equivalent circuit based on this extracted rational function. Thus, after balancing between approximation precision and concise surrogate model, the order of the fitting rational function is set $m = n = 8$ and $m = n = 10$, respectively. The weighting factor $W_r = |S_{11}^2|$ could emphasize the notched band (5.75GHz-6.0 GHz) generated by slots and capacitors.

After weighted iterative calculation, the reflection coefficient S_{11} and Smith chart of the fitting rational function curves are shown in Figure 6.13, Figure 6.14, Figure 6.15, and Figure 6.16, respectively, to compare with those original data from CST simulation. To explicitly display the quantitative difference between fitting curves and original data from the simulation, Figure 6.13, Figure 6.15, and Figure 6.16 use a Cartesian coordinate system. The unknown coefficient vector $\boldsymbol{x}$ of 10-order ($m = n = 10$) fitting rational function is listed in Table 6.4.

Because the input variable and the output value of system response belong to the complex number field, the quality of fitting performance is related to both magnitude and phase. It can be seen that the fitting rational function is reliable and efficient as a surrogate function since the curves ($m = n = 10$) fit very well in these figures. In particular, the notched band (5.75GHz-6.0 GHz) could be precisely recognized from the operating UWB spectrum by the RFWI approach. And the fitting quality in the notched-band is much better than in other regions because of the weighting factor

setting $W_r = |S_{11}^2|$. The better fitting performance in Smith Chart demonstrates that this approach could minimize phase distortion, which is significant for practical utilization in the areas of microwave and RF.

Therefore, the fitting rational function is qualified to replace the initial band-notched UWB pyramidal monopole antenna as a surrogate function. The surrogate model only consists of 21 extracted real numbers in Table 6.4, so integrating the band-notched UWB antenna into a communication system would be convenient for both hardware and software in the future. More importantly, the RFWI approach is applied not only to the antenna of this case and the kind of band-notched UWB antenna but also to other kinds of antenna systems.

6.3 Summary

In this chapter, two traditional antennas, a chassis antenna and a band-notched UWB antenna, have been taken as applications to utilize the function fitting approach in Chapter 4 and the equivalent circuit method in Chapter 5. The extracted rational functions have high fidelity to rebuild the antenna responses, so it demonstrates that the principle in Chapter 3, the fitting approach in Chapter 4, and the equivalent circuit technique in Chapter 5 are feasible and effective. In the next chapter, a more challengeable reconfigurable antenna is chosen to obtain the surrogate model.

Chapter 7

Parameter Extraction from Reconfigurable Antenna

The Rational Fitting with Weighted Iteration (RFWI) approach is applied in traditional antennas in the last chapter. To verify effectiveness for broadband, sensitive recognition of very narrow band from UWB spectrum, and precision of the fitting result, a more challenging reconfigurable UWB antenna with tunable notched-band is taken to apply the RFWI approach and to obtain a data-driven surrogate model in this chapter.

7.1 Antenna Design

It is a reconfigurable ultra-wideband (UWB) pyramidal monopole antenna with a tunable notched band, which comes from [89]. To obtain the accurate and whole system response, including magnitude and phase information, the reconfigurable antenna is simulated using CST Microwave Studio®.

The structure of the reconfigurable UWB antenna is shown in Figure 7.1. The antenna, composed of four pieces of substrate TLY-3-0450-C5 (permittivity of 2.33, thickness of 1.143mm), is set on the centre of an $80 \times 80 mm^2$ copper ground plane. A slot is mounted with a varactor in each face of the UWB pyramidal antenna. The

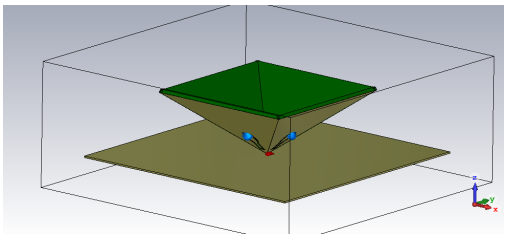

FIGURE 7.1: Geometry of the reconfigurable UWB pyramidal antenna with varactors in [89].

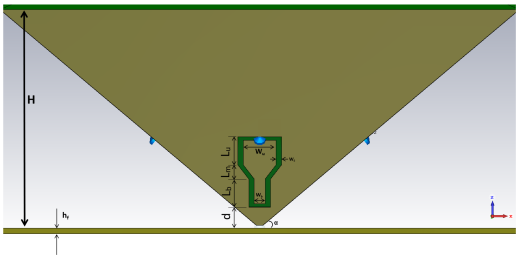

FIGURE 7.2: Dimension of the antenna with slot and varactor.

TABLE 7.1: Design specifications of the reconfigurable antenna

Notation	W	H	h_f	α	L_u	L_m
Value	80.00mm	20.00mm	0.5mm	40°	4.0mm	2.0mm
Notation	L_b	d	W_u	W_b	W_s	
Value	4.0mm	3.0mm	3.0mm	1.0mm	0.5mm	

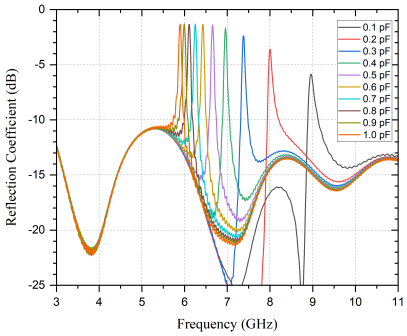

FIGURE 7.3: Reflection coefficient (dB) of the reconfigurable antenna with tunable varactor in CST simulation.

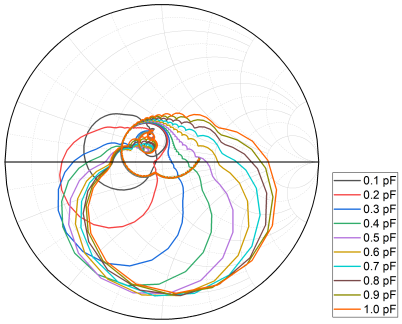

FIGURE 7.4: Smith chart of the reconfigurable antenna with tunable varactor in CST simulation.

dimension of one face with slot and varactor is shown in Figure 7.2 and the corresponding design specifications are listed in Table 7.1.

To depict the whole system response in a complex number field, the reflection coefficient in dB and Smith Chart of the reconfigurable antenna are shown in Figure 7.3 and Figure 7.4, respectively.

In Figure 7.3, the antenna works in the ultra-wideband (3GHz-11GHz), excluding the variable notched bands. The corresponding notched bands at -10 dB reflection coefficient, listed in Table 7.2, move towards lower frequency with a larger varactor value. That is the tunable notched-band reconfiguration of this antenna. The proportion of notched-bandwidth in ultra-wideband (3GHz-11GHz) is around 2.0% $\sim$ 3.4%.

7.2 Fitting and Extraction

After simulation, 1000 discrete complex data evenly distributed in the frequency range (3GHz-11GHz) are collected from CST simulation. Due to the very narrow notched-band (2.0% $\sim$ 3.4%) compared with ultra-wideband (3GHz-11GHz), there are fewer data in the notched-band and the magnitude of such data changes dramatically in Figure 7.3. When fitting, this situation must be taken into account; otherwise,

TABLE 7.2: Notched-band with different varactor

Varactor (pF)	Notched-Band (GHz)	Notched-BW (MHz)	Proportion in UWB
0.1	8.88~9.13	250	3.1%
0.2	7.94~8.21	270	3.4%
0.3	7.31~7.48	170	2.1%
0.4	6.89~7.05	160	2.0%
0.5	6.57~6.75	180	2.3%
0.6	6.33~6.51	180	2.3%
0.7	6.15~6.33	180	2.3%
0.8	6.00~6.19	190	2.4%
0.9	5.87~6.08	210	2.6%
1.0	5.73~5.99	260	3.3%

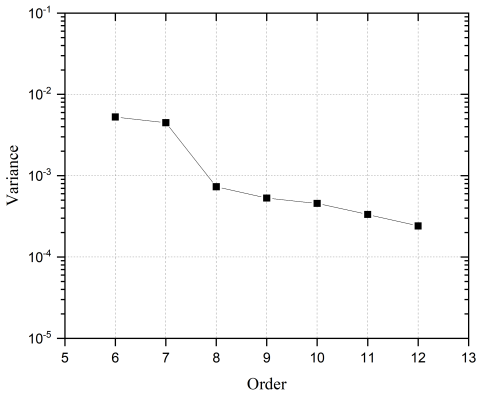

FIGURE 7.5: Variance σ^2 with different order.

the narrow notched band will not be recognized.

The tactic is to properly set the relative weighting factor $\boldsymbol{W}_r$ as

$$\boldsymbol{W}_r = diag\left\{\left|k_1\right| + \left|k_2\right| + c\right\}, (c = 1) \tag{7.1}$$

where k_1 and k_2 are forward slope and back slope of the magnitude of the reflection coefficient in Figure 7.3, respectively. The bias constant c is to prevent the relative weighting factor from becoming zero. For the first point, $\boldsymbol{W}_r = diag\left\{2\left|k_2\right| + c\right\}$. And for the last point, $\boldsymbol{W}_r = diag\left\{2\left|k_1\right| + c\right\}$.

The order of rational function affects the limitation of fitting precision. The variance σ^2 of 6-, 7-, 8-, 9-, 10-, 11-, and 12-order with fixed $0.5pF$ varactor using the same iteration times is listed in Table 7.3 and plotted in Figure 7.5. The corresponding magnitude of the S-parameter figure, Smith chart, real part and imaginary part

TABLE 7.3: Variance σ^2 with different order.

Order	6	7	8	9
Variance	5.28×10^{-3}	4.49×10^{-3}	7.31×10^{-4}	5.31×10^{-4}
Order	10	11	12	
Variance	4.56×10^{-4}	3.34×10^{-4}	2.41×10^{-4}	

of the S-parameter are shown in Figure 7.6, Figure 7.7, Figure 7.8, and Figure 7.9, respectively, where the order is set 6, 8, 10, and 12. In order to quantitatively display the fitting result, a Cartesian coordinate system is used in Figure 7.6, Figure 7.8, and Figure 7.9. Figure 7.5, Figure 7.6, Figure 7.7, Figure 7.8, and Figure 7.9 illustrate graphically that the higher-order function fits better, but the higher-order fitting spends more computational runtime. Trading off between precision and runtime, the following orders in this chapter are all set 12.

In Figure 7.6, Figure 7.7, Figure 7.8, and Figure 7.9, for all curves, the part in the notched-band range fits remarkably well, compared with other parts of the same curve. Clearly, it demonstrates the relative weighting factor $\boldsymbol{W}_r$ in Equation (7.1) is effective to recognize the narrow notched-band from the UWB spectrum.

Subsequently, the extracted parameters of fitting rational function with variable varactor from $0.1pF$ to $1.0pF$ are listed in Table C.1. The variance σ^2 between rational function and simulation are listed in Table C.2. The S-parameter figures and Smith chart of rational function fitting with $0.1pF$, $0.2pF$, $0.3pF$, $0.4pF$, $0.5pF$, $0.7pF$ and $1.0pF$ and their corresponding original simulation are shown in Figure 7.10, Figure 7.11, Figure 7.12, and Figure 7.13. It can be seen that the variance σ^2 in Table C.2 are very tiny. In Figure 7.10, Figure 7.11, Figure 7.12, and Figure 7.13, all

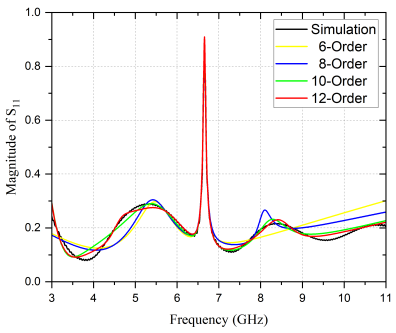

FIGURE 7.6: Magnitude of S-parameter with fixed 0.5pF varactor in the Cartesian coordinate, when rational function is 6-, 8-, 10-, 12-Order, respectively.

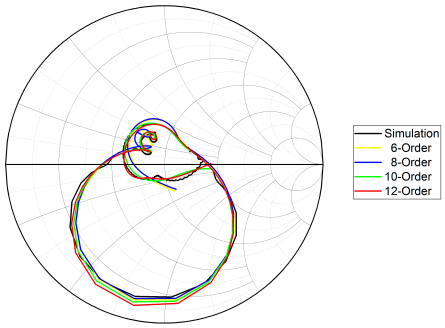

FIGURE 7.7: Smith chart of the reconfigurable antenna with fixed 0.5pF varactor, when rational function is 6-, 8-, 10-, 12-Order, respectively.

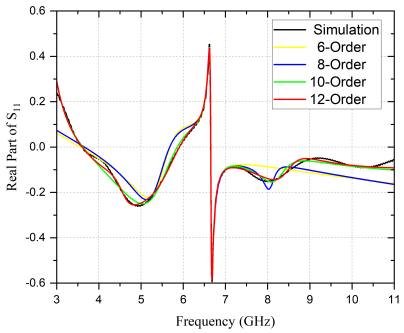

FIGURE 7.8: Real part of S-parameter with fixed 0.5pF varactor in the Cartesian coordinate, when rational function is 6-, 8-, 10-, 12-Order, respectively.

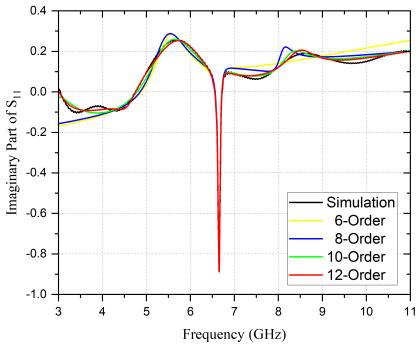

FIGURE 7.9: Imaginary part of S-parameter with fixed 0.5pF varactor in the Cartesian coordinate, when rational function is 6-, 8-, 10-, 12-Order, respectively.

of the rational functions fit very well with the simulation data, including magnitude, real part, and imaginary part of S-parameter, and Smith chart.

7.3 Interpolation

Although all rational functions fit well with 19 groups of antenna response and corresponding parameters are extracted, the tunable varactor value of this reconfigurable antenna is continuously variable and infinite. It is infeasible to simulate and fit all possible responses. Thus, a proper method is required to construct a surrogate model.

Each of extracted parameters with different varactor values from $0.1pF$ to $1.0pF$ of Table C.1 is plotted in Figure 7.14, where all parameters change smoothly. In accordance with the foundation of Space Mapping [72], the system's input variables and output response are continuous multi-dimensional space. Therefore, a linear interpolation method based on 19 groups of extracted parameters in Table C.1, is able to approximate this reconfigurable antenna's response with an arbitrary varactor value.

By linear interpolation, the parameters of a rational function with some varactor value are figured out and listed in Table C.4. The variance σ^2 between interpolation and simulation are listed in Table C.3, which are plotted in Figure 7.15. The S-parameter figures and Smith chart with $0.12pF$, $0.18pF$, $0.28pF$, $0.38pF$, $0.48pF$, $0.68pF$, $0.98pF$ varactor and their corresponding original simulation as comparison are depicted in Figure 7.16, Figure 7.17, Figure 7.18, and Figure 7.19.

The variance σ^2 in Table C.3 is not as accurate as those in Table C.2, which is clearly illustrated in Figure 7.15. However, the interpolation result is still acceptable to be a surrogate model. If necessary, increasing groups of simulation and fitting

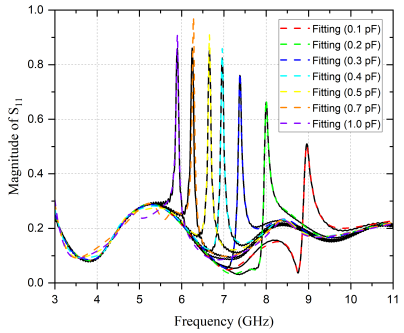

FIGURE 7.10: Magnitude of S-parameter with 12-order rational function, when tunable varactor is 0.1pF, 0.2pF, 0.3pF, 0.4pF, 0.5pF, 0.7pF, and 1.0pF, respectively. The corresponding original curves in CST simulation are black solid lines as a contrast.

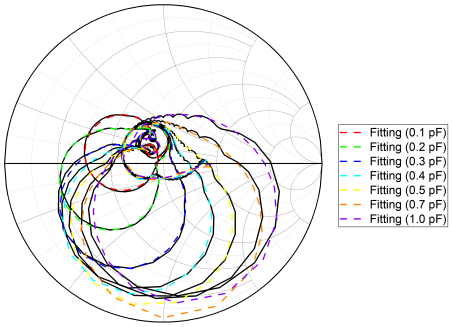

FIGURE 7.11: Smith chart of S-parameter with 12-order rational function, when tunable varactor is 0.1pF, 0.2pF, 0.3pF, 0.4pF, 0.5pF, 0.7pF, and 1.0pF, respectively. The corresponding original curves in CST simulation are black solid lines as a contrast.

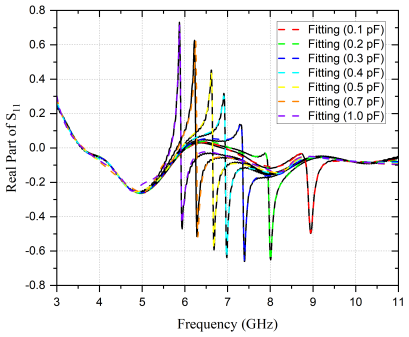

FIGURE 7.12: Real part of S-parameter with 12-order rational function, when tunable varactor is 0.1pF, 0.2pF, 0.3pF, 0.4pF, 0.5pF, 0.7pF, and 1.0pF, respectively. The corresponding original curves in CST simulation are black solid lines as a contrast.

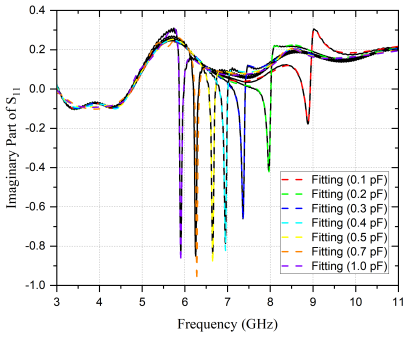

FIGURE 7.13: Imaginary part of S-parameter with 12-order rational function, when tunable varactor is 0.1pF, 0.2pF, 0.3pF, 0.4pF, 0.5pF, 0.7pF, and 1.0pF, respectively. The corresponding original curves in CST simulation are black solid lines as a contrast..

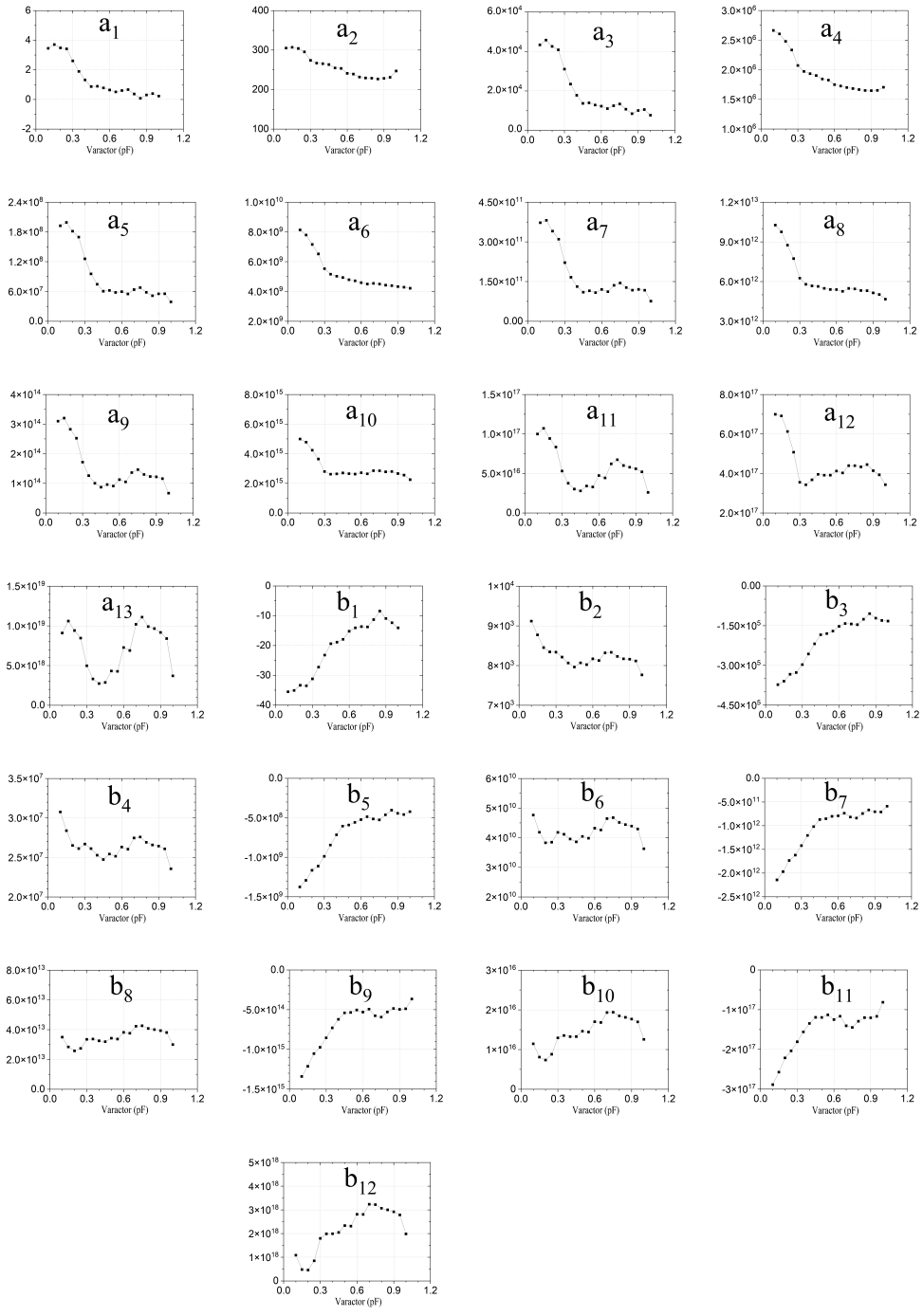

FIGURE 7.14: Each dimension of unknown coefficient vector x with different varactor from 0.1pF to 1.0pF obtained from the fitting rational function.

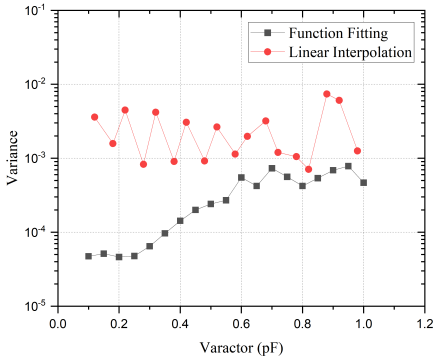

FIGURE 7.15: Variance σ^2 with different varactor.

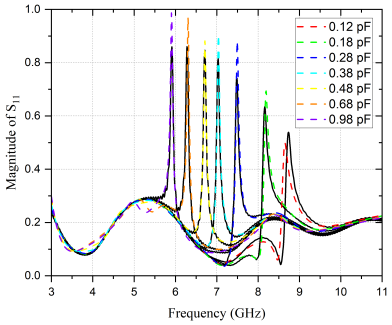

FIGURE 7.16: Magitude of S-parameter with 12-order function, when varactor is 0.12pF, 0.18pF, 0.28pF, 0.38pF, 0.48pF, 0.68pF, and 0.98pF, respectively. The corresponding curves in simulation are black solid lines as a contrast.

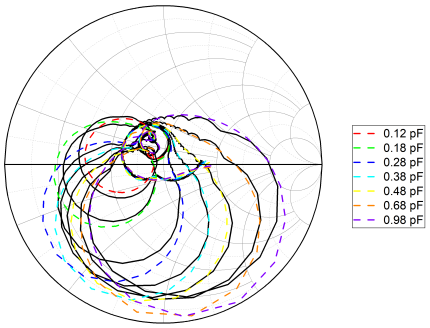

FIGURE 7.17: Smith chart of S-parameter with 12-order function, when varactor is 0.12pF, 0.18pF, 0.28pF, 0.38pF, 0.48pF, 0.68pF, and 0.98pF, respectively. The corresponding curves in simulation are black solid lines as a contrast.

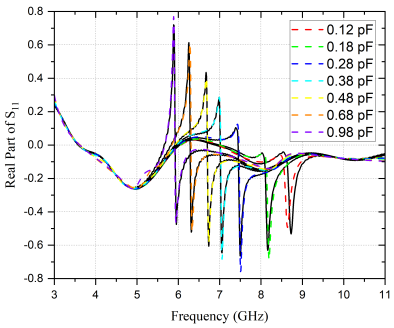

FIGURE 7.18: Real part of S-parameter with 12-order function, when varactor is 0.12pF, 0.18pF, 0.28pF, 0.38pF, 0.48pF, 0.68pF, and 0.98pF, respectively. The corresponding curves in simulation are black solid lines as a contrast.

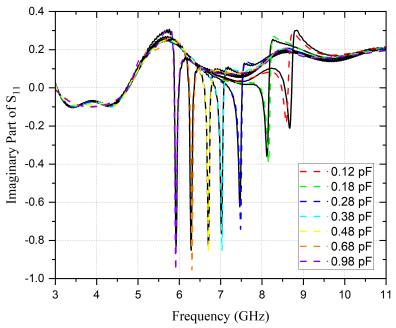

FIGURE 7.19: Imaginary part of S-parameter with 12-order function, when varactor is 0.12pF, 0.18pF, 0.28pF, 0.38pF, 0.48pF, 0.68pF, and 0.98pF, respectively. The corresponding curves in simulation are black solid lines as a contrast.

data in Table C.1 can actually improve interpolation precision. In Figure 7.16, Figure 7.17, Figure 7.18, and Figure 7.19, the curves of interpolation are very close to simulation curves, including both magnitude and phase. It indicates that the linear interpolation method based on pre-existing data in Table C.1 is feasible to quickly obtain a completed system response with an arbitrary varactor.

So far, a proper surrogate model has been obtained to substitute the reconfigurable ultra-wideband (UWB) pyramidal monopole antenna with a tunable notched band.

7.4 Discussion

Through this example, the Rational Fitting with Weighted Iteration (RFWI) approach has many advantages and potential applications.

Firstly, on account of elastic order of rational function and adaptable weighting factor ($\boldsymbol{W}_r$) in the iterative process, the RFWI approach has the flexibility to be widely utilized for the specific requirements, such as the example shown in this chapter, the precise recognition of the very narrow notched-band from the UWB spectrum.

Secondly, it is effective to find a feasible surrogate model through the RFWI approach. In this chapter, the exported data from the CST simulation are 19 groups of antenna responses, and each group contains 1000 complex numbers ($38,000 = 2 \times 1,000 \times 19$). After RFWI fitting, 25 real numbers composing one rational function are extracted from each group of responses ($475 = 25 \times 19$). Thus, the compression ratio of parameter extraction is 1.25% (=475/38,000). These 475 real numbers with the linear interpolation method can construct the arbitrary responses of this reconfigurable antenna with tiny variance σ^2 at the level of 10^{-3}. In other words, the combination of 475 real numbers in Table C.1 and the interpolation method is an excellent surrogate model of the reconfigurable UWB antenna with tunable notched-band.

The benefit of the surrogate model extracted through RFWI is meaningful to integrating the complicated reconfigurable antenna into a communication system for both software and hardware aspects. In the software aspect, the surrogate model can combine faster with signal processing algorithm to uncover the potential ability of reconfigurable antenna, since the surrogate model has less data, only 475 real numbers. In the hardware aspect, it is convenient to be implemented into a chip since the rational function is composed of simple arithmetical operations, only including addition, multiplication (and power), and division.

Besides the CAD simulation shown in this chapter, the VNA measurement can also be the input data of the RFWI approach. Thus, this approach could also obtain the surrogate model of a practical reconfigurable antenna.

Additionally, this approach is not subject to electrical loading reconfiguration. In fact, besides electrical loading, this approach is able to be reliably applied to all reconfigurable antennas based on different mechanisms, such as mechanical changes and material changes.

Last but not least, RFWI is convenient to combine with Artificial Intelligence (AI) algorithms. From an AI perspective, the RFWI approach is regarded as a process of feature extraction. The feature is extracted very well through RFWI because few output data contain completed information of the system response. And the fitting process converts the complicated electromagnetic structure to an analytical function, which could combine with an AI algorithm to realize the automated design in microwave and RF areas in the future.

7.5 Summary

In this chapter, a more challenging reconfigurable UWB antenna with tunable notched-band has been taken as an application using the Rational Fitting with Weight Iteration (RFWI) approach. It demonstrates that the RFWI approach is a reliable and efficient approach with high fidelity to extract parameters and obtain a surrogate model from the reconfigurable antenna. However, as a data-driven approach, it restricts the width of the reconfigurable range. To widen the reconfigurable range with the same numbers of extracted parameters, a physics-based surrogate modelling approach is developed in Chapter 8.

Chapter 8

A Physics-Based Surrogate Model of Reconfigurable Antenna

In the last chapter, a data-driven surrogate modelling approach is applied in a reconfigurable UWB antenna. To increase the efficiency of feature extraction, a new surrogate modelling approach is needed. There is no doubt that a physics-based generic surrogate model is attractive but very difficult to find. Luckily, for a frequency reconfigurable antenna with electronic loadings, the model based on the equivalent network analysis method is available as the physics-based surrogate model. It is the reason that the network analysis is based on physical principles, such as Kirchhoff's Current/Voltage Law and Maxwell's Equations. Additionally, equivalent circuit and network analysis are the standard methods to simplify the complicated electromagnetic structure [90] and design antenna [91]. Therefore, the surrogate model with equivalent network analysis has fewer extracted features.

In this chapter, a physics-based surrogate model combining the RFWI approach and equivalent network analysis is developed for a frequency reconfigurable antenna with electronic loadings.

8.1 Physics-Based Surrogate Modelling Approach

The surrogate modelling flow is shown in Figure 8.1. The starting point of this process in Figure 8.1 is a detailed design structure of the reconfigurable antenna, including geometry sizes and material properties, so that the antenna can be modelled on the computer or be fabricated in reality. The first step in this flow is to remove all the dynamic electronic loadings from the original reconfigurable antenna. The remaining part of the reconfigurable antenna without dynamic loadings is regarded as a multi-port network. Let's suppose the reconfigurable antenna has n dynamic electronic loadings. The multi-port network without dynamic loadings has $n+1$ ports since the additional port is for antenna feeding.

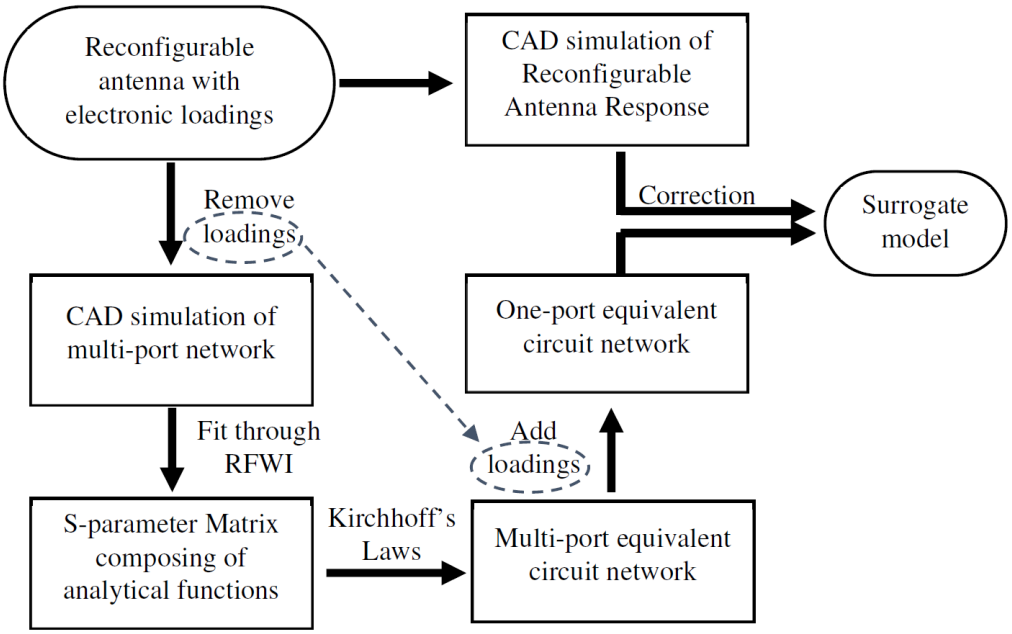

FIGURE 8.1: Flow chart of the physics-based surrogate modeling process.

Because the multi-port network does not contain any dynamic components, its responses in the frequency domain depend on only frequency. The responses can be output through CAD simulation or VNA measurement, and the obtained responses are discrete numerical data. The scattering parameter of the multi-port network is an $(n+1)\times(n+1)$ matrix. Each element of the matrix only relies on the variable frequency, and they can be approximated through Rational Fitting with Weighted Iteration (RFWI) as the type of analytical rational function,

$$\check{S}_{ij}(s) \approx S_{ij}(s;\boldsymbol{x}) = \frac{s^r + b_1 s^{r-1} + \cdots + b_i s^{r-i} + \cdots + b_r}{a_1 s^t + a_2 s^{t-1} + \cdots + a_j s^{t+1-j} + \cdots + a_{t+1}}, \quad (i,j = 1,2,3,\cdots,n,n+1) \tag{8.1}$$

where $\check{S}_{ij}(s)$ is the observable scattering parameters, $S_{ij}(s;\boldsymbol{x})$ is the approximated analytical rational function, and the unknown coefficient vector $\boldsymbol{x}$ is the extracted feature of the analytical function. The scattering parameter matrix is a set of analytical rational functions, and such an analytical matrix could allow to be operated with mathematical calculation and transformation.

The equivalent circuit distribution of the multi-port network could be generated from the scattering matrix based on Kirchhoff's Current/Voltage Law. And then, the assembly of the multi-port equivalent network and the previously removed dynamic electronic loadings becomes a new one-port network, which is the equivalent network of the original reconfigurable antenna. Therefore, the reflection coefficient and the equivalent impedance of the original reconfigurable antenna can be determined.

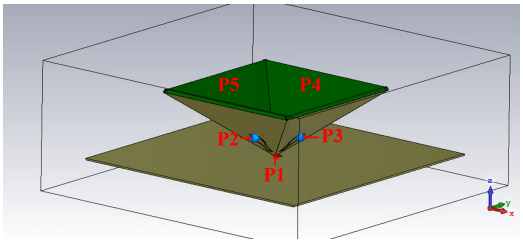

FIGURE 8.2: Geometry of the reconfigurable antenna.

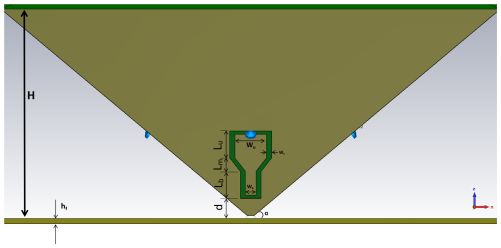

FIGURE 8.3: Dimension of one face with slot and varactor.

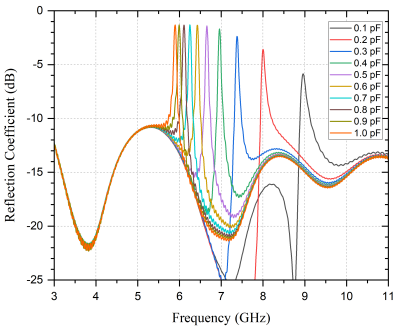

FIGURE 8.4: Magnitude of reflection coefficient of the reconfigurable antenna with tunable varactor from CST simulation.

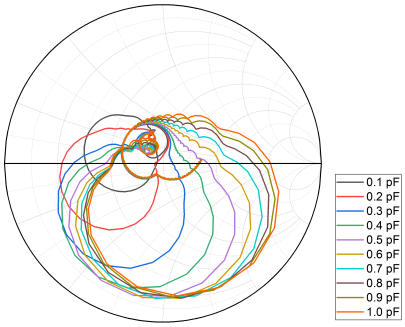

FIGURE 8.5: Smith chart of the reconfigurable antenna with tunable varactor from CST simulation.

In fact, due to the inner complicated electromagnetic field of the multi-port network, the validation of the equivalent network is limited in some specified conditions. Connecting the dynamic electronic loadings actually changes the inner electromagnetic field and current distribution of the multi-port network, so the obtained equivalent network needs to be modified. Thus, it is indispensable to make some corrections based on the obtained equivalent network to optimize the physics-based surrogate model of the original reconfigurable antenna.

8.2 Antenna Design

The application is a frequency reconfigurable ultra-wideband pyramidal monopole antenna with tunable varactors. The antenna geometry and design are shown in Figure 8.2 and Figure 8.3, and the design specifications are followed in [92]. This reconfigurable antenna has four tunable varactors mounted on these ports (P2, P3, P4, P5 in Figure 8.2), controlled by the same bias circuit. Thus, it only has one independent input reconfigurable variable.

The antenna responses with variable varactor are simulated using the transient solver in CST Microwave Studio®. Its reflection coefficient in dB and on a Smith

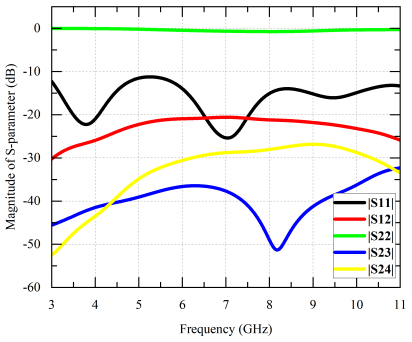

FIGURE 8.6: Magnitude of S parameters of the multi-port network from CST simulation.

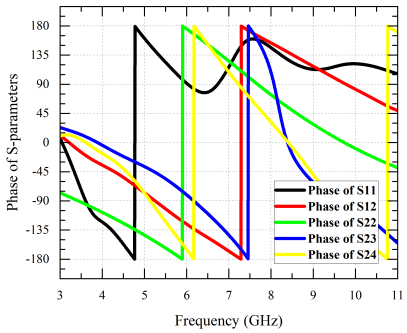

FIGURE 8.7: Phase of S parameters of the multi-port network from CST simulation.

chart is plotted in Figure 8.4 and Figure 8.5. It can be seen that the reconfigurable antenna works in the ultra-wideband (3GHz-11GHz), excluding the notched band, which is tuned by the variable varactor. When the variable varactor is larger, the notched band will move toward a lower frequency.

8.3 Parameter Extraction and Network Analysis

This reconfigurable antenna with four varactors is a suitable application for network analysis since the network of the reconfigurable antenna without varactors is 5-port. The 5-port network is simulated using the transient solver in CST Microwave Studio®.

Its scattering parameter matrix is a 5×5 matrix. The geometry of this reconfigurable antenna has several symmetrical properties, which could reduce the complexity of the matrix and equivalent network [93], [94]. Firstly, for these ports connecting electronic loadings (P2, P3, P4, P5), their reflection parameters are equal: $S_{22} = S_{33} = S_{44} = S_{55}$. Secondly, for the feeding port (P1), four loading ports (P2, P3, P4, P5) are the same: $S_{12} = S_{13} = S_{14} = S_{15}$. Thirdly, for the loading ports (P2, P3, P4, P5), their adjacent loading ports are the same. For example, P3 and P5 are the adjacent loading ports of P2, so $S_{23} = S_{25}$. Fourthly, for the non-adjacent loading ports, their relationships are equal, so $S_{24} = S_{35}$. Fifthly, the 5-port network is a reciprocal network, so $S_{ij} = S_{ji}(i, j = 1, 2, 3, 4, 5)$. To sum up, there are only 5

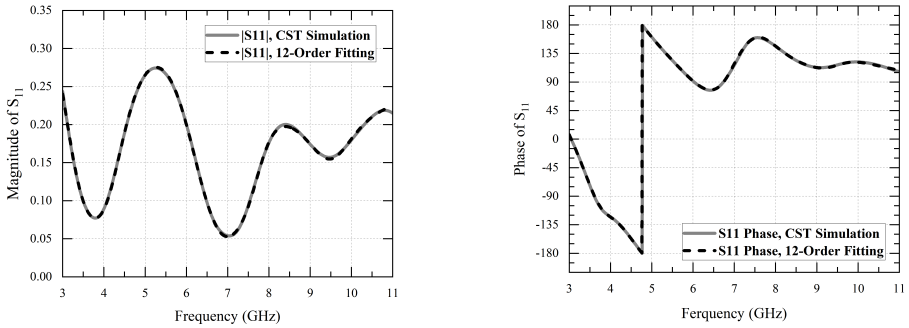

FIGURE 8.8: Rational function fitting of S11.

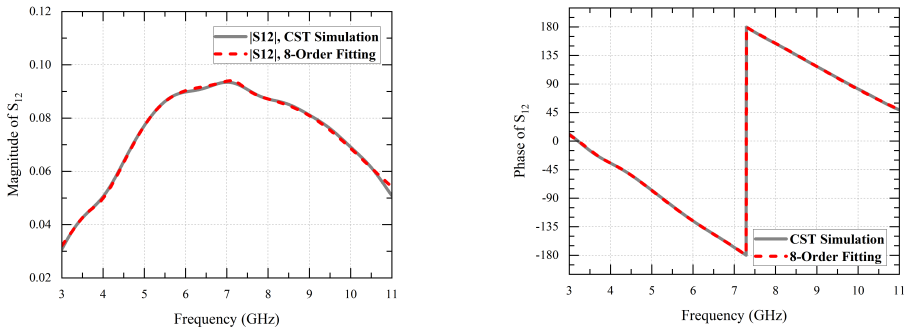

FIGURE 8.9: Rational function fitting of S12.

different independent elements $(S_{11}, S_{12}, S_{22}, S_{23}, S_{24})$ in this 5×5 matrix,

$$\begin{cases} S_{11} \\ S_{12} = S_{13} = S_{14} = S_{15} = S_{21} = S_{31} = S_{41} = S_{51} \\ S_{22} = S_{33} = S_{44} = S_{55} \\ S_{23} = S_{25} = S_{34} = S_{45} = S_{32} = S_{52} = S_{43} = S_{54} \\ S_{24} = S_{35} = S_{42} = S_{53} \end{cases} \tag{8.2}$$

They are discrete numerical data sets in a complex field, including the magnitude shown in Figure 8.6 and the phase shown in Figure 8.7. In order to do the subsequent calculation and transformation, fitting analytical functions with these discrete numerical data is necessary. The RFWI approach is used for analytical rational function extraction. The fitting performances contain every independent element of the matrix, S_{11} shown in Figure 8.8, S_{12} shown in Figure 8.9, S_{22} shown in Figure 8.10, S_{23} shown in Figure 8.11, S_{24} shown in Figure 8.12. The orders of the fitting analytical rational functions are 12-, 8-, 10-, 8-, and 10-order, respectively, so the extracted numbers of these rational functions are 25, 17, 21, 17, and 21, respectively.

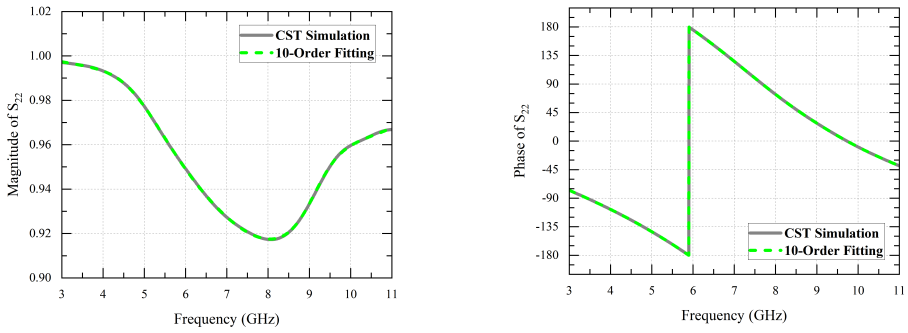

FIGURE 8.10: Rational function fitting of S22.

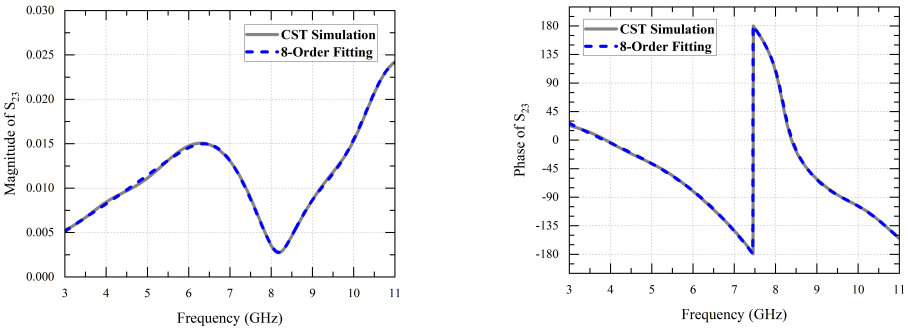

FIGURE 8.11: Rational function fitting of S23.

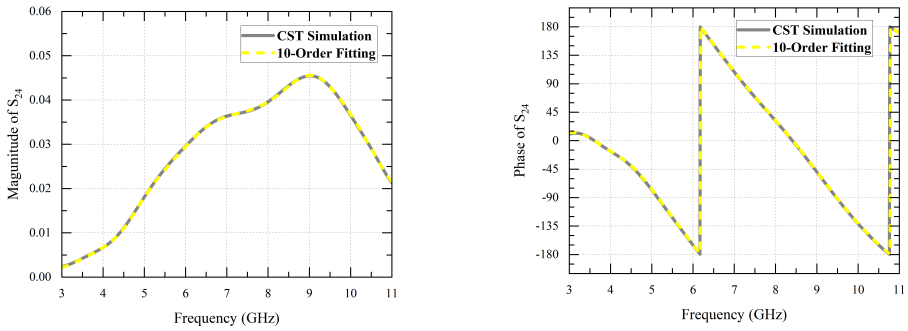

FIGURE 8.12: Rational function fitting of S24.

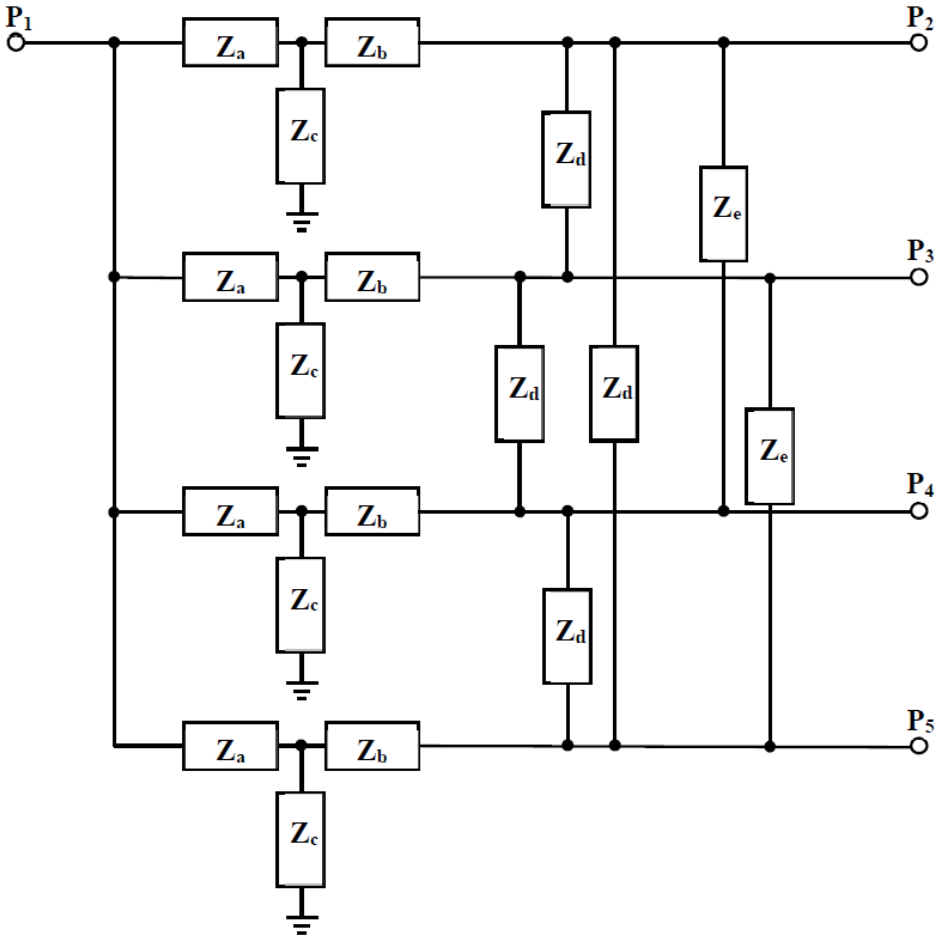

FIGURE 8.13: Equivalent network topology.

The impedance matrix, Z matrix, can be found directly from S parameter matrix,

$$[Z] = ([U] + [S])([U] - [S])^{-1} \tag{8.3}$$

The topology of the 5-port equivalent network is plotted in Figure 8.13, where five independent unknown components $(Z_a, Z_b, Z_c, Z_d, Z_e)$ can be found from the Z matrix. Because of the closure of rational functions in mathematics, the Z matrix elements and the network components $(Z_a, Z_b, Z_c, Z_d, Z_e)$ are also the rational functions. The rational functions of the network components $(Z_a, Z_b, Z_c, Z_d, Z_e)$ can be conveniently converted to the equivalent lumped circuit [85].

Then, the 5-port equivalent network connecting four varactors becomes a new 1-port equivalent network. All performances of the 1-port network can be determined, including equivalent impedance and reflection coefficient. The reflection coefficient of the 1-port network within the variable varactor can describe the dynamic reconfiguration of the antenna.

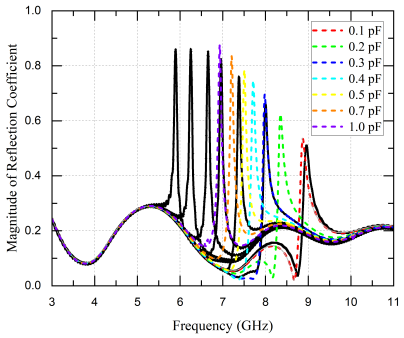

FIGURE 8.14: Magnitude of reflection coefficient of equivalent network with vriable varactor and the corresponding data from CST simulation.

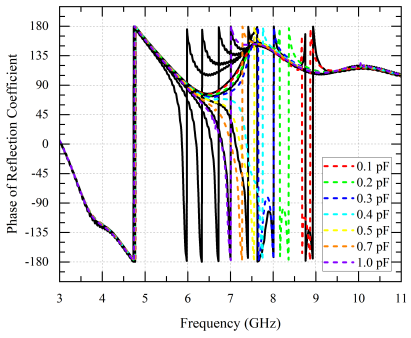

FIGURE 8.15: Phase of reflection coefficient of equivalent network with vriable varactor and the corresponding data from CST simulation.

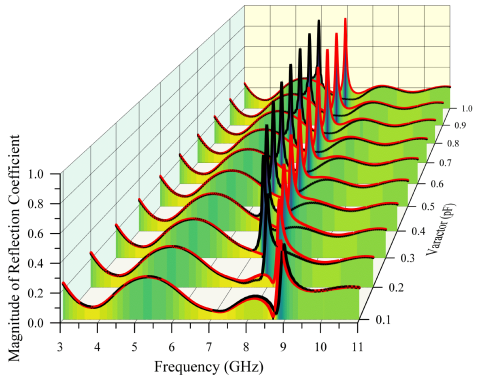

FIGURE 8.16: 3-D magnitude of reflection coefficient of equivalent network with vriable varactor and the corresponding data from CST simulation.

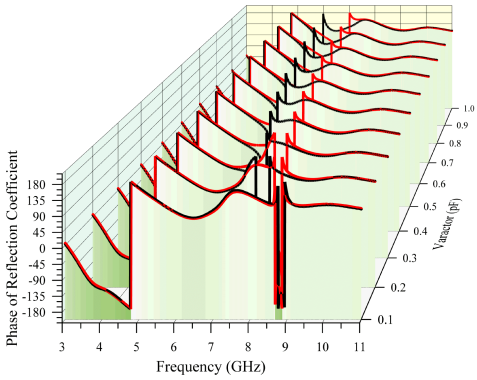

FIGURE 8.17: 3-D phase of reflection coefficient of equivalent network with variable varactor and the corresponding data from CST simulation.

8.4 Correction and Verification

The reflection coefficients of the 1-port equivalent network with dynamic reconfiguration contain the magnitude shown in Figure 8.14 and the phase shown in Figure 8.15, where the corresponding data from CST simulation are also plotted. In order to clearly display the responses performance and the variation trend with the variable varactor, 3-D figures with an additional axis representing the variable varactor plot the reflection coefficient, including the 3-D magnitude shown in Figure 8.16 and the 3-D phase shown in Figure 8.17.

In Figures 8.14, Figure 8.15, Figure 8.16, Figure 8.17, it can be seen that the remarkable antenna characteristics of the UWB spectrum and narrow notched band are displayed. The frequency of the notch band gets lower as the varactor capacitance increases, as expected from the simulation. However, the frequencies of notched bands with the same varactor could not match quantitatively between equivalent network

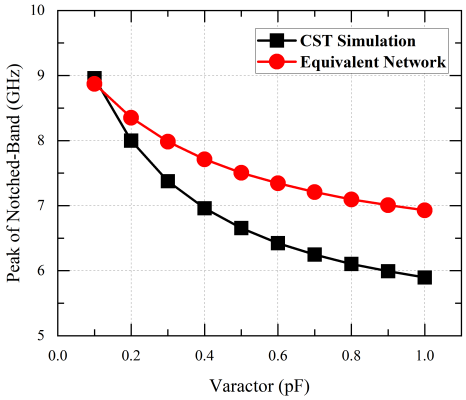

FIGURE 8.18: Notched-band peak frequency of equivalent network response without correction and the corresponding data from CST simulation.

TABLE 8.1: Notched-band peak frequency of responses without correction

Varactor(pF)	**Peak Frequency from CST Simulation (GHz)**	**Peak Frequency from Equivalent Network (GHz)**
0.1	8.98	8.87
0.2	8.00	8.35
0.3	7.38	7.98
0.4	6.96	7.71
0.5	6.66	7.50
0.6	6.42	7.34
0.7	6.25	7.21
0.8	6.10	7.10
0.9	5.99	7.10
1.0	5.90	6.93

and CST simulation. The peak frequency of the notched bands with the variable varactor is shown in Figure 8.18 and the corresponding data are listed in Table 8.1. Thus, the proper correction is needed.

For the narrow dynamic range, a linear function is used as the correction,

$$V_c = aV + b, \tag{8.4}$$

where V is the initial input variable varactor, and V_c is the input variable varactor after linear correction. The correctional parameters (a, b) are set as $a = 0.34$ and $b = 0.09$. With the linear correction, the peak frequency of notched bands with variable varactor is shown in Figure 8.19 and the corresponding data are listed in Table 8.2.

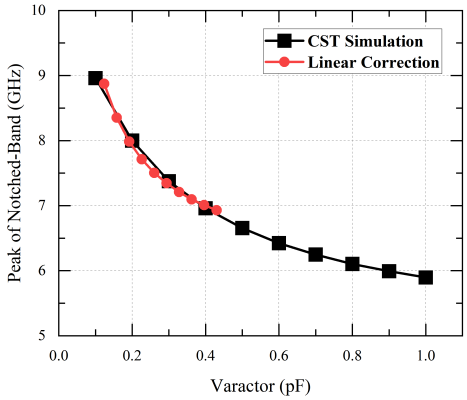

FIGURE 8.19: Notched-band peak frequency of equivalent network response with linear correction and the corresponding data from CST simulation.

TABLE 8.2: Notched-band peak frequency of responses with linear correction

V(pF)	**V_c(pF)**	**Peak Frequency with Linear Correction (GHz)**
0.1	0.124	8.87
0.2	0.158	8.35
0.3	0.192	7.98
0.4	0.226	7.71
0.5	0.260	7.50
0.6	0.294	7.34
0.7	0.328	7.21
0.8	0.362	7.10
0.9	0.396	7.10
1.0	0.430	6.93

For the broad dynamic range, the simple linear function is inaccurate, and a logarithmic function is used as the correction function,

$$V_c = a \cdot log_{10}(V + c) + b. \tag{8.5}$$

The correctional parameters (a, b, c) are set as $a = 0.5$, $b = 0.35$, and $c = 0.23$. With the logarithmic correction, the peak frequency of notched bands with variable varactor is shown in Figure 8.20 and the corresponding data are listed in Table 8.3.

The above analysis completes the physics-based surrogate model with a broad dynamic range (0.1pF-1pF). In order to verify the validity of the continuously variable varactor, the correctional model responses and the corresponding CST simulation are illustrated in Figure 8.21 and Figure 8.22. For the magnitude in Figure 8.21 and the

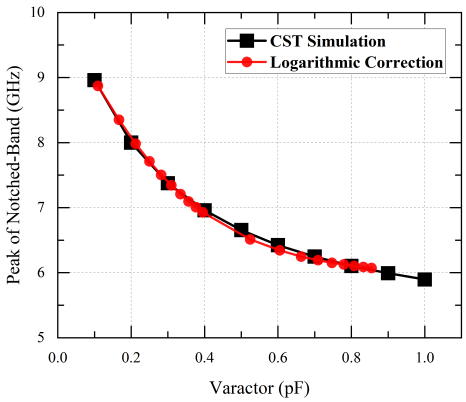

FIGURE 8.20: Notched-band peak frequency of equivalent network response with logarithmic correction and the corresponding data from CST simulation.

TABLE 8.3: Notched-band peak frequency of responses with logarithmic correction

V(pF)	V_c**(pF)**	**Peak Frequency with Linear Correction (GHz)**
0.1	0.109	8.87
0.2	0.167	8.35
0.3	0.212	7.98
0.4	0.250	7.71
0.5	0.281	7.50
0.6	0.310	7.34
0.7	0.334	7.21
0.8	0.356	7.10
0.9	0.377	7.10
1.0	0.395	6.93
2.0	0.524	6.51
3.0	0.605	6.34
4.0	0.663	6.25
5.0	0.709	6.19
6.0	0.747	6.15
7.0	0.780	6.13
8.0	0.808	6.10
9.0	0.833	6.09
10.0	0.855	6.07

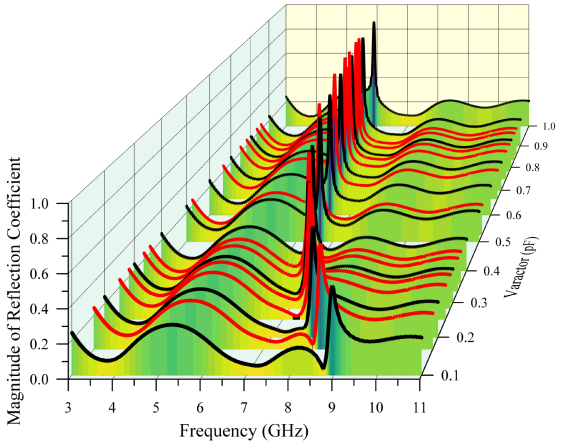

FIGURE 8.21: After logarithmic correction, 3-D magnitude of reflection coefficient of equivalent network with vriable varactor and the corresponding CST simulation.

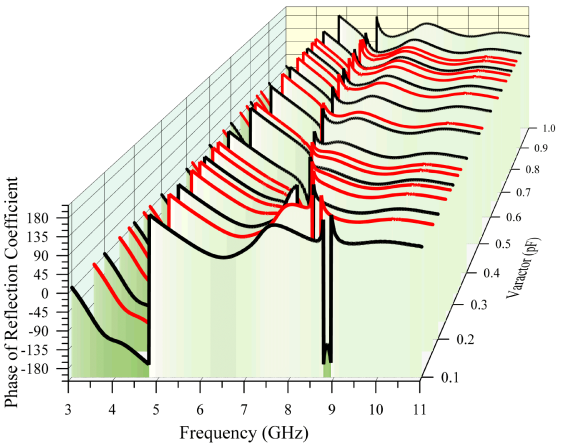

FIGURE 8.22: After logarithmic correction, 3-D phase of reflection coefficient of equivalent network with vriable varactor and the corresponding CST simulation.

phase in Figure 8.22, the surfaces of response data representing both the surrogate model and the CST simulation change smoothly, especially the better continuity of the remarkable notched bands. It demonstrates that the final surrogate model is well qualified to represent the original reconfigurable antenna.

8.5 Discussion

The proposed physics-based surrogate modelling technique is a comprehensive approach that combines the RFWI approach and network analysis. They aim to obtain a surrogate model with fewer extracted features, higher fidelity, and a broader dynamic range.

In this chapter, the surrogate model is presented for the continuous frequency reconfigurable antenna with tuning electronic components. As another common kind of reconfigurable antenna, a switched frequency reconfigurable antenna with several operating states can be designed using PIN diodes or other switch components. Its surrogate model is a group of several traditional antennas' models, or the surrogate model in this chapter with several discrete input variables. That means the surrogate model could be used for switched frequency reconfigurable antenna.

As the initial input data of this surrogate model, the discrete response data from CAD simulation in this chapter could be substituted by those from practical VNA, and the subsequent steps keep the same. In other words, this surrogate modelling technique is also applied for a practical reconfigurable antenna.

It is significant and necessary to use the RFWI approach to fit the discrete responses data to extract the analytical rational functions. Those discrete data may have different interval frequencies, even from different sources. For instance, some of the data are from different CAD software simulations, while some of the data are from VNA measurements. Thus, converting the discrete data to the analytical rational functions is a necessity and a prerequisite to making the subsequent processes, such as the transformation between the S matrix and the Z matrix, the design of the equivalent network, the calculation of the reflection coefficient, and the correction of the input variable.

Although the example antenna in this chapter with four varactors is regarded as only one independent input variable, the surrogate model based on the equivalent network can be applied for a more complicated reconfigurable antenna with multiple electronic components, such as the reconfigurable antenna in [95].

Because this surrogate model could be expressed by the analytical rational functions, it can describe the continuously dynamic reconfiguration of the antenna with arbitrary input variables.

The number of extracted features is an important factor in determining the extracted efficiency of a surrogate model, especially when the model is embedded into the hardware chip. At the stage of fitting scattering parameter matrix, 101 real numbers are extracted from the discrete responses data (101 = 25 + 21 + 17 + 21 + 17). At the stage of the correction, there are three correctional coefficient numbers in the logarithmic function. Even though a more complicated function is used to correct a much broader dynamic range, its numbers would be fewer. Finally, the total extracted numbers for the surrogate model in this chapter are only 104 (104 = 101 + 3), which is much less than 475 in the last chapter. Thus, the surrogate model within equivalent network analysis has a higher compression ratio, which will lead to lower cost and faster reaction when integrating the original reconfigurable antenna into a

communication system.

However, this surrogate model is only applied for a reconfigurable antenna with electronic loadings, not for antennas using other reconfigurable mechanisms. That is the limitation of this model, while the RFWI approach in [92] can be applied in all kinds of frequency reconfigurable antenna, including mechanical and material reconfiguration.

8.6 Summary

In this chapter, a reconfigurable UWB antenna with tunable notched-band, the same antenna in Chapter 7, has been taken as an application to obtain a physics-based surrogate model combining the Rational Fitting with Weight Iteration (RFWI) approach and equivalent network analysis. The physics-based surrogate modelling approach is feasible and efficient, and it has fewer extracted numbers with a wider reconfigurable range than the data-driven surrogate model in Chapter 7.

Chapter 9

Conclusions and Future Work

9.1 Conclusions

This thesis describes innovative research into ”Feature Extraction from Reconfigurable Antenna”. It is a completed modelling system, including guiding principles, analytical function fitting derivation, equivalent circuit/network techniques, surrogate modelling applications to two traditional antennas, a data-driven surrogate modelling application to a reconfigurable UWB antenna, and a physics-based surrogate modelling application to a reconfigurable UWB antenna. All the applications demonstrate that the new perspectives, theories and methods in this thesis are feasible, effective, and accurate. The obtained surrogate models have fewer extracted features, higher fidelity, and a broader dynamic range. Furthermore, the surrogate model technique has many other potential applications. Firstly, it can be used for arbitrary frequency reconfigurable antenna because of its universality. Secondly, it can be applied for a practical reconfigurable antenna, when the initial input data of the surrogate is the discrete response data from practical VNA measurement. Thirdly, the extracted surrogate model is necessary to integrate the complicated reconfigurable antenna into a communication system for both software and hardware aspects. Last but not least, it is convenient to combine Artificial Intelligence (AI) to realize the automated design in the microwave and RF areas in the future.

9.1.1 Analytical Function Fitting

In this thesis, the analytical rational function fitting has been presented. In particular, it is suitable for the responses of microwave systems in a complex field. The derivation of functional fitting in mathematics is detailed step by step from real polynomial function, to real rational function, to complex polynomial function, until complex rational function. During this section, the general algorithms and computational programme algorithms have been presented. Furthermore, for non-linear function fitting, a novel approach, Rational Fitting with Weighted Iteration (RFWI), has been

developed. It combines the least squares method and weighted iteration to extract the rational function in the complex field from the discrete numerical data of CAD simulation and VNA measurement. This approach is reliable and efficient, and its flexible weighting factor could be adapted to a lot of harsh scenarios, even the precise recognition of a very narrow notched band within an ultra-wideband. It can be as the basic module combined with other algorithms, such as interpolation and network analysis, to find the proper surrogate models of antennas.

9.1.2 Equivalent Circuit and Equivalent Network

In this thesis, the general methods of the equivalent circuit and equivalent network based on rational function have been presented. As the important tools to analyse the electromagnetic structure, the equivalent circuit and network could construct a visualized surrogate model. Because the conversion from the rational function to an equivalent circuit is not unique, several methods are given, such as Directly Translated Method, Partial Fraction Expansion Method, and Continued Fraction. Various topologies of the equivalent circuit composed of basic electronic components, including resistor, capacitor and inductor, provide abundant and flexible choices for a surrogate model. Furthermore, the multiport equivalent network method is developed from the equivalent circuit. That extends the applications, from a simple traditional antenna to a reconfigurable antenna and other microwave systems.

9.1.3 Parameter Extraction from Traditional Antennas

As the applications of function fitting technique and equivalent circuit method, two traditional antennas are chosen to extract fitting rational functions and obtain surrogate models. The first traditional antenna is a chassis antenna with two resonators. The second traditional antenna is a band-notched ultra-wideband (UWB) pyramidal monopole antenna. The surrogate models match well with the CAD simulated responses, including both magnitude and phase. They demonstrate that the RFWI approach and equivalent circuit method are reliable and efficient. The flexible weighting factor and elastic order in the RFWI approach could be adapted to the harsh scenarios and the specific requirements.

9.1.4 Parameter Extraction from Reconfigurable Antenna

For a reconfigurable antenna, a surrogate modelling approach combining Rational Fitting with Weighted Iteration (RFWI) and linear interpolation is developed. It can extract parameters and rational functions from the discrete numerical data of

reconfigurable antenna responses from CAD simulation and VNA measurement. To illustrate the validity and high-fidelity of this surrogate modelling approach, a reconfigurable UWB antenna with a tunable notched band is taken as a challenging application. It has many advantages and potential applications. On account of the elastic order and the adaptable weighting factor, this approach has the flexibility to be widely utilized in complicated scenarios. It has fewer extracted parameters, only 475 real numbers, to construct the proper surrogate model. This approach is not subject to electrical loading reconfiguration.

9.1.5 A Physics-Based Surrogate Model of Reconfigurable Antenna

A physics-based surrogate model, combining Rational Fitting with Weighted Iteration (RFWI) and network analysis, is presented. It is a reliable and efficient approach with high-fidelity to substitute the original reconfigurable antenna within electronic components with a broad dynamic range. To demonstrate its feasibility and benefits, an application to a frequency reconfigurable ultra-wideband antenna with tunable varactors is taken as an example to obtain a successful surrogate model. This surrogate modelling technique has the benefits of fewer extracted numbers, better precision, and a broader variable range because of its physics-based equivalent network analysis.

9.2 Future Work

This work has shown that the surrogate modelling approaches are feasible to replace the traditional antennas and frequency reconfigurable antennas. However, radiation pattern reconfigurable antennas and polarization reconfigurable antennas could not be covered by the surrogate model. Furthermore, the function fitting techniques and equivalent circuit network method as the basic module could combine with other algorithms, such as the hotspot AI algorithms, to expand its applications. Thus, it is a promising area of future research and development in this field.

Some further work can be researched in the future:

1. Obtain the generic surrogate models, which could cover the radiation pattern reconfigurable antenna and the polarization reconfigurable antenna;

2. Combine the RFWI with the Gradient Descent method to optimize the convergence issue to reduce the runtime;

3. Combine the surrogate model with artificial intelligence (AI) algorithms to optimize the antenna system;

4. Integrate the original reconfigurable antenna into a communication system based on the surrogate model;

5. Design signal processing algorithm based on the surrogate model of a reconfigurable antenna to realize the adaptive antenna system;

6. Obtain the generic surrogate model of a filter;

7. Obtain the physics-based surrogate model of a reconfigurable filter;

8. Design the filtering antenna with reconfigurable functionality;

9. Research electronic neuristor based on equivalent circuit and equivalent network methods.

Appendix A

Basic Forms of Function Fitting

A.1 Polynomial Function in Real Field

I. 1-order real polynomial function

The fitting function Y_f with the observable input X and 2 unknown parameters (a_1, a_2), could approximate the observable output Y, as

$$Y \approx Y_f = a_1 X + a_2. \tag{A.1}$$

To display the derivation of each parameter in detail, the expectation operator in statistics is used here. The expectation of the squared residual, labelled as e, is

$$\begin{aligned} e =& E[(Y - Y_f)^2] \\ =& E[(Y - (a_1 X + a_2))^2] \\ =& E[Y^2 + a_1^2 X^2 + a_2^2 - 2a_1 XY - 2a_2 Y + 2a_1 a_2 X] \\ =& E[Y^2] + a_1^2 E[X^2] + a_2^2 - 2a_1 E[XY] - 2a_2 E[Y] + 2a_1 a_2 E[X]. \end{aligned} \tag{A.2}$$

The least squares method is to find the optimal parameters by minimizing the expectation e. Since the fitting function contains 2 unknown parameters (a_1, a_2), there are 2 gradient equations, which are the fitting function on their partial derivatives, respectively,

$$\begin{cases} \dfrac{\partial e}{\partial a_1} = 2a_1 E[X^2] - 2E[XY] + 2a_2 E[X] \\ \dfrac{\partial e}{\partial a_2} = 2a_2 - 2E[Y] + 2a_1 E[X]. \end{cases} \tag{A.3}$$

By setting these gradient equations to zero, a group of equations composed of the unknown parameters (a_1, a_2) is obtained,

$$\begin{cases} \dfrac{\partial e}{\partial a_1} = 0 \\ \dfrac{\partial e}{\partial a_2} = 0. \end{cases} \tag{A.4}$$

Since the fitting function Y_f is a linear function, the gradient equations still keep such linearity that expectation operator $E[\cdot]$ could finally be moved on the observable parameters (X^2, X, Y, XY),

$$\begin{cases} a_1 E[X^2] + a_2 E[X] = E[XY] \\ a_1 E[X] + a_2 = E[Y]. \end{cases} \tag{A.5}$$

Because the unknown parameters (a_1, a_2) are outside of the expectation operator, the final solution of the unknown parameters (a_1, a_2) is easy and accurate to find out. To display the solution clearly, Equation (A.5) could be expressed as the type of matrix equation,

$$\begin{bmatrix} E[X^2] & E[X] \\ E[X] & 1 \end{bmatrix} \begin{bmatrix} a_1 \\ a_2 \end{bmatrix} = \begin{bmatrix} E[XY] \\ E[Y] \end{bmatrix} \tag{A.6}$$

For other order real polynomial function fitting, the process is similar to 1-order real function here since they are all linear functions. Their final solutions to unknown parameters could be accurately and easily obtained.

A.2 Rational Function in Real Field

I. (0, 1)-order real rational function

There are two order numbers in rational function since it is composed of denominator polynomial and numerator polynomial. The fitting function Y_f with the observable input X and 2 unknown parameters (a_1, a_2), could approximate the observable output Y, as

$$Y \approx Y_f = \frac{1}{a_1 X + a_2}. \tag{A.7}$$

To linearize the non-linear rational function, the residual needs to be changed as a new type,

$$r = Y \cdot (a_1 X + a_2) - 1. \tag{A.8}$$

So, the expectation of squared residual, labelled as e, is

$$\begin{aligned} e =& E[(Y \cdot (a_1 X + a_2) - 1)^2] \\ =& E[a_1^2 X^2 Y^2 + a_2^2 Y^2 + 1 + 2a_1 a_2 XY^2 - 2a_1 XY - 2a_2 Y] \\ =& a_1^2 E[X^2 Y^2] + a_2^2 E[Y^2] + 1 + 2a_1 a_2 E[XY^2] - 2a_1 E[XY] - 2a_2 E[Y]. \end{aligned} \tag{A.9}$$

It can be seen that the unknown parameters (a_1, a_2) are outside of the expectation operator. Thus, gradient equations are still easy to get through their partial

derivatives, respectively,

$$\begin{cases} \dfrac{\partial e}{\partial a_1} = 2a_1E[X^2Y^2] + 2a_2E[XY^2] - 2E[XY] \\ \dfrac{\partial e}{\partial a_2} = 2a_2E[Y^2] + 2a_1E[XY^2] - 2E[Y]. \end{cases} \tag{A.10}$$

Likewise, setting these gradient equations to zero can generate the equations, where the unknown parameters (a_1, a_2) can be solved,

$$\begin{cases} \dfrac{\partial e}{\partial a_1} = 0 \\ \dfrac{\partial e}{\partial a_2} = 0 \end{cases} \tag{A.11}$$

The final solution to the unknown parameters (a_1, a_2) is expressed as the type of matrix equation,

$$\begin{bmatrix} E[X^2Y^2] & E[XY^2] \\ E[XY^2] & E[Y^2] \end{bmatrix} \begin{bmatrix} a_1 \\ a_2 \end{bmatrix} = \begin{bmatrix} E[XY] \\ E[Y] \end{bmatrix} \tag{A.12}$$

II. (0, 2)-order real rational function

Likewise, (0, 2)-order real rational function also follows the same process. Since it has 3 unknown parameters (a_1, a_2, a_3), the final matrix equation with a 3×3 matrix is more complicated.

$$Y \approx Y_f = \frac{1}{a_1X^2 + a_2X + a_3} \tag{A.13}$$

After approximation, the expectation of squared residual is

$$\begin{aligned} e =& E[(Y \cdot (a_1X^2 + a_2X + a_3) - 1)^2] \\ =& E[a_1^2X^4Y^2 + a_2^2X^2Y^2 + a_3^2Y^2 + 1 \\ & + 2a_1a_2X^3Y^2 + 2a_1a_3X^2Y^2 - 2a_1X^2Y \\ & + 2a_2a_3XY^2 - 2a_2XY - 2a_3Y] \\ =& a_1^2E[X^4Y^2] + a_2^2E[X^2Y^2] + a_3^2E[Y^2] + 1 \\ & + 2a_1a_2E[X^3Y^2] + 2a_1a_3E[X^2Y^2] - 2a_1E[X^2Y] \\ & + 2a_2a_3E[XY^2] - 2a_2E[XY] - 2a_3E[Y] \end{aligned} \tag{A.14}$$

Setting the gradient equations to zero can generate the equations to find the unknown parameters (a_1, a_2, a_3),

$$\begin{cases} 0 = \dfrac{\partial e}{\partial a_1} = 2a_1E[X^4Y^2] + 2a_2E[X^3Y^2] + 2a_3E[X^2Y^2] - 2E[X^2Y] \\ 0 = \dfrac{\partial e}{\partial a_2} = 2a_2E[X^2Y^2] + 2a_1E[X^3Y^2] + 2a_3E[XY^2] - 2E[XY] \\ 0 = \dfrac{\partial e}{\partial a_3} = 2a_3E[Y^2] + 2a_1E[X^2Y^2] + 2a_2E[XY^2] - 2E[Y] \end{cases} \tag{A.15}$$

The final solution to the unknown parameters (a_1, a_2, a_3) is expressed as the type of matrix equation,

$$\begin{bmatrix} E[X^4Y^2] & E[X^3Y^2] & E[X^2Y^2] \\ E[X^3Y^2] & E[X^2Y^2] & E[XY^2] \\ E[X^2Y^2] & E[XY^2] & E[Y^2] \end{bmatrix} \begin{bmatrix} a_1 \\ a_2 \\ a_3 \end{bmatrix} = \begin{bmatrix} E[X^2Y] \\ E[XY] \\ E[Y] \end{bmatrix}. \tag{A.16}$$

III. (1, 2)-order real rational function

Of course, the numerator order of the rational function could be set as non-zero. It will lead to more unknown parameters.

$$Y \approx Y_f = \frac{X + b_1}{a_1X^2 + a_2X + a_3} \tag{A.17}$$

After approximation, the expectation of squared residual is

$$\begin{aligned} e =& E[(Y \cdot (a_1X^2 + a_2X + a_3) - (X + b_1))^2] \\ =& E[a_1^2X^4Y^2 + a_2^2X^2Y^2 + a_3Y^2 + X^2 + b_1^2 \\ &+ 2a_1a_2X^3Y^2 + 2a_1a_3X^2Y^2 - 2a_1X^3Y - 2a_1b_1X^2Y \\ &+ 2a_2a_3XY^2 - 2a_2X^2Y - 2a_2b_1XY \\ &- 2a_3XY - 2a_3b_1Y + 2b_1X] \end{aligned} \tag{A.18}$$

Setting the gradient equations to zero can generate the equations to find the unknown parameters (a_1, a_2, a_3, b_1),

$$\begin{cases} 0 = \dfrac{\partial e}{\partial a_1} = 2a_1E[X^4Y^2] + 2a_2E[X^3Y^2] + 2a_3E[X^2Y^2] - 2E[X^3Y] - 2b_1E[X^2Y] \\ 0 = \dfrac{\partial e}{\partial a_2} = 2a_2E[X^2Y^2] + 2a_1E[X^3Y^2] + 2a_3E[XY^2] - 2E[X^2Y] - 2b_1E[XY] \\ 0 = \dfrac{\partial e}{\partial a_3} = 2a_3E[Y^2] + 2a_1E[X^2Y^2] + 2a_2E[XY^2] - 2E[XY] - 2b_1E[Y] \\ 0 = \dfrac{\partial e}{\partial b_1} = 2b_1 - 2a_1E[X^2Y] - 2a_2E[XY] - 2a_3E[Y] + 2E[X] \end{cases} \tag{A.19}$$

The final solution to the unknown parameters(a_1, a_2, a_3, b_1) is expressed as the type of matrix equation,

$$\begin{bmatrix} E[X^4Y^2] & E[X^3Y^2] & E[X^2Y^2] & -E[X^2Y] \\ E[X^3Y^2] & E[X^2Y^2] & E[XY^2] & -E[XY] \\ E[X^2Y^2] & E[XY^2] & E[Y^2] & -E[Y] \\ E[X^2Y] & E[XY] & E[Y] & -1 \end{bmatrix} \begin{bmatrix} a_1 \\ a_2 \\ a_3 \\ b_1 \end{bmatrix} = \begin{bmatrix} E[X^3Y] \\ E[X^2Y] \\ E[XY] \\ E[X] \end{bmatrix} \tag{A.20}$$

A.3 Polynomial Function in Complex Field

I. 1-order complex polynomial function

The fitting function Z_f with the observable input variable s and 2 unknown parameters (a_1, a_2), approximating the observable output Z, is,

$$Z \approx Z_f = a_1 s + a_2. \tag{A.21}$$

The subscript letter f of Z_f means fitting. Z_f is the function of s, so its complete expression is $Z_f(s)$. The notation s is related to frequency f or ω ($s = j2\pi f$, or $s = j\omega$) in Fourier transform and Laplace transform. The fitting function Z_f and observable Z are in a complex field, and the input variable s is a pure imaginary number, while the unknown parameters (a_1, a_2) are in the real field. So, $Z, Z_f, s \in \mathbb{C}$ and $a_1, a_2 \in \mathbb{R}$. They can be expressed as

$$\begin{cases} Z = R + jX \\ s = j\omega \end{cases}, \tag{A.22}$$

where R, X, and ω are real numbers ($R, X, \omega \in \mathbb{R}$). Likewise, the expectation of squared residual e is

$$\begin{aligned} e =& E[|Z - Z_f|^2] \\ =& E[|Z - (a_1 s + a_2)|^2] \\ =& E[|(R + jX) - (ja_1\omega + a_2)|^2] \\ =& E[(R - a_2)^2] + E[(X - a_1\omega)^2] \\ =& E[R^2] - 2a_2E[R] + a_2^2 + E[X^2] - 2a_1E[\omega X] + a_1^2E[\omega^2], \end{aligned} \tag{A.23}$$

where the residual is the modulus of the difference between 2 complex numbers (Z, Z_f). By setting the gradient equations to zero, the unknown parameters can be found accurately,

$$\begin{cases} 0 = \dfrac{\partial e}{\partial a_1} = -2E[\omega X] + 2a_1E[\omega^2] \\ 0 = \dfrac{\partial e}{\partial a_2} = -2E[R] + 2a_2 \end{cases} \tag{A.24}$$

The final solution to the unknown parameters (a_1, a_2) is expressed as the type of matrix equation,

$$\begin{bmatrix} E[\omega^2] & 0 \\ 0 & 1 \end{bmatrix} \begin{bmatrix} a_1 \\ a_2 \end{bmatrix} = \begin{bmatrix} E[\omega X] \\ E[R] \end{bmatrix} \tag{A.25}$$

From the final matrix equation, the unknown parameters (a_1, a_2) could be figured out in the real field since in this equation all observable data are real numbers.

II. 2-order complex polynomial function

Likewise, 2-order polynomial function fitting can be figured out accurately, as well.

$$Z \approx Z_f = a_1 s^2 + a_2 s + a_3 \tag{A.26}$$

$$\begin{cases} Z = R + jX \\ s = j\omega \end{cases} \tag{A.27}$$

The expectation of squared residual e is

$$\begin{aligned} e =& E[|Z - Z_f|^2] \\ =& E[|Z - (a_1 s^2 + a_2 s + a_3)|^2] \\ =& E[(R + a_1\omega^2 - a_3)^2] + E[(X - a_2\omega)^2] \\ =& E[R^2] + a_1^2E[\omega^4] + a_3^2 + 2a_1E[\omega^2 R] - 2a_3E[R] - 2a_1a_3E[\omega^2] \\ & + E[X^2] - 2a_2E[\omega X] + a_2^2E[\omega^2] \end{aligned} \tag{A.28}$$

Setting the gradient equations to zero can generate the equations to find out the unknown parameters,

$$\begin{cases} 0 = \dfrac{\partial e}{\partial a_1} = 2a_1 E[\omega^4] + 2E[\omega^2 R] - 2a_3 E[\omega^2] \\ 0 = \dfrac{\partial e}{\partial a_2} = -2E[\omega X] + 2a_2 E[\omega^2] \\ 0 = \dfrac{\partial e}{\partial a_3} = 2a_3 - 2E[R] - 2a_1 E[\omega^2] \end{cases} \tag{A.29}$$

The final solution to the unknown parameters (a_1, a_2, a_3) is expressed as the type of matrix equation,

$$\begin{bmatrix} E[\omega^4] & 0 & -E[\omega^2] \\ 0 & E[\omega^2] & 0 \\ -E[\omega^2] & 0 & 1 \end{bmatrix} \begin{bmatrix} a_1 \\ a_2 \\ a_3 \end{bmatrix} = \begin{bmatrix} -E[\omega^2 R] \\ E[\omega X] \\ E[R] \end{bmatrix} \tag{A.30}$$

Although the matrix equation is also regular, it is entirely different from that of the polynomial function fitting in the real field, such as Equation (A.6). Actually, these differences come from the Euclidean norm and complex field in Equation (A.28).

A.4 Rational Function in Complex Field

I. (0, 1)-order complex rational function

(0, 1)-order complex rational function is the simplest type, since its numerator is constant and its denominator contains 2 unknown parameters (a_1, a_2).

$$Z \approx Z_f = \frac{1}{a_1 s + a_2} \tag{A.31}$$

$$\begin{cases} Z = R + jX \\ s = j\omega \end{cases} \tag{A.32}$$

To linearize the non-linear rational function, the residual needs to be changed. So, the expectation of squared residual, labelled as e, is

$$\begin{aligned} e =& E[|Z \cdot (a_1 s + a_2) - 1|^2] \\ =& E[|(R + jX)(ja_1\omega + a_2) - 1|^2] \\ =& E[(a_2 R - a_1\omega X - 1)^2] + E[(a_2 X + a_1\omega R)^2] \\ =& a_2^2 E[R^2] + a_1^2 E[\omega X^2] + 1 - 2a_1 a_2 E[\omega RX] - 2a_2 E[R] + 2a_1 E[\omega X] \\ &+ a_2^2 E[X^2] + a_1^2 E[\omega^2 R^2] + 2a_1 a_2 E[\omega RX] \end{aligned} \tag{A.33}$$

It can be seen that the unknown parameters (a_1, a_2) are outside of the expectation operator. Thus, the gradient equations are still easy to get through their partial derivatives, respectively,

$$\begin{cases} 0 = \dfrac{\partial e}{\partial a_1} = 2a_1 E[\omega X^2] + 2E[\omega X] + 2a_1 E[\omega^2 R^2] \\ 0 = \dfrac{\partial e}{\partial a_2} = 2a_2 E[R^2] - 2E[R] + 2a_2 E[X^2] \end{cases} \tag{A.34}$$

Setting these gradient equations to zero can generate the equations. The final solution to the unknown parameters (a_1, a_2) is expressed as the type of matrix equation,

$$\begin{bmatrix} E[\omega^2 R^2] + E[\omega^2 X^2] & 0 \\ 0 & E[R^2] + E[X^2] \end{bmatrix} \begin{bmatrix} a_1 \\ a_2 \end{bmatrix} = \begin{bmatrix} -E[\omega X] \\ E[R] \end{bmatrix} \tag{A.35}$$

II. (0, 2)-order complex rational function

Likewise, (0, 2)-order complex rational function follows the same process, as well. Since it has 3 unknown parameters (a_1, a_2, a_3), the final matrix equation with a 3×3 matrix is more complicated.

$$Z \approx Z_f = \frac{1}{a_1 s^2 + a_2 s + a_3} \tag{A.36}$$

$$\begin{cases} Z = R + jX \\ s = j\omega \end{cases} \tag{A.37}$$

After approximation, the expectation of squared residual is

$$
\begin{aligned}
e =& E[|Z \cdot (a_1 s^2 + a_2 s + a_3) - 1|^2] \\
=& E[|(R + jX)(-a_1\omega^2 + ja_2\omega + a_3) - 1|^2] \\
=& E[(-a_1\omega^2 R + a_3 R - a_2\omega X - 1)^2] + E[(a_2\omega R - a_1\omega^2 X + a_3 X)^2] \\
=& E[a_1^2\omega^4 R^2 + a_3^2 R^2 + a_2^2\omega^2 X^2 + 1 - 2a_1a_3\omega^2 R^2 + 2a_1a_2\omega^3 RX + 2a_1\omega^2 R \\
& - 2a_2a_3\omega RX - 2a_3 R + 2a_2\omega X] \\
& + E[a_2^2\omega^2 R^2 + a_1^2\omega^4 X^2 + a_3^2 X^2 - 2a_1a_2\omega^3 RX + 2a_2a_3\omega RX - 2a_1a_3\omega^2 X^2] \\
=& a_1^2 E[\omega^4 R^2] + a_3^2 E[R^2] + a_2^2 E[\omega^2 X^2] + 1 \\
& - 2a_1a_3 E[\omega^2 R^2] + 2a_1a_2 E[\omega^3 RX] + 2a_1 E[\omega^2 R] \\
& - 2a_2a_3 E[\omega RX] - 2a_3 E[R] + 2a_2 E[\omega X] \\
& + a_2^2 E[\omega^2 R^2] + a_1^2 E[\omega^4 X^2] + a_3^2 E[X^2] \\
& - 2a_1a_2 E[\omega^3 RX] + 2a_2a_3 E[\omega RX] - 2a_1a_3 E[\omega^2 X^2]
\end{aligned}
\tag{A.38}
$$

Setting the gradient equation to zero can generate the equations to find the unknown parameters (a_1, a_2, a_3),

$$
\begin{cases}
0 = \dfrac{\partial e}{\partial a_1} = 2a_1 E[\omega^4 R^2] - 2a_3 E[\omega^2 R^2] + 2E[\omega^2 R] + 2a_1 E[\omega^4 X^2] - 2a_3 E[\omega^2 X^2] \\
0 = \dfrac{\partial e}{\partial a_2} = 2a_2 E[\omega^2 X^2] + 2E[\omega X] + 2a_2 E[\omega^2 R^2] \\
0 = \dfrac{\partial e}{\partial a_3} = 2a_3 E[R^2] - 2a_1 E[\omega^2 R^2] - 2E[R] + 2a_3 E[X^2] - 2a_1 E[\omega^2 X^2]
\end{cases}
\tag{A.39}
$$

The final solution to the unknown parameters (a_1, a_2, a_3) is expressed as the type of matrix equation,

$$
\begin{bmatrix}
E[\omega^4 R^2] + E[\omega^4 X^2] & 0 & -E[\omega^2 R^2] - E[\omega^2 X^2] \\
0 & E[\omega^2 R^2] + E[\omega^2 X^2] & 0 \\
-E[\omega^2 R^2] - E[\omega^2 X^2] & 0 & E[R^2] + E[X^2]
\end{bmatrix}
\cdot
\begin{bmatrix} a_1 \\ a_2 \\ a_3 \end{bmatrix}
=
\begin{bmatrix} -E[\omega^2 R] \\ -E[\omega X] \\ E[R] \end{bmatrix}
\tag{A.40}
$$

Compared with Equation (A.16), the Matrix Equation (A.40) of a complex rational function is more complicated.

III. (1, 2)-order complex rational function

Of course, the numerator order of the rational function could be set as non-zero. It will lead to more unknown parameters.

$$Z \approx Z_f = \frac{s + b_1}{a_1 s^2 + a_2 s + a_3} \tag{A.41}$$

$$\begin{cases} Z = R + jX \\ s = j\omega \end{cases} \tag{A.42}$$

After approximation, the expectation of squared residual is

$$\begin{aligned}
e =& E[|Z \cdot (a_1 s^2 + a_2 s + a_3) - (s + b_1)|^2] \\
=& E[|(R + jX)(-a_1\omega^2 + ja_2\omega + a_3) - (j\omega + b_1)|^2] \\
=& E[(-a_1\omega^2 R + a_3 R - a_2\omega X - b_1)^2] + E[(a_2\omega R - a_1\omega^2 X + a_3 X - \omega)^2] \\
=& E[a_1^2\omega^4 R^2 + a_3^2 R^2 + a_2^2\omega^2 X^2 + b_1^2 - 2a_1a_3\omega^2 R^2 + 2a_1a_2\omega^3 RX + 2a_1b_1\omega^2 R \\
& - 2a_2a_3\omega RX - 2a_3b_1 R + 2a_2b_1\omega X] \\
& + E[a_2^2\omega^2 R^2 + a_1^2\omega^4 X^2 + a_3^2 X^2 + \omega^2 - 2a_1a_2\omega^3 RX + 2a_2a_3\omega RX - 2a_2\omega^2 R \\
& - 2a_1a_3\omega^2 X^2 + 2a_1\omega^3 X - 2a_3\omega X] \\
=& a_1^2 E[\omega^4 R^2] + a_3^2 E[R^2] + a_2^2 E[\omega^2 X^2] + b_1^2 \\
& - 2a_1a_3 E[\omega^2 R^2] + 2a_1a_2 E[\omega^3 RX] + 2a_1b_1 E[\omega^2 R] \\
& - 2a_2a_3 E[\omega RX] - 2a_3b_1 E[R] + 2a_2b_1 E[\omega X] \\
& + a_2^2 E[\omega^2 R^2] + a_1^2 E[\omega^4 X^2] + a_3^2 E[X^2] + E[\omega^2] \\
& - 2a_1a_2 E[\omega^3 RX] + 2a_2a_3 E[\omega RX] - 2a_2 E[\omega^2 R] \\
& - 2a_1a_3 E[\omega^2 X^2] + 2a_1 E[\omega^3 X] - 2a_3 E[\omega X]
\end{aligned} \tag{A.43}$$

Setting the gradient equations to zero can generate the equations to find the unknown parameters (a_1, a_2, a_3, b_1),

$$\begin{cases} 0 = \dfrac{\partial e}{\partial a_1} = 2a_1E[\omega^4R^2] - 2a_3E[\omega^2R^2] + 2b_1E[\omega^2R] \\ \qquad\qquad +2a_1E[\omega^4X^2] - 2a_3E[\omega^2X^2] + 2E[\omega^3X] \\ 0 = \dfrac{\partial e}{\partial a_2} = 2a_2E[\omega^2X^2] + 2b_1E[\omega X] + 2a_2E[\omega^2R^2] - 2E[\omega^2R] \\ 0 = \dfrac{\partial e}{\partial a_3} = 2a_3E[R^2] - 2a_1E[\omega^2R^2] - 2b_1E[R] \\ \qquad\qquad +2a_3E[X^2] - 2a_1E[\omega^2X^2] - 2E[\omega X] \\ 0 = \dfrac{\partial e}{\partial b_1} = 2b_1 + 2a_1E[\omega^2R] - 2a_3E[R] + 2a_2E[\omega X] \end{cases} \tag{A.44}$$

The final solution to the unknown parameters(a_1, a_2, a_3, b_1) is expressed as the type of matrix equation,

$$\begin{bmatrix} E[\omega^4R^2]+E[\omega^4X^2] & 0 & -E[\omega^2R^2]-E[\omega^2X^2] & E[\omega^2R] \\ 0 & E[\omega^2R^2]+E[\omega^2X^2] & 0 & E[\omega X] \\ -E[\omega^2R^2]-E[\omega^2X^2] & 0 & E[R^2]+E[X^2] & -E[R] \\ E[\omega^2R] & E[\omega X] & -E[R] & 1 \end{bmatrix} \cdot \begin{bmatrix} a_1 \\ a_2 \\ a_3 \\ b_1 \end{bmatrix} = \begin{bmatrix} -E[\omega^3X] \\ E[\omega^2R] \\ E[\omega X] \\ 0 \end{bmatrix} \tag{A.45}$$

The Matrix Equation (A.45) is much more complicated than Equation (A.20) in the real field.

Appendix B

Basic Forms of Equivalent Circuit

B.1 Directly Translated Method

B.1.1 Group of Resistors and Capacitors

I. $m = n = 1$

The (1, 1)-order rational function is as:

$$Z(s) = \frac{s + b_1}{a_1 s + a_2}. \tag{B.1}$$

It can convert to the equivalent circuit topology in Figure B.1. There are 3 parameters (a_1, a_2, b_1) in Equation (B.1), so the 3 unknown parameters (R_1, R_2, C_1) in Figure B.1 can be figured out through the following methods.

Method A

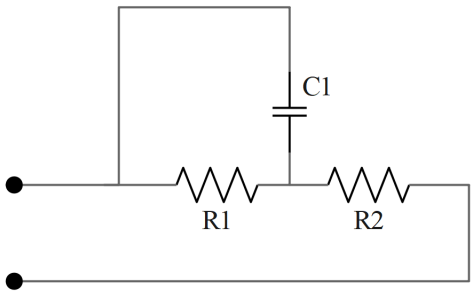

FIGURE B.1: Equivalent circuit composed of resistors and capacitor for (1, 1)-order rational function.

The equivalent impedance in Figure B.1 is

$$\begin{aligned} Z(s) =& R_2 + R_1 \mathbin{/\!/} \frac{1}{sC_1} \\ =& \frac{sC_1R_1R_2 + R_1 + R_2}{sC_1R_1 + 1} \\ =& \frac{s + \dfrac{R_1 + R_2}{C_1R_1R_2}}{s \cdot \dfrac{1}{R_2} + \dfrac{1}{C_1R_1R_2}} \end{aligned} \tag{B.2}$$

For the variable s, Equation (B.2) has the same type as Equation (B.1). Comparing their counterpart coefficients, we can get the equations group,

$$\begin{cases} a_1 = \dfrac{1}{R_2} \\ a_2 = \dfrac{1}{C_1R_1R_2} \\ b_1 = \dfrac{R_1 + R_2}{C_1R_1R_2} \end{cases} \tag{B.3}$$

Through Equations (B.3), the unknown components (R_1, R_2, C_1) in Figure B.1 can be solved,

$$\begin{cases} C_1 = \dfrac{a_1^2}{a_1b_1 - a_2} \\ R_1 = \dfrac{a_1b_1 - a_2}{a_1a_2} \\ R_2 = \dfrac{1}{a_1} \end{cases} \tag{B.4}$$

So far, the equivalent circuit within resistors and capacitor in Figure B.1 is obtained from its corresponding (1, 1)-order rational function in Equation (B.1).

Method B

The corresponding equivalent circuit within resistors and capacitor in Figure B.1 can be constructed through Kirchhoff's Current/Voltage Laws. Each branch's current of the equivalent circuit could be marked in Figure B.2.

Based on Kirchhoff's Current Law (KCL), the equations are

$$\begin{cases} i_{R_2} = i \\ i_{C_1} + i_{R_1} - i_{R_2} = 0 \end{cases} \tag{B.5}$$

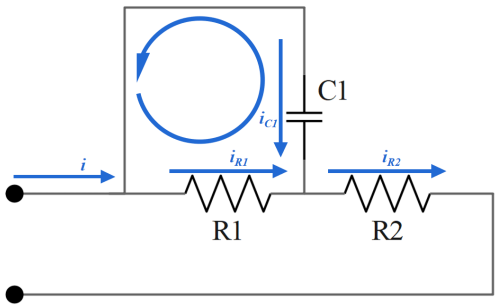

FIGURE B.2: The current in equivalent circuit composed of resistors and capacitor for (1, 1)-order rational function.

Based on Kirchhoff's Voltage Law (KVL), the equation is

$$-\frac{1}{sC_1}\cdot i_{C_1} + R_1 i_{R_1} = 0 \tag{B.6}$$

To solve the problem clearly, Equations (B.5) and Equation (B.6) can be spliced together and expressed as the type of matrix equation,

$$\begin{bmatrix} 0 & 0 & 1 \\ 1 & 1 & -1 \\ -\frac{1}{sC_1} & R_1 & 0 \end{bmatrix} \begin{bmatrix} i_{C_1} \\ i_{R_1} \\ i_{R_2} \end{bmatrix} = \begin{bmatrix} i \\ 0 \\ 0 \end{bmatrix} \tag{B.7}$$

In Matrix Equation (B.7), the vector $(i_{C_1}, i_{R_1}, i_{R_2})^T$ contains 3 branch currents and the 3×3 matrix is composed of lumped components. Thus, the vector $(i_{C_1}, i_{R_1}, i_{R_2})^T$ can be solved and expressed by the lumped components. Then, the equivalent impedance of the circuit can be expressed by the lumped components,

$$Z(s) = \frac{\sum_j R_j i_{R_j}}{i} = \frac{R_1 i_{R_1} + R_2 i_{R_2}}{i}. \tag{B.8}$$

The completed expression of Equation (B.8) is Equation (B.2). Thus, the subsequent process is the same as that in Method A.

Compared with Method A, the process of Method B has more steps. However, the matrix equation in Method B is regular to be easily extended to the higher order. Furthermore, in Method B, more information about the circuit can be obtained, such as the current of each branch and the voltage of each node.

II. $m = n = 2$

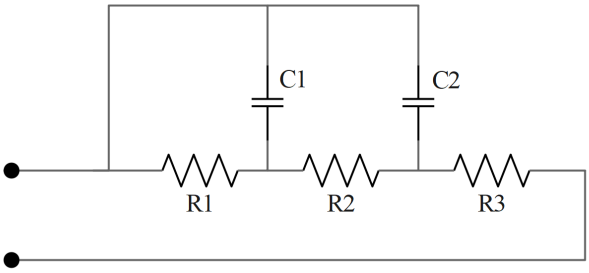

FIGURE B.3: Equivalent circuit composed of resistors and capacitors for (2, 2)-order rational function.

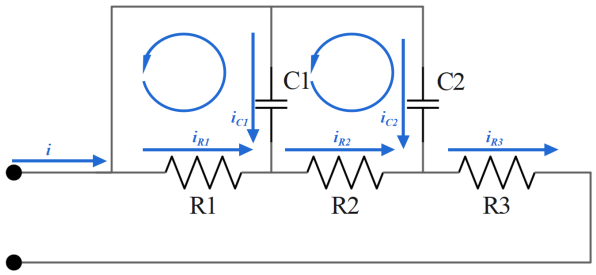

FIGURE B.4: The current in equivalent circuit composed of resistors and capacitors for (2, 2)-order rational function.

The (2, 2)-order rational function is as:

$$Z(s) = \frac{s^2 + b_1 s + b_2}{a_1 s^2 + a_2 s + a_3}. \tag{B.9}$$

It can convert to the equivalent circuit topology in Figure B.3. There are 5 parameters (a_1, a_2, a_3, b_1, b_2) in Equation (B.9), so that the 5 unknown parameters (R_1, R_2, R_3, C_1, C_2) in Figure B.3 can be figured out through the following methods.

Method A

The equivalent impedance in Figure B.3 is

$$Z(s) = R_3 + \frac{1}{sC_2} \,/\!/\, (R_2 + \frac{1}{sC_1} \,/\!/\, R_1) \tag{B.10}$$

Method B

The corresponding equivalent circuit within resistors and capacitor in Figure B.3 can be built through Kirchhoff's Current/Voltage Laws. Each branch's current of the equivalent circuit could be marked in Figure B.4.

Based on Kirchhoff's Current Law (KCL), the equations are

$$\begin{cases} i_{R_3} = i \\ i_{C_1} + i_{R_1} - i_{R_2} = 0 \\ i_{C_2} + i_{R_2} - i_{R_3} = 0 \end{cases} \tag{B.11}$$

Based on Kirchhoff's Voltage Law (KVL), the equations are

$$\begin{cases} -\dfrac{1}{sC_1} i_{C_1} + R_1 i_{R_1} = 0 \\ \dfrac{1}{sC_1} i_{C_1} - \dfrac{1}{sC_2} i_{C_2} + R_2 i_{R_2} = 0 \end{cases} \tag{B.12}$$

To solve the problem clearly, Equations (B.11) and Equations (B.12) can be spliced together and expressed as the type of matrix equation,

$$\begin{bmatrix} 0 & 0 & 0 & 0 & 1 \\ 1 & 0 & 1 & -1 & 0 \\ 0 & 1 & 0 & 1 & -1 \\ -\frac{1}{sC_1} & 0 & R_1 & 0 & 0 \\ \frac{1}{sC_1} & -\frac{1}{sC_2} & 0 & R_2 & 0 \end{bmatrix} \begin{bmatrix} i_{C_1} \\ i_{C_2} \\ i_{R_1} \\ i_{R_2} \\ i_{R_3} \end{bmatrix} = \begin{bmatrix} i \\ 0 \\ 0 \\ 0 \\ 0 \end{bmatrix} \tag{B.13}$$

In Matrix Equation (B.13), the vector $(i_{C_1}, i_{C_2}, i_{R_1}, i_{R_2}, i_{R_3})^T$ contains 5 branch currents and the 5×5 matrix is composed of lumped components. Thus, the vector $(i_{C_1}, i_{C_2}, i_{R_1}, i_{R_2}, i_{R_3})^T$ can be solved and expressed by the lumped components. Then, the equivalent impedance of the circuit can be expressed by the lumped components,

$$Z(s) = \frac{\sum\limits_j R_j i_{R_j}}{i} = \frac{R_1 i_{R_1} + R_2 i_{R_2} + R_3 i_{R_3}}{i} \tag{B.14}$$

B.1.2 Group of Resistors and Capacitors II

To illustrate the diversity of the conversion from the rational function to its equivalent circuit, another circuit with the same numbers of resistors and capacitors but a different topology is discussed.

I. $m = n = 1$

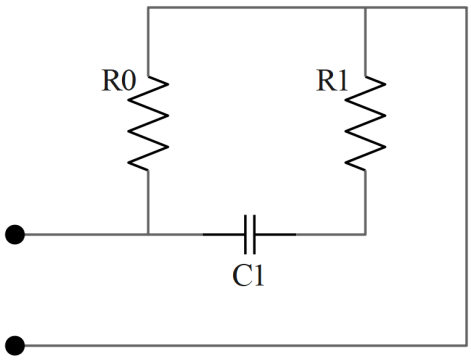

FIGURE B.5: Equivalent circuit composed of resistors and capacitor for (1, 1)-order rational function.

The (1, 1)-order rational function is as:

$$Z(s) = \frac{s + b_1}{a_1 s + a_2} \tag{B.15}$$

It can convert to the equivalent circuit topology in Figure B.5. There are 3 parameters (a_1, a_2, b_1) in Equation (B.15), so that the 3 unknown parameters (R_0, R_1, C_1) in Figure B.5 can be figured out through the following methods.

Method A

The equivalent impedance in Figure B.5 is

$$\begin{aligned} Z(s) =& R_0 \mathbin{/\!/} (\frac{1}{sC_1} + R_1) \\ =& \frac{sC_1R_0R_1 + R_0}{sC_1(R_0 + R_1) + 1} \\ =& \frac{s + \dfrac{1}{C_1R_1}}{s \cdot \dfrac{R_0 + R_1}{R_0R_1} + \dfrac{1}{C_1R_0R_1}} \end{aligned} \tag{B.16}$$

For the variable s, Equation (B.16) has the same type of Equation (B.15). Comparing their counterpart coefficients, we can get the equations

$$\begin{cases} a_1 = \dfrac{R_0 + R_1}{R_0R_1} = \dfrac{1}{R_0} + \dfrac{1}{R_1} \\ a_2 = \dfrac{1}{C_1R_0R_1} \\ b_1 = \dfrac{1}{C_1R_1} \end{cases} \tag{B.17}$$

Through Equations (B.17), the unknown components (R_0, R_1, C_1) can be solved,

$$\begin{cases} C_1 = \dfrac{a_1 b_1 - a_2}{b_1^2} \\ R_0 = \dfrac{b_1}{a_2} \\ R_1 = \dfrac{b_1}{a_1 b_1 - a_2} \end{cases} \tag{B.18}$$

So far, the equivalent circuit within resistors and capacitor in Figure B.5 is obtained from its corresponding (1, 1)-order rational function.

Method B

The corresponding equivalent circuit within resistors and capacitor in Figure B.5 can be constructed through Kirchhoff's Current/Voltage Laws. Each branch's current of the equivalent circuit could be marked in Figure B.6.

Based on Kirchhoff's Current Law (KCL), the equations are

$$\begin{cases} i_{C_1} + i_{R_0} = i \\ i_{C_1} - i_{R_1} = 0 \end{cases} \tag{B.19}$$

Based on Kirchhoff's Voltage Law (KVL), the equation is

$$\frac{1}{sC_1} i_{C_1} - R_0 i_{R_0} + R_1 i_{R_1} = 0 \tag{B.20}$$

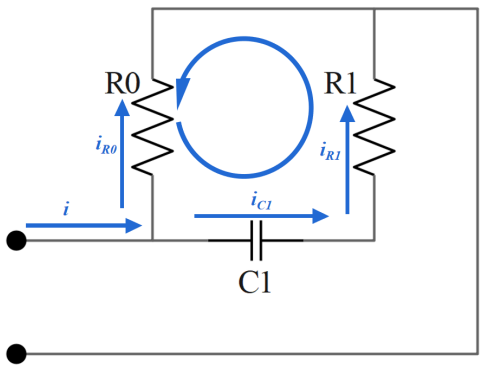

FIGURE B.6: The current in equivalent circuit composed of resistors and capacitor for (1, 1)-order rational function.

To solve the problem clearly, Equations (B.19) and Equation (B.20) can be spliced together and expressed as the type of matrix equation,

$$\begin{bmatrix} 1 & 1 & 0 \\ 1 & 0 & -1 \\ \frac{1}{sC_1} & -R_0 & R_1 \end{bmatrix} \begin{bmatrix} i_{C_1} \\ i_{R_0} \\ i_{R_1} \end{bmatrix} = \begin{bmatrix} i \\ 0 \\ 0 \end{bmatrix} \tag{B.21}$$

In Matrix Equation (B.21), the vector $(i_{C_1}, i_{R_0}, i_{R_1})^T$ contains 3 branch currents and the 3×3 matrix is composed of lumped components. Thus, the vector $(i_{C_1}, i_{R_0}, i_{R_1})^T$ can be solved and expressed by the lumped components. Then, the equivalent impedance of the circuit can be expressed by the lumped components,

$$Z(s) = \frac{R_0 \cdot i_{R_0}}{i} \tag{B.22}$$

The complete expression of Equation (B.22) is Equation (B.16). Thus, the subsequent process is the same as that in Method A.

Compared with Method A, the process of Method B has more steps. However, the matrix equation in Method B is regular to be easily extended to the higher order. Furthermore, in Method B, more information about the circuit can be obtained, such as the current of each branch and the voltage of each node.

II. $m = n = 2$

The (2, 2)-order rational function is as:

$$Z(s) = \frac{s^2 + b_1 s + b_2}{a_1 s^2 + a_2 s + a_3} \tag{B.23}$$

It can convert to the equivalent circuit topology in Figure B.7. There are 5 parameters (a_1, a_2, a_3, b_1, b_2) in Equation (B.23), so that the 5 unknown parameters (R_0, R_1, R_2, C_1, C_2) in Figure B.7 can be figured out through the following methods.

Method A

The equivalent impedance in Figure B.7 is

$$Z(s) = R_0 \mathbin{/\!/} (\frac{1}{sC_1} + R_1 \mathbin{/\!/} (\frac{1}{sC_2} + R_2)) \tag{B.24}$$

Method B

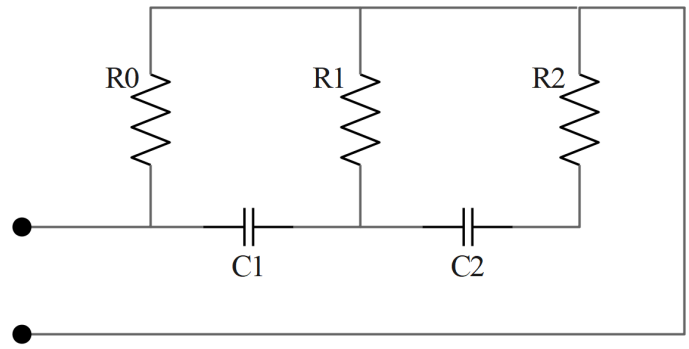

FIGURE B.7: Equivalent circuit composed of resistors and capacitors for (2, 2)-order rational function.

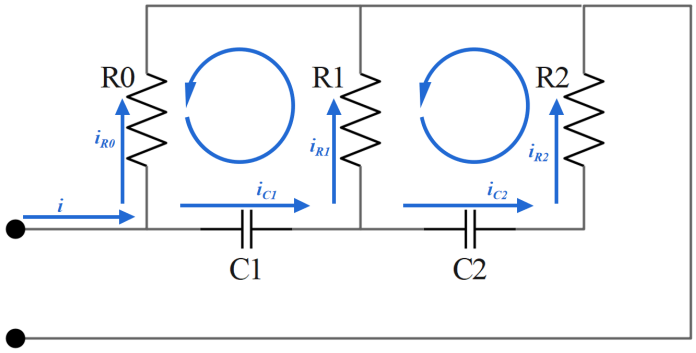

FIGURE B.8: The current in equivalent circuit composed of resistors and capacitors for (2, 2)-order rational function.

The corresponding equivalent circuit within resistors and capacitors in Figure B.7 can be built through Kirchhoff's Current/Voltage Laws. Each branch's current of the equivalent circuit could be marked in Figure B.8.

Based on Kirchhoff's Current Law (KCL), the equations are

$$\begin{cases} i_{C_1} + i_{R_0} = i \\ i_{C_1} - i_{C_2} - i_{R_1} = 0 \\ i_{C_2} - i_{R_2} = 0 \end{cases} \tag{B.25}$$

Based on Kirchhoff's Voltage Law (KVL), the equations are

$$\begin{cases} \dfrac{1}{sC_1} i_{C_1} - R_0 i_{R_0} + R_1 i_{R_1} = 0 \\ \dfrac{1}{sC_2} i_{C_2} - R_1 i_{R_1} + R_2 i_{R_2} = 0 \end{cases} \tag{B.26}$$

To solve the problem clearly, Equations (B.25) and Equations (B.26) can be spliced together and expressed as the type of matrix equation,

$$\begin{bmatrix} 1 & 0 & 1 & 0 & 0 \\ 1 & -1 & 0 & -1 & 0 \\ 0 & 1 & 0 & 0 & -1 \\ \frac{1}{sC_1} & 0 & -R_0 & R_1 & 0 \\ 0 & \frac{1}{sC_2} & 0 & -R_1 & R_2 \end{bmatrix} \begin{bmatrix} i_{C_1} \\ i_{C_2} \\ i_{R_0} \\ i_{R_1} \\ i_{R_2} \end{bmatrix} = \begin{bmatrix} i \\ 0 \\ 0 \\ 0 \\ 0 \end{bmatrix} \tag{B.27}$$

In Matrix Equation (B.27), the vector $(i_{C_1}, i_{C_2}, i_{R_0}, i_{R_1}, i_{R_2})^T$ contains 5 branch currents and the 5×5 matrix is composed of lumped components. Thus, the vector $(i_{C_1}, i_{C_2}, i_{R_0}, i_{R_1}, i_{R_2})^T$ can be solved and expressed by the lumped components. Then, the equivalent impedance of the circuit can be expressed by the lumped components,

$$Z(s) = \frac{R_0 \cdot i_{R_0}}{i} \tag{B.28}$$

B.1.3 Group of Resistors and Inductors

The rational function is also converted to an equivalent circuit composed of the resistors and inductors.

I. $m = n = 1$

The (1, 1)-order rational function is as:

$$Z(s) = \frac{s + b_1}{a_1 s + a_2} \tag{B.29}$$

It can convert to the equivalent circuit topology in Figure B.9. There are 3 parameters (a_1, a_2, b_1) in Equation (B.29), so that the 3 unknown parameters (R_1, R_2, L_1) in Figure B.9 can be figured out through the following methods.

Method A

The equivalent impedance in Figure B.9 is

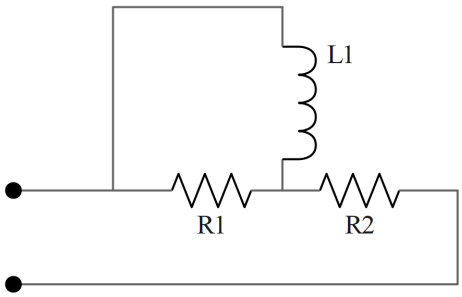

FIGURE B.9: Equivalent circuit composed of resistors and inductor for (1, 1)-order rational function.

$$\begin{aligned} Z(s) =& R_2 + sL_1 \;/\!/\; R_1 \\ =& \frac{sL_1(R_1+R_2)+R_1R_2}{sL_1+R_1} \\ =& \frac{s+\dfrac{R_1R_2}{L_1(R_1+R_2)}}{S\cdot\dfrac{1}{R_1+R_2}+\dfrac{R_1}{L_1(R_1+R_2)}} \end{aligned} \tag{B.30}$$

For the variable s, Equation (B.30) has the same type of Equation (B.29). Comparing their counterpart coefficients, we can get the equations

$$\begin{cases} a_1 = \dfrac{1}{R_1+R_2} \\ a_2 = \dfrac{R_1}{L_1(R_1+R_2)} \\ b_1 = \dfrac{R_1R_2}{L_1(R_1+R_2)} \end{cases} \tag{B.31}$$

Through Equations (B.31), the unknown components (R_1, R_2, L_1) can be solved,

$$\begin{cases} L_1 = \dfrac{1}{a_2} - \dfrac{a_1b_1}{a_2^2} \\ R_1 = \dfrac{1}{a_1} - \dfrac{b_1}{a_2} \\ R_2 = \dfrac{b_1}{a_2} \end{cases} \tag{B.32}$$

So far, the equivalent circuit within resistors and inductor in Figure B.9 is obtained from its corresponding (1, 1)-order rational function.

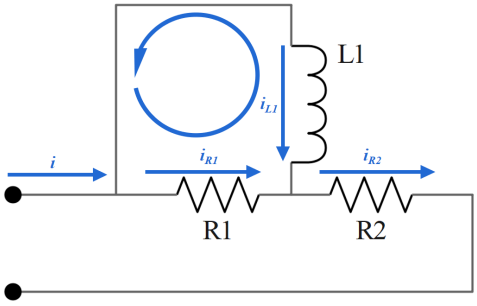

FIGURE B.10: The current in equivalent circuit composed of resistors and inductor for (1, 1)-order rational function.

Method B

The corresponding equivalent circuit within resistors and inductor in Figure B.9 can be constructed through Kirchhoff's Current/Voltage Laws. Each branch's current of the equivalent circuit could be marked in Figure B.10.

Based on Kirchhoff's Current Law (KCL), the equations are

$$\begin{cases} i_{R_2} = i \\ i_{L_1} + i_{R_1} - i_{R_2} = 0 \end{cases} \tag{B.33}$$

Based on Kirchhoff's Voltage Law (KVL), the equation is

$$-sL_1 i_{L_1} + R_1 i_{R_1} = 0 \tag{B.34}$$

To solve the problem clearly, Equations (B.33) and Equation (B.34) can be spliced together and expressed as the type of matrix equation,

$$\begin{bmatrix} 0 & 0 & 1 \\ 1 & 1 & -1 \\ -sL_1 & R_1 & 0 \end{bmatrix} \begin{bmatrix} i_{L_1} \\ i_{R_1} \\ i_{R_2} \end{bmatrix} = \begin{bmatrix} i \\ 0 \\ 0 \end{bmatrix} \tag{B.35}$$

In Matrix Equation (B.35), the vector $(i_{L_1}, i_{R_1}, i_{R_2})^T$ contains 3 branch currents and the 3×3 matrix is composed of lumped components. Thus, the vector $(i_{L_1}, i_{R_1}, i_{R_2})^T$ can be solved and expressed by the lumped components. Then, the equivalent impedance of the circuit can be expressed by the lumped components,

$$Z(s) = \frac{\sum_j R_j i_{R_j}}{i} = \frac{R_1 i_{R_1} + R_2 i_{R_2}}{i} \tag{B.36}$$

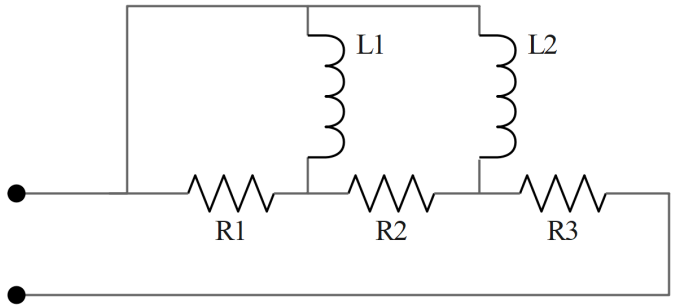

FIGURE B.11: Equivalent circuit composed of resistors and inductors for (2, 2)-order rational function.

II. $m = n = 2$

The (2, 2)-order rational function is as:

$$Z(s) = \frac{s^2 + b_1 s + b_2}{a_1 s^2 + a_2 s + a_3} \tag{B.37}$$

It can convert to the equivalent circuit topology in Figure B.11. There are 5 parameters (a_1, a_2, a_3, b_1, b_2) in Equation (B.37), so that 5 unknown parameters (R_1, R_2, R_3, L_1, L_2) in Figure B.11 can be figured out through the following methods.

Method A

The equivalent impedance in Figure B.11 is

$$Z(s) = R_3 + sL_2 \mathbin{/\!/} (R_2 + sL_1 \mathbin{/\!/} R_1) \tag{B.38}$$

Method B

The corresponding equivalent circuit within resistors and inductors in Figure B.11 can be built through Kirchhoff's Current/Voltage Laws. The current of each branch in an equivalent circuit could be marked in Figure B.12.

Based on Kirchhoff's Current Law (KCL), the equations are

$$\begin{cases} i_{R_3} = i \\ i_{L_1} + i_{R_1} - i_{R_2} = 0 \\ i_{L_2} + i_{R_2} - i_{R_3} = 0 \end{cases} \tag{B.39}$$

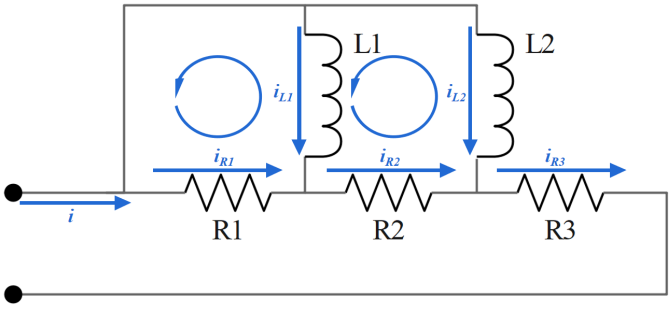

FIGURE B.12: The current in equivalent circuit composed of resistors and inductors for (2, 2)-order rational function.

Based on Kirchhoff's Voltage Law (KVL), the equations are

$$\begin{cases} -sL_1 i_{L_1} + R_1 i_{R_1} = 0 \\ sL_1 i_{L_1} - sL_2 i_{L_2} + R_2 i_{R_2} = 0 \end{cases} \tag{B.40}$$

To solve the problem clearly, Equations (B.39) and Equations (B.40) can be spliced together and expressed as the type of matrix equation,

$$\begin{bmatrix} 0 & 0 & 0 & 0 & 1 \\ 1 & 0 & 1 & -1 & 0 \\ 0 & 1 & 0 & 1 & -1 \\ -sL_1 & 0 & R_1 & 0 & 0 \\ sL_1 & -sL_2 & 0 & R_2 & 0 \end{bmatrix} \begin{bmatrix} i_{L_1} \\ i_{L_2} \\ i_{R_1} \\ i_{R_2} \\ i_{R_3} \end{bmatrix} = \begin{bmatrix} i \\ 0 \\ 0 \\ 0 \\ 0 \end{bmatrix} \tag{B.41}$$

In Matrix Equation (B.41), the vector $(i_{L_1}, i_{L_2}, i_{R_1}, i_{R_2}, i_{R_3})^T$ contains 5 branch currents and the 5×5 matrix is composed of lumped components. Thus, the vector $(i_{L_1}, i_{L_2}, i_{R_1}, i_{R_2}, i_{R_3})^T$ can be solved and expressed by the lumped components. Then, the equivalent impedance of the circuit can be expressed by the lumped components,

$$Z(s) = \frac{\sum_j R_j i_{R_j}}{i} = \frac{R_1 i_{R_1} + R_2 i_{R_2} + R_3 i_{R_3}}{i} \tag{B.42}$$

B.2 Continued Fraction Method

Continued Fraction is also named: method of successive division, division algorithm, and Euclidean algorithm. It can be used to obtain the corresponding equivalent circuit. The equivalent circuit topologies are still various through the Continued Fraction Method. To obtain the correct result, the process of Continued Fraction must follow the explicit topology.

I. 1-order rational function

For 1-order rational function, the equivalent circuit topology is as Figure B.1, so its equivalent impedance is

$$\begin{aligned} Z(s) =& R_2 + \frac{1}{sC_1} \;/\!/\; R_1 \\ =& R_2 + \frac{1}{sC_1 + \dfrac{1}{R_1}} \end{aligned} \tag{B.43}$$

As the type of Equation (B.43), the standard type of 1-order rational function could be operated as

$$\begin{aligned} Z(s) =& \frac{s + b_1}{a_1 s + a_2} \\ =& \frac{1}{a_1} + \frac{b_1 - \dfrac{a_2}{a_1}}{a_1 s + a_2} \\ =& \frac{1}{a_1} + \frac{1}{\dfrac{a_1^2}{a_1 b_1 - a_2} \cdot s + \dfrac{a_1 a_2}{a_1 b_1 - a_2}} \end{aligned} \tag{B.44}$$

Comparing the counterpart coefficients in Equation (B.43) and Equation (B.44), the unknown components (C_1, R_1, R_2) in Figure B.1 can be obtained,

$$\begin{cases} C_1 = \dfrac{a_1^2}{a_1 b_1 - a_2} \\ R_1 = \dfrac{a_1 b_1 - a_2}{a_1 a_2} \\ R_2 = \dfrac{1}{a_1} \end{cases} \tag{B.45}$$

II. 2-order rational function

For 2-order rational function, the equivalent circuit topology is as Figure B.3, so its equivalent impedance is

$$\begin{aligned} Z(s) =& R_3 + \frac{1}{sC_2} \mathbin{/\!/} (R_2 + \frac{1}{sC_1} \mathbin{/\!/} R_1) \\ =& R_3 + \cfrac{1}{sC_2 + \cfrac{1}{R_2 + \cfrac{1}{sC_1 + \cfrac{1}{R_1}}}} \end{aligned} \tag{B.46}$$

As the type of Equation (B.46), the standard type of 2-order rational function could be operated as

$$\begin{aligned} Z(s) =& \frac{s^2 + b_1 s + b_2}{a_1 s^2 + a_2 s + a_3} \\ =& \frac{1}{a_1} + \frac{(b_1 - \frac{a_2}{a_1}) \cdot s + (b_2 - \frac{a_3}{a_1})}{a_1 s^2 + a_2 s + a_3} \\ =& \frac{1}{a_1} + \cfrac{1}{\cfrac{a_1 s^2 + a_2 s + a_3}{\cfrac{a_1 b_1 - a_2}{a_1} \cdot S + \cfrac{a_1 b_2 - a_3}{a_1}}} \\ =& \frac{1}{a_1} + \cfrac{1}{\cfrac{a_1^2}{a_1 b_1 - a_2} \cdot s + \cfrac{(a_2 - \cfrac{a_1^2}{a_1 b_1 - a_2} \cdot \cfrac{a_1 b_2 - a_3}{a_1}) \cdot s + a_3}{\cfrac{a_1 b_1 - a_2}{a_1} \cdot s + \cfrac{a_1 b_2 - a_3}{a_1}}} \\ =& \frac{1}{a_1} + \cfrac{1}{\cfrac{a_1^2}{a_1 b_1 - a_2} \cdot s + \cfrac{\cfrac{a_2 \cdot (a_1 b_1 - a_2) - a_1 \cdot (a_1 b_2 - a_3)}{a_1 b_1 - a_2} \cdot s + a_3}{\cfrac{a_1 b_1 - a_2}{a_1} \cdot s + \cfrac{a_1 b_2 - a_3}{a_1}}} \\ =& \frac{1}{a_1} + \cfrac{1}{\cfrac{a_1^2}{a_1 b_1 - a_2} \cdot s + \cfrac{1}{\cfrac{\cfrac{a_1 b_1 - a_2}{a_1} \cdot s + \cfrac{a_1 b_2 - a_3}{a_1}}{\cfrac{a_2 \cdot (a_1 b_1 - a_2) - a_1 \cdot (a_1 b_2 - a_3)}{a_1 b_1 - a_2} \cdot s + a_3}}} \end{aligned} \tag{B.47}$$

Comparing the counterpart coefficients in Equation (B.46) and Equation (B.47), the unknown components (C_1, C_2, R_1, R_2, R_3) in Figure B.3 can be obtained,

$$\begin{cases} C_1 = & \dfrac{a_1^4 a_2^2 - 2a_1^3 a_2 b_1 b_2 - 2a_1^3 a_3 b_2 + a_1^2 a_2^2 b_1^2 + 2a_1^2 a_2^2 b_2 + 2a_1^2 a_2 a_3 b_1 + ...}{(a_2 - a_1 b_1) \cdot (a_1^2 b_2^2 - a_1 a_2 b_1 b_2 + a_1 a_3 b_1^2 - 2a_1 a_3 b_2 + ...} \\ & \dfrac{... + a_1^2 a_3 - 2a_1 a_2^3 b_1 - 2a_1 a_2^2 a_3 + a_2^4}{... + a_2^2 b_2 - a_2 a_3 b_1 + a_3^2)} \\ C_2 = & \dfrac{a_1^2}{a_1 b_1 - a_2} \\ R_1 = & -\dfrac{a_1^2 b_2^2 - a_1 a_2 b_1 b_2 + a_1 a_3 b_1^2 - 2a_1 a_3 b_2 + a_2^2 b_2 - a_2 a_3 b_1 + a_3^2}{a_3 \cdot (-a_1^2 b_2 + a_1 a_2 b_1 + a_1 a_3 - a_2^2)} \\ R_2 = & \dfrac{(a_1 b_1 - a_2)^2}{a_1 \cdot [a_2 \cdot (a_1 b_1 - a_2) - a_1 \cdot (a_1 b_2 - a_3)]} \\ R_3 = & \dfrac{1}{a_1} \end{cases} \tag{B.48}$$

Appendix C

Data in Chapter 7

TABLE C.1: Unknown coefficient vector $\boldsymbol{x}$ with tunable varactor (0.1pF-1.0pF) from fitting.

Varactor (pF)	a_1 a_6 a_{11} b_3 b_8	a_2 a_7 a_{12} b_4 b_9	a_3 a_8 a_{13} b_5 b_{10}	a_4 a_9 b_1 b_6 b_{11}	a_5 a_{10} b_2 b_7 b_{12}
0.10	3.45×10^{0}	3.05×10^{2}	4.34×10^{4}	2.66×10^{6}	1.92×10^{8}
	8.14×10^{9}	3.72×10^{11}	1.03×10^{13}	3.10×10^{14}	4.99×10^{15}
	1.00×10^{17}	7.00×10^{17}	9.10×10^{18}	-3.55×10^{1}	9.12×10^{3}
	-3.73×10^{5}	3.08×10^{7}	-1.38×10^{9}	4.77×10^{10}	-2.14×10^{12}
	3.50×10^{13}	-1.34×10^{15}	1.14×10^{16}	-2.89×10^{17}	1.09×10^{18}
0.15	3.71×10^{0}	3.07×10^{2}	4.58×10^{4}	2.60×10^{6}	1.99×10^{8}
	7.79×10^{9}	3.81×10^{11}	9.75×10^{12}	3.20×10^{14}	4.78×10^{15}
	1.07×10^{17}	6.91×10^{17}	1.06×10^{19}	-3.51×10^{1}	8.77×10^{3}
	-3.60×10^{5}	2.84×10^{7}	-1.29×10^{9}	4.18×10^{10}	-1.97×10^{12}
	2.84×10^{13}	-1.21×10^{15}	8.10×10^{15}	-2.57×10^{17}	4.81×10^{17}
0.20	3.48×10^{0}	3.04×10^{2}	4.26×10^{4}	2.48×10^{6}	1.81×10^{8}
	7.16×10^{9}	3.40×10^{11}	8.75×10^{12}	2.83×10^{14}	4.24×10^{15}
	9.43×10^{16}	6.13×10^{17}	9.41×10^{18}	-3.33×10^{1}	8.45×10^{3}
	-3.34×10^{5}	2.65×10^{7}	-1.16×10^{9}	3.83×10^{10}	-1.73×10^{12}
	2.58×10^{13}	-1.05×10^{15}	7.35×10^{15}	-2.21×10^{17}	4.60×10^{17}
0.25	3.41×10^{0}	2.95×10^{2}	4.08×10^{4}	2.33×10^{6}	1.70×10^{8}
	6.52×10^{9}	3.10×10^{11}	7.73×10^{12}	2.52×10^{14}	3.64×10^{15}
	8.35×10^{16}	5.08×10^{17}	8.45×10^{18}	-3.35×10^{1}	8.34×10^{3}
	-3.27×10^{5}	2.61×10^{7}	-1.11×10^{9}	3.85×10^{10}	-1.62×10^{12}
	2.74×10^{13}	-9.74×10^{14}	8.82×10^{15}	-2.04×10^{17}	8.49×10^{17}

Varactor (pF)	a_1 a_6 a_{11} b_3 b_8	a_2 a_7 a_{12} b_4 b_9	a_3 a_8 a_{13} b_5 b_{10}	a_4 a_9 b_1 b_6 b_{11}	a_5 a_{10} b_2 b_7 b_{12}
0.30	2.60×10^{0} 5.53×10^{9} 5.31×10^{16} -2.97×10^{5} 3.35×10^{13}	2.74×10^{2} 2.21×10^{11} 3.56×10^{17} 2.67×10^{7} -8.54×10^{14}	3.11×10^{4} 6.26×10^{12} 4.98×10^{18} -9.88×10^{8} 1.29×10^{16}	2.07×10^{6} 1.72×10^{14} -3.12×10^{1} 4.18×10^{10} -1.81×10^{17}	1.26×10^{8} 2.80×10^{15} 8.34×10^{3} -1.42×10^{12} 1.80×10^{18}
0.35	1.89×10^{0} 5.16×10^{9} 3.76×10^{16} -2.57×10^{5} 3.37×10^{13}	2.67×10^{2} 1.66×10^{11} 3.43×10^{16} 2.61×10^{7} -7.29×10^{14}	2.35×10^{4} 5.79×10^{12} 3.32×10^{18} -8.45×10^{8} 1.35×10^{16}	1.97×10^{6} 1.26×10^{14} -2.72×10^{1} 4.11×10^{10} -1.56×10^{17}	9.55×10^{7} 2.62×10^{15} 8.21×10^{3} -1.21×10^{12} 1.99×10^{18}
0.40	1.32×10^{0} 5.02×10^{9} 3.03×10^{16} -2.19×10^{5} 3.25×10^{13}	2.66×10^{2} 1.31×10^{11} 3.68×10^{17} 2.53×10^{7} -6.22×10^{14}	1.78×10^{4} 5.67×10^{12} 2.73×10^{18} -7.15×10^{8} 1.32×10^{16}	1.93×10^{6} 1.00×10^{14} -2.32×10^{1} 3.96×10^{10} -1.35×10^{17}	7.46×10^{7} 2.64×10^{15} 8.06×10^{3} -1.02×10^{12} 1.99×10^{18}
0.45	8.70×10^{-1} 4.94×10^{9} 2.79×10^{16} -1.84×10^{5} 3.20×10^{13}	2.63×10^{2} 1.10×10^{11} 3.96×10^{17} 2.47×10^{7} -5.40×10^{14}	1.37×10^{4} 5.63×10^{12} 2.87×10^{18} -6.06×10^{8} 1.33×10^{16}	1.90×10^{6} 8.71×10^{13} -1.94×10^{1} 3.86×10^{10} -1.19×10^{17}	6.05×10^{7} 2.70×10^{15} 7.96×10^{3} -8.70×10^{11} 2.05×10^{18}
0.50	8.92×10^{-1} 4.79×10^{9} 3.41×10^{16} -1.80×10^{5} 3.43×10^{13}	2.55×10^{2} 1.15×10^{11} 3.91×10^{17} 2.54×10^{7} -5.35×10^{14}	1.40×10^{4} 5.49×10^{12} 4.31×10^{18} -5.91×10^{8} 1.46×10^{16}	1.84×10^{6} 9.58×10^{13} -1.89×10^{1} 4.04×10^{10} -1.20×10^{17}	6.22×10^{7} 2.65×10^{15} 8.07×10^{3} -8.52×10^{11} 2.34×10^{18}
0.55	7.78×10^{-1} 4.72×10^{9} 3.29×10^{16} -1.71×10^{5} 3.37×10^{13}	2.54×10^{2} 1.08×10^{11} 3.91×10^{17} 2.52×10^{7} -5.04×10^{14}	1.29×10^{4} 5.40×10^{12} 4.27×10^{18} -5.58×10^{8} 1.44×10^{16}	1.82×10^{6} 9.10×10^{13} -1.79×10^{1} 3.98×10^{10} -1.13×10^{17}	5.81×10^{7} 2.62×10^{15} 8.02×10^{3} -8.02×10^{11} 2.31×10^{18}
0.60	6.39×10^{-1} 4.59×10^{9} 4.73×10^{16} -1.53×10^{5} 3.82×10^{13}	2.41×10^{2} 1.20×10^{11} 4.12×10^{17} 2.63×10^{7} -5.31×10^{14}	1.23×10^{4} 5.39×10^{12} 7.27×10^{18} -5.23×10^{8} 1.70×10^{16}	1.75×10^{6} 1.12×10^{14} -1.52×10^{1} 4.32×10^{10} -1.25×10^{17}	5.96×10^{7} 2.72×10^{15} 8.17×10^{3} -7.92×10^{11} 2.81×10^{18}
0.65	5.10×10^{-1} 4.50×10^{9} 4.44×10^{16} -1.42×10^{5} 3.76×10^{13}	2.39×10^{2} 1.12×10^{11} 4.03×10^{17} 2.60×10^{7} -4.94×10^{14}	1.11×10^{4} 5.26×10^{12} 6.90×10^{18} -4.87×10^{8} 1.68×10^{16}	1.72×10^{6} 1.05×10^{14} -1.41×10^{1} 4.26×10^{10} -1.17×10^{17}	5.50×10^{7} 2.64×10^{15} 8.13×10^{3} -7.36×10^{11} 2.81×10^{18}

Varactor (pF)	a_1 a_6 a_{11} b_3 b_8	a_2 a_7 a_{12} b_4 b_9	a_3 a_8 a_{13} b_5 b_{10}	a_4 a_9 b_1 b_6 b_{11}	a_5 a_{10} b_2 b_7 b_{12}
0.70	6.01×10^{-1} 4.54×10^{9} 6.22×10^{16} -1.44×10^{5} 4.23×10^{13}	2.32×10^{2} 1.36×10^{11} 4.40×10^{17} 2.75×10^{7} -5.77×10^{14}	1.25×10^{4} 5.48×10^{12} 1.02×10^{19} -5.15×10^{8} 1.93×10^{16}	1.70×10^{6} 1.36×10^{14} -1.37×10^{1} 4.64×10^{10} -1.41×10^{17}	6.38×10^{7} 2.86×10^{15} 8.32×10^{3} -8.17×10^{11} 3.24×10^{18}
0.75	6.64×10^{-1} 4.50×10^{9} 6.74×10^{16} -1.46×10^{5} 4.26×10^{13}	2.29×10^{2} 1.45×10^{11} 4.39×10^{17} 2.76×10^{7} -5.94×10^{14}	1.34×10^{4} 5.44×10^{12} 1.11×10^{19} -5.26×10^{8} 1.94×10^{16}	1.68×10^{6} 1.46×10^{14} -1.37×10^{1} 4.68×10^{10} -1.45×10^{17}	6.78×10^{7} 2.85×10^{15} 8.33×10^{3} -8.39×10^{11} 3.22×10^{18}
0.80	3.67×10^{-1} 4.42×10^{9} 6.01×10^{16} -1.26×10^{5} 4.08×10^{13}	2.29×10^{2} 1.27×10^{11} 4.34×10^{17} 2.69×10^{7} -5.29×10^{14}	1.08×10^{4} 5.32×10^{12} 9.90×10^{18} -4.62×10^{8} 1.85×10^{16}	1.67×10^{6} 1.30×10^{14} -1.13×10^{1} 4.51×10^{10} -1.29×10^{17}	5.83×10^{7} 2.78×10^{15} 8.23×10^{3} -7.43×10^{11} 3.07×10^{18}
0.85	7.86×10^{-2} 4.39×10^{9} 5.79×10^{16} -1.05×10^{5} 4.01×10^{13}	2.27×10^{2} 1.17×10^{11} 4.45×10^{17} 2.66×10^{7} -4.85×10^{14}	8.50×10^{3} 5.31×10^{12} 9.66×10^{18} -4.03×10^{8} 1.81×10^{16}	1.65×10^{6} 1.23×10^{14} -8.45×10^{0} 4.44×10^{10} -1.20×10^{17}	5.15×10^{7} 2.80×10^{15} 8.17×10^{3} -6.68×10^{11} 3.00×10^{18}
0.90	3.03×10^{-1} 4.33×10^{9} 5.59×10^{16} -1.22×10^{5} 3.94×10^{13}	2.28×10^{2} 1.20×10^{11} 4.14×10^{17} 2.64×10^{7} -4.97×10^{14}	1.01×10^{4} 5.14×10^{12} 9.17×10^{18} -4.43×10^{8} 1.77×10^{16}	1.65×10^{6} 1.22×10^{14} -1.09×10^{1} 4.39×10^{10} -1.20×10^{17}	5.53×10^{7} 2.66×10^{15} 8.16×10^{3} -7.05×10^{11} 2.92×10^{18}
0.95	3.96×10^{-1} 4.29×10^{9} 5.20×10^{16} -1.30×10^{5} 3.81×10^{13}	2.31×10^{2} 1.17×10^{11} 3.93×10^{17} 2.61×10^{7} -4.89×10^{14}	1.06×10^{4} 5.02×10^{12} 8.40×10^{18} -4.59×10^{8} 1.70×10^{16}	1.65×10^{6} 1.16×10^{14} -1.24×10^{1} 4.29×10^{10} -1.17×10^{17}	5.54×10^{7} 2.56×10^{15} 8.12×10^{3} -7.10×10^{11} 2.79×10^{18}
1.0	2.24×10^{-1} 4.22×10^{9} 2.60×10^{16} -1.33×10^{5} 3.00×10^{13}	2.47×10^{2} 7.61×10^{10} 3.43×10^{17} 2.36×10^{7} -3.66×10^{14}	7.72×10^{3} 4.67×10^{12} 3.70×10^{18} -4.22×10^{8} 1.26×10^{16}	1.70×10^{6} 6.68×10^{13} -1.41×10^{1} 3.63×10^{10} -8.14×10^{16}	3.92×10^{7} 2.25×10^{15} 7.76×10^{3} -5.89×10^{11} 1.98×10^{18}

TABLE C.2: Variance σ^2 with different varactor.

Varactor (pF)	**0.10**	**0.15**	**0.20**	**0.25**	**0.30**
Variance σ^2	4.72×10^{-5}	5.12×10^{-5}	4.62×10^{-5}	4.76×10^{-5}	6.46×10^{-5}
Varactor (pF)	**0.35**	**0.40**	**0.45**	**0.50**	**0.55**
Variance σ^2	9.65×10^{-5}	1.43×10^{-4}	2.01×10^{-4}	2.41×10^{-4}	2.71×10^{-4}
Varactor (pF)	**0.60**	**0.65**	**0.70**	**0.75**	**0.80**
Variance σ^2	5.50×10^{-4}	4.22×10^{-4}	7.30×10^{-4}	5.60×10^{-4}	4.22×10^{-4}
Varactor (pF)	**0.85**	**0.90**	**0.95**	**1.0**	
Variance σ^2	5.37×10^{-4}	6.89×10^{-4}	7.82×10^{-4}	4.68×10^{-4}	

TABLE C.3: Variance σ^2 with different varactor

Varactor (pF)	**0.12**	**0.18**	**0.22**	**0.28**	**0.32**
Variance σ^2	3.60×10^{-3}	1.58×10^{-3}	4.47×10^{-3}	8.29×10^{-4}	4.20×10^{-3}
Varactor (pF)	**0.38**	**0.42**	**0.48**	**0.52**	**0.58**
Variance σ^2	9.07×10^{-4}	3.07×10^{-3}	9.21×10^{-4}	2.64×10^{-3}	1.14×10^{-3}
Varactor (pF)	**0.62**	**0.68**	**0.72**	**0.78**	**0.82**
Variance σ^2	1.98×10^{-3}	3.19×10^{-3}	1.20×10^{-3}	1.05×10^{-3}	7.09×10^{-4}
Varactor (pF)	**0.88**	**0.92**	**0.98**		
Variance σ^2	7.40×10^{-3}	6.05×10^{-3}	1.26×10^{-3}		

TABLE C.4: Unknown coefficient vector $\boldsymbol{x}$ with tunable varactor from linear interpolation for verfication.

Varactor (pF)	a_1 a_6 a_{11} b_3 b_8	a_2 a_7 a_{12} b_4 b_9	a_3 a_8 a_{13} b_5 b_{10}	a_4 a_9 b_1 b_6 b_{11}	a_5 a_{10} b_2 b_7 b_{12}
0.12	3.60×10^{0} 7.93×10^{9} 1.04×10^{17} -3.65×10^{5} 3.11×10^{13}	3.06×10^{2} 3.78×10^{11} 6.95×10^{17} 2.93×10^{7} -1.26×10^{15}	4.48×10^{4} 9.96×10^{12} 1.00×10^{19} -1.33×10^{9} 9.44×10^{15}	2.63×10^{6} 3.16×10^{14} -3.53×10^{1} 4.42×10^{10} -2.70×10^{17}	1.96×10^{8} 4.87×10^{15} 8.91×10^{3} -2.04×10^{12} 7.23×10^{17}
0.18	3.57×10^{0} 7.41×10^{9} 9.94×10^{16} -3.44×10^{5} 2.68×10^{13}	3.05×10^{2} 3.57×10^{11} 6.44×10^{17} 2.73×10^{7} -1.12×10^{15}	4.39×10^{4} 9.15×10^{12} 9.89×10^{18} -1.22×10^{9} 7.65×10^{15}	2.53×10^{6} 2.98×10^{14} -3.40×10^{1} 3.97×10^{10} -2.36×10^{17}	1.89×10^{8} 4.46×10^{15} 8.58×10^{3} -1.83×10^{12} 4.69×10^{17}
0.22	3.44×10^{0} 6.78×10^{9} 8.78×10^{16} -3.30×10^{5} 2.68×10^{13}	2.99×10^{2} 3.22×10^{11} 5.50×10^{17} 2.63×10^{7} -1.01×10^{15}	4.15×10^{4} 8.14×10^{12} 8.84×10^{18} -1.13×10^{9} 8.23×10^{15}	2.39×10^{6} 2.64×10^{14} -3.34×10^{1} 3.84×10^{10} -2.11×10^{17}	1.74×10^{8} 3.88×10^{15} 8.39×10^{3} -1.67×10^{12} 6.94×10^{17}
0.28	2.93×10^{0} 5.93×10^{9} 6.53×10^{16} -3.09×10^{5} 3.11×10^{13}	2.83×10^{2} 2.57×10^{11} 4.16×10^{17} 2.65×10^{7} -9.02×10^{14}	3.50×10^{4} 6.85×10^{12} 6.37×10^{18} -1.04×10^{9} 1.13×10^{16}	2.18×10^{6} 2.04×10^{14} -3.21×10^{1} 4.05×10^{10} -1.90×10^{17}	1.43×10^{8} 3.14×10^{15} 8.34×10^{3} -1.50×10^{12} 1.42×10^{18}
0.32	2.18×10^{0} 5.31×10^{9} 4.38×10^{16} -2.73×10^{5} 3.36×10^{13}	2.70×10^{2} 1.88×10^{11} 3.48×10^{17} 2.64×10^{7} -7.79×10^{14}	2.65×10^{4} 5.98×10^{12} 3.98×10^{18} -9.02×10^{8} 1.33×10^{16}	2.01×10^{6} 1.44×10^{14} -2.88×10^{1} 4.14×10^{10} -1.66×10^{17}	1.08×10^{8} 2.69×10^{15} 8.26×10^{3} -1.29×10^{12} 1.91×10^{18}
0.38	1.55×10^{0} 5.08×10^{9} 3.32×10^{16} -2.34×10^{5} 3.30×10^{13}	2.66×10^{2} 1.45×10^{11} 3.58×10^{17} 2.56×10^{7} -6.65×10^{14}	2.01×10^{4} 5.72×10^{12} 2.97×10^{18} -7.67×10^{8} 1.34×10^{16}	1.95×10^{6} 1.11×10^{14} -2.48×10^{1} 4.02×10^{10} -1.43×10^{17}	8.29×10^{7} 2.63×10^{15} 8.12×10^{3} -1.09×10^{12} 1.99×10^{18}
0.42	1.05×10^{0} 4.97×10^{9} 2.89×10^{16} -1.98×10^{5} 3.22×10^{13}	2.64×10^{2} 1.18×10^{11} 3.85×10^{17} 2.50×10^{7} -5.73×10^{14}	1.54×10^{4} 5.65×10^{12} 2.82×10^{18} -6.49×10^{8} 1.33×10^{16}	1.91×10^{6} 9.24×10^{13} -2.09×10^{1} 3.90×10^{10} -1.25×10^{17}	6.61×10^{7} 2.68×10^{15} 8.00×10^{3} -9.30×10^{11} 2.03×10^{18}

Varactor (pF)	a_1 a_6 a_{11} b_3 b_8	a_2 a_7 a_{12} b_4 b_9	a_3 a_8 a_{13} b_5 b_{10}	a_4 a_9 b_1 b_6 b_{11}	a_5 a_{10} b_2 b_7 b_{12}
0.48	8.83×10^{-1} 4.85×10^{9} 3.17×10^{16} -1.82×10^{5} 3.34×10^{13}	2.58×10^{2} 1.13×10^{11} 3.93×10^{17} 2.52×10^{7} -5.37×10^{14}	1.39×10^{4} 5.55×10^{12} 3.74×10^{18} -5.97×10^{8} 1.41×10^{16}	1.87×10^{6} 9.23×10^{13} -1.91×10^{1} 3.97×10^{10} -1.19×10^{17}	6.15×10^{7} 2.67×10^{15} 8.03×10^{3} -8.59×10^{11} 2.22×10^{18}
0.52	8.23×10^{-1} 4.75×10^{9} 3.34×10^{16} -1.74×10^{5} 3.39×10^{13}	2.54×10^{2} 1.11×10^{11} 3.91×10^{17} 2.53×10^{7} -5.17×10^{14}	1.33×10^{4} 5.43×10^{12} 4.29×10^{18} -5.71×10^{8} 1.45×10^{16}	1.83×10^{6} 9.29×10^{13} -1.83×10^{1} 4.01×10^{10} -1.16×10^{17}	5.97×10^{7} 2.63×10^{15} 8.04×10^{3} -8.22×10^{11} 2.32×10^{18}
0.58	6.95×10^{-1} 4.64×10^{9} 4.16×10^{16} -1.60×10^{5} 3.64×10^{13}	2.46×10^{2} 1.15×10^{11} 4.04×10^{17} 2.59×10^{7} -5.20×10^{14}	1.25×10^{4} 5.40×10^{12} 6.07×10^{18} -5.37×10^{8} 1.60×10^{16}	1.78×10^{6} 1.04×10^{14} -1.63×10^{1} 4.19×10^{10} -1.20×10^{17}	5.90×10^{7} 2.68×10^{15} 8.11×10^{3} -7.96×10^{11} 2.61×10^{18}
0.62	5.62×10^{-1} 4.54×10^{9} 4.56×10^{16} -1.46×10^{5} 3.78×10^{13}	2.40×10^{2} 1.15×10^{11} 4.06×10^{17} 2.62×10^{7} -5.09×10^{14}	1.16×10^{4} 5.32×10^{12} 7.05×10^{18} -5.01×10^{8} 1.69×10^{16}	1.73×10^{6} 1.08×10^{14} -1.45×10^{1} 4.29×10^{10} -1.20×10^{17}	5.69×10^{7} 2.67×10^{15} 8.14×10^{3} -7.58×10^{11} 2.81×10^{18}
0.68	5.64×10^{-1} 4.53×10^{9} 5.51×10^{16} -1.43×10^{5} 4.04×10^{13}	2.35×10^{2} 1.26×10^{11} 4.25×10^{17} 2.69×10^{7} -5.44×10^{14}	1.19×10^{4} 5.39×10^{12} 8.87×10^{18} -5.03×10^{8} 1.83×10^{16}	1.71×10^{6} 1.24×10^{14} -1.38×10^{1} 4.49×10^{10} -1.31×10^{17}	6.03×10^{7} 2.77×10^{15} 8.24×10^{3} -7.85×10^{11} 3.06×10^{18}
0.72	6.39×10^{-1} 4.52×10^{9} 6.53×10^{16} -1.45×10^{5} 4.25×10^{13}	2.30×10^{2} 1.41×10^{11} 4.39×10^{17} 2.75×10^{7} -5.87×10^{14}	1.31×10^{4} 5.46×10^{12} 1.07×10^{19} -5.22×10^{8} 1.94×10^{16}	1.69×10^{6} 1.42×10^{14} -1.37×10^{1} 4.66×10^{10} -1.43×10^{17}	6.62×10^{7} 2.85×10^{15} 8.33×10^{3} -8.30×10^{11} 3.23×10^{18}
0.78	4.86×10^{-1} 4.46×10^{9} 6.30×10^{16} -1.34×10^{5} 4.15×10^{13}	2.29×10^{2} 1.34×10^{11} 4.36×10^{17} 2.72×10^{7} -5.55×10^{14}	1.18×10^{4} 5.37×10^{12} 1.04×10^{19} -4.88×10^{8} 1.88×10^{16}	1.67×10^{6} 1.36×10^{14} -1.23×10^{1} 4.58×10^{10} -1.35×10^{17}	6.21×10^{7} 2.81×10^{15} 8.27×10^{3} -7.81×10^{11} 3.13×10^{18}
0.82	1.94×10^{-1} 4.41×10^{9} 5.88×10^{16} -1.13×10^{5} 4.04×10^{13}	2.28×10^{2} 1.21×10^{11} 4.40×10^{17} 2.67×10^{7} -5.03×10^{14}	9.41×10^{3} 5.32×10^{12} 9.76×10^{18} -4.27×10^{8} 1.83×10^{16}	1.66×10^{6} 1.26×10^{14} -9.59×10^{0} 4.47×10^{10} -1.24×10^{17}	5.42×10^{7} 2.79×10^{15} 8.19×10^{3} -6.98×10^{11} 3.03×10^{18}

Varactor (pF)	a_1 a_6 a_{11} b_3 b_8	a_2 a_7 a_{12} b_4 b_9	a_3 a_8 a_{13} b_5 b_{10}	a_4 a_9 b_1 b_6 b_{11}	a_5 a_{10} b_2 b_7 b_{12}
0.88	2.13×10^{-1} 4.35×10^{9} 5.67×10^{16} -1.15×10^{5} 3.96×10^{13}	2.28×10^{2} 1.19×10^{11} 4.26×10^{17} 2.65×10^{7} -4.92×10^{14}	9.47×10^{3} 5.21×10^{12} 9.36×10^{18} -4.27×10^{8} 1.78×10^{16}	1.65×10^{6} 1.22×10^{14} -9.93×10^{0} 4.41×10^{10} -1.20×10^{17}	5.38×10^{7} 2.72×10^{15} 8.16×10^{3} -6.90×10^{11} 2.95×10^{18}
0.92	3.59×10^{-1} 4.30×10^{9} 5.36×10^{16} -1.27×10^{5} 3.86×10^{13}	2.30×10^{2} 1.18×10^{11} 4.01×10^{17} 2.62×10^{7} -4.92×10^{14}	1.04×10^{4} 5.07×10^{12} 8.71×10^{18} -4.53×10^{8} 1.72×10^{16}	1.65×10^{6} 1.18×10^{14} -1.18×10^{1} 4.33×10^{10} -1.18×10^{17}	5.54×10^{7} 2.60×10^{15} 8.13×10^{3} -7.08×10^{11} 2.84×10^{18}
0.98	2.93×10^{-1} 4.24×10^{9} 3.64×10^{16} -1.32×10^{5} 3.32×10^{13}	2.41×10^{2} 9.25×10^{10} 3.63×10^{17} 2.46×10^{7} -4.15×10^{14}	8.87×10^{3} 4.81×10^{12} 5.58×10^{18} -4.37×10^{8} 1.43×10^{16}	1.68×10^{6} 8.64×10^{13} -1.34×10^{1} 3.89×10^{10} -9.56×10^{16}	4.57×10^{7} 2.37×10^{15} 7.91×10^{3} -6.38×10^{11} 2.31×10^{18}

Bibliography

[1] D. Cabric, M. S. W. Chen, D. A. Sobel, J. Yang, and R. W. Brodersen, "Future wireless systems: Uwb, 60ghz, and cognitive radios", in *Proceedings of the IEEE 2005 Custom Integrated Circuits Conference, 2005.*, vol. 2005, Institute of Electrical and Electronics Engineers Inc., pp. 793–796.

[2] T. Yücek and H. Arslan, "A survey of spectrum sensing algorithms for cognitive radio applications", *IEEE Communications Surveys and Tutorials*, vol. 11, no. 1, pp. 116–130, 2009.

[3] J. Mitola, "Software radios-survey, critical evaluation and future directions", in *1992 National Telesystems Conference, NTC 1992*, Institute of Electrical and Electronics Engineers Inc., pp. 13/15–13/23.

[4] W. H. W. Tuttlebee, "Software-defined radio: Facets of a developing technology", in *Software Radio Technologies: Selected Readings*. Wiley-IEEE Press, 2001, pp. 31–37.

[5] J. T. Aberle, S. H. Oh, and G. A. Taylor, "Frequency-agile antennas for a software-defined and cognitive radio", in *Printed Antennas for Wireless Communications*. wiley, 2007, pp. 379–405.

[6] T. Ulversoy, "Software defined radio: Challenges and opportunities", *IEEE Communications Surveys and Tutorials*, vol. 12, no. 4, pp. 531–550, 2010.

[7] C. A. Balanis and P. I. Ioannides, "Introduction to smart antennas", in *Synthesis Lectures on Antennas*, vol. 5, 2007, pp. 1–179.

[8] M. Chryssomallis, "Smart antennas", *IEEE Antennas and Propagation Magazine*, vol. 42, no. 3, pp. 129–136, 2000.

[9] A. O. Boukalov and S.-G. Haggman, "System aspects of smart-antenna technology in cellular wireless communications - an overview", *The 1999 Radio and Wireless Conference (RAWCON)*, vol. 48, no. 6, pp. 919–929, 2000.

[10] P. S. Hall, P. Gardner, J. Kelly, E. Ebrahimi, M. R. Hamid, F. Ghanem, F. J. Herraiz-Martínez, and D. Segovia-Vargas, "Reconfigurable antenna challenges for future radio systems", in *2009 3rd European Conference on Antennas and Propagation*, 2009, pp. 949–955.

[11] R.-S. Chen, L. Zhu, S.-W. Wong, X.-Z. Yu, Y. Li, W. He, L. Zhang, and Y. He, "Novel reconfigurable full-metal cavity-backed slot antennas using movable metal posts", *IEEE Transactions on Antennas and Propagation*, vol. 69, no. 10, pp. 6154–6164, 2021.

[12] J. Wang, W. B. Lu, Z. G. Liu, A. Q. Zhang, and H. Chen, "Graphene-based microwave antennas with reconfigurable pattern", *IEEE Transactions on Antennas and Propagation*, vol. 68, no. 4, pp. 2504–2510, 2020.

[13] T. W. Kim, J. S. Park, and S. O. Park, "A theoretical model for resonant frequency and radiation pattern on rectangular microstrip patch antenna on liquid crystal substrate", *IEEE Transactions on Antennas and Propagation*, vol. 66, no. 9, pp. 4533–4540, 2018.

[14] X. L. Chang, P. S. Chee, and E. H. Lim, "Ionic polymer actuator with crenellated structures for mems application", in *IEEE International Conference on Semiconductor Electronics, Proceedings, ICSE*, vol. 2020-July, pp. 160–163.

[15] P. Gardner, A. Feresidis, P. S. Hall, T. J. Jackson, O. Tade, M. Mavridou, Y. Kabiri, and X. Gao, "Frequency reconfiguration in single and dual antenna modules", in *2013 7th European Conference on Antennas and Propagation (EuCAP)*, 2013, pp. 2006–2009.

[16] P. Gardner, M. R. Hamid, P. S. Hall, J. Kelly, F. Ghanem, and E. Ebrahimi, "Reconfigurable antennas for cognitive radio: Requirements and potential design approaches", in *2008 Institution of Engineering and Technology Seminar on Wideband, Multiband Antennas and Arrays for Defence or Civil Applications*, 2008, pp. 89–94.

[17] F. C. Commission *et al.*, "Revision of part 15 of the commission's rules regarding ultra-wideband transmission systems", *First Report And Order, FCC 02-48*, 2002.

[18] R. P. Labade, N. Pishoroty, S. B. Deosarkar, and A. Malahotra, "Compact band-notched printed monopole antenna for ultrawideband communication", in *11th IEEE India Conference, INDICON 2014*, Institute of Electrical and Electronics Engineers Inc., 2014, pp. 1–5.

[19] J. S. Lee, Y. W. Su, and C. C. Shen, "A comparative study of wireless protocols: Bluetooth, uwb, zigbee, and wi-fi", in *33rd Annual Conference of the IEEE Industrial Electronics Society, IECON*, 2007, pp. 46–51.

[20] W. Xiao, R. Wang, J. Song, D. Wu, L. Hu, and M. Chen, "Ai-based satellite ground communication system with intelligent antenna pointing", in *2020 IEEE Global Communications Conference, GLOBECOM 2020*, Institute of Electrical and Electronics Engineers Inc., 2020, pp. 1–6.

[21] F. Andriulli, P. Chen, D. Erricolo, J. Jin, M. Arrebola, M. Li, S. M., R. He, B. Lau, C. Oestges, K. Haneda, and B. Liu, "Special issue announcements", *IEEE Transactions on Antennas and Propagation*, vol. 69, no. 8, pp. 5196–5196, 2021.

[22] Q. Zhang, "Ai and machine learning based technologies for microwaves", *IEEE Transactions on Microwave Theory and Techniques*, vol. 69, no. 3, pp. 1999–2000, 2021.

[23] J. W. Bandler, "The journey to automated design optimization and a vision for the future", in *IEEE MTT-S International Microwave Symposium Digest*, pp. 1517–1519.

[24] H. Zhang, Z. Zhang, R. Zhao, J. Lu, Y. Wang, and P. Jia, "Review on uwb-based and multi-sensor fusion positioning algorithms in indoor environment", in *2021 IEEE 5th Advanced Information Technology, Electronic and Automation Control Conference (IAEAC)*, vol. 5, 2021, pp. 1594–1598.

[25] P. Pannu and D. K. Sharma, "Uwb-mimo antenna with stop band behavior and high isolation", in *2020 IEEE International Women in Engineering (WIE) Conference on Electrical and Computer Engineering (WIECON-ECE)*, Institute of Electrical and Electronics Engineers Inc., 2008, pp. 276–279.

[26] M. Rahman, M. NagshvarianJahromi, S. S. Mirjavadi, and A. M. Hamouda, "Compact uwb band-notched antenna with integrated bluetooth for personal wireless communication and uwb applications", *Electronics (Switzerland)*, vol. 8, no. 2, 2019.

[27] M. R. Hamid, "Wideband reconfigurable antennas", Ph.D. dissertation, School of Electronic, Electrical and Computer Engineering, University of Birmingham, Birmingham, UK, 2011.

[28] M. Tyan, N. V. Nguyen, and J. W. Lee, "Improving variable-fidelity modelling by exploring global design space and radial basis function networks for aerofoil design", *Engineering Optimization*, vol. 47, no. 7, pp. 885–908, 2015.

[29] R. L. Haupt, "Antenna design with a mixed integer genetic algorithm", *IEEE Transactions on Antennas and Propagation*, vol. 55, no. 3 I, pp. 577–582, 2007.

[30] B. Gustavsen and A. Semlyen, "Rational approximation of frequency domain responses by vector fitting", *IEEE Transactions on Power Delivery*, vol. 14, no. 3, pp. 1052–1059, 1999.

[31] S. Grivet-Talocia, "Package macromodeling via time-domain vector fitting", *IEEE Microwave and Wireless Components Letters*, vol. 13, no. 11, pp. 472–474, 2003.

[32] J. E. Rayas-Sánchez, "Power in simplicity with asm: Tracing the aggressive space mapping algorithm over two decades of development and engineering applications", *IEEE Microwave Magazine*, vol. 17, no. 4, pp. 64–76, 2016.

[33] J. C. Melgarejo, J. Ossorio, S. Cogollos, M. Guglielmi, V. E. Boria, and J. W. Bandler, "On space mapping techniques for microwave filter tuning", *IEEE Transactions on Microwave Theory and Techniques*, vol. 67, no. 12, pp. 4860–4870, 2019.

[34] J. W. Bandler, Q. S. Cheng, S. A. Dakroury, A. S. Mohamed, M. H. Bakr, K. Madsen, and J. Søndergaard, "Space mapping: The state of the art", *IEEE Transactions on Microwave Theory and Techniques*, vol. 52, no. 1 II, pp. 337–361, 2004.

[35] H. M. Jafari, M. J. Deen, S. Hranilovic, and N. K. Nikolova, "A study of ultra-wideband antennas for near-field imaging", *IEEE Transactions on Antennas and Propagation*, vol. 55, no. 4, pp. 1184–1188, 2007.

[36] C. X. Mao and Q. X. Chu, "Compact coradiator uwb-mimo antenna with dual polarization", *IEEE Transactions on Antennas and Propagation*, vol. 62, no. 9, pp. 4474–4480, 2014.

[37] H. F. Abutarboush, R. Nilavalan, S. W. Cheung, K. M. Nasr, T. Peter, D. Budimir, and H. Al-Raweshidy, "A reconfigurable wideband and multiband antenna using dual-patch elements for compact wireless devices", *IEEE Transactions on Antennas and Propagation*, vol. 60, no. 1, pp. 36–43, 2012.

[38] M. Alibakhshikenari, B. S. Virdee, C. H. See, P. Shukla, S. M. Moghaddam, A. U. Zaman, S. Shafqaat, M. O. Akinsolu, B. Liu, J. Yang, R. Abd-Alhameed, F. Falcone, and E. Limiti, "Dual-polarized highly folded bowtie antenna with slotted self-grounded structure for sub-6 ghz 5g applications", *IEEE Transactions on Antennas and Propagation*, vol. 70, no. 4, pp. 3028–3033, 2022.

[39] E. Antonino-Daviu, M. Cabedo-Fabrés, M. Sonkki, N. M. Mohamed-Hicho, and M. Ferrando-Bataller, "Design guidelines for the excitation of characteristic modes in slotted planar structures", *IEEE Transactions on Antennas and Propagation*, vol. 64, no. 12, pp. 5020–5029, 2016.

[40] S. R. Emadian, C. Ghobadi, J. Nourinia, M. H. Mirmozafari, and J. Pourahmadazar, "Bandwidth enhancement of cpw-fed circle-like slot antenna with dual band-notched characteristic", *IEEE Antennas and Wireless Propagation Letters*, vol. 11, pp. 543–546, 2012.

[41] X. Liu, Y. Yin, P. Liu, J. Wang, and B. Xu, "A cpw-fed dual band-notched uwb antenna with a pair of bended dual-l-shape parasitic branches", *Progress in Electromagnetics Research*, vol. 136, pp. 623–634, 2013.

[42] M. Rahman and J. D. Park, "The smallest form factor uwb antenna with quintuple rejection bands for iot applications utilizing rsrr and rcsrr", *Sensors (Switzerland)*, vol. 18, no. 3, 2018.

[43] M. Rahman, W. T. Khan, and M. Imran, "Penta-notched uwb antenna with sharp frequency edge selectivity using combination of srr, csrr, and dgs", *AEU - International Journal of Electronics and Communications*, vol. 93, pp. 116–122, 2018.

[44] R. Fallahi, A. A. Kalteh, and M. G. Roozbahani, "A novel uwb elliptical slot antenna with band-notched characteristics", *Progress in Electromagnetics Research*, vol. 82, pp. 127–136, 2008.

[45] S. Yadav, A. K. Gautam, and B. K. Kanaujia, "Design of dual band-notched lamp-shaped antenna with uwb characteristics", *International Journal of Microwave and Wireless Technologies*, vol. 9, no. 2, pp. 395–402, 2017.

[46] G. Gao, B. Hu, L. He, S. Wang, and C. Yang, "Investigation of a reconfigurable dual notched uwb antenna by conceptual circuit model and time-domain characteristics", *Microwave and Optical Technology Letters*, vol. 59, no. 6, pp. 1326–1332, 2017.

[47] M. Nejatijahromi, M. Naghshvarianjahromi, and M. Ur Rahman, "Switchable planar monopole antenna between ultra-wideband and narrow band behavior", *Progress in Electromagnetics Research Letters*, vol. 75, pp. 131–137, 2018.

[48] M. Nejatijahromi, M. Naghshvarianjahromi, and M. Rahman, "Compact cpw fed switchable uwb antenna as an antenna filter at narrow-frequency bands", *Progress In Electromagnetics Research C*, vol. 81, pp. 199–209, 2018.

[49] M. Rahman, D. S. Ko, and J. D. Park, "A compact multiple notched ultra-wide band antenna with an analysis of the csrr-to-csrr coupling for portable uwb applications", *Sensors (Switzerland)*, vol. 17, no. 10, 2017.

[50] M. S. Shakhirul, M. Jusoh, Y. S. Lee, and C. R. Nurol Husna, "A review of reconfigurable frequency switching technique on micostrip antenna", vol. 1019, Institute of Physics Publishing, 2018, p. 012 042.

[51] M. R. Hamid, P. Gardner, P. S. Hall, and F. Ghanem, "Vivaldi antenna with integrated switchable band pass resonator", *IEEE Transactions on Antennas and Propagation*, vol. 59, no. 11, pp. 4008–4015, 2011.

[52] J. T. Bernhard, "Reconfigurable antennas", in *Synthesis Lectures on Antennas*, vol. 4, 2007, pp. 1–66.

[53] P. Lotfi, M. Azarmanesh, and S. Soltani, "Rotatable dual band-notched uwb/triple-band wlan reconfigurable antenna", *IEEE Antennas and Wireless Propagation Letters*, vol. 12, pp. 104–107, 2013.

[54] H. Jiang, M. Patterson, D. Brown, C. Zhang, K. Pan, G. Subramanyam, D. Kuhl, K. Leedy, and C. Cerny, "Miniaturized and reconfigurable cpw square-ring slot antenna loaded with ferroelectric bst thin film varactors", *IEEE Transactions on Antennas and Propagation*, vol. 60, no. 7, pp. 3111–3119, 2012.

[55] M. Sazegar, Y. Zheng, C. Kohler, H. Maune, M. Nikfalazar, J. R. Binder, and R. Jakoby, "Beam steering transmitarray using tunable frequency selective surface with integrated ferroelectric varactors", *IEEE Transactions on Antennas and Propagation*, vol. 60, no. 12, pp. 5690–5699, 2012.

[56] N. Apaydin, K. Sertel, and J. L. Volakis, "Nonreciprocal leaky-wave antenna based on coupled microstrip lines on a non-uniformly biased ferrite substrate", *IEEE Transactions on Antennas and Propagation*, vol. 61, no. 7, pp. 3458–3465, 2013.

[57] J. M. Bell, M. F. Iskander, and J. J. Lee, "Ultrawideband hybrid ebg/ferrite ground plane for low-profile array antennas", *IEEE Transactions on Antennas and Propagation*, vol. 55, no. 1, pp. 4–12, 2007.

[58] F. A. Miranda, F. W. Van Keuls, R. R. Romanofsky, C. H. Mueller, S. Alterovitz, and G. Subramanyam, "Ferroelectric thin films-based technology for frequency- and phase-agile microwave communication applications", *Integrated Ferroelectrics*, vol. 42, pp. 131–149, 2002.

[59] H. Xu, N. K. Pervez, and R. A. York, "Tunable microwave integrated circuits using bst thin film capacitors with device structure optimization", in *Seventeenth International Symposium on Integrated Ferroelectrics, ISIF-17*, vol. 77, pp. 27–35.

[60] C. J. Panagamuwa, A. Chauraya, and J. C. Vardaxoglou, "Frequency and beam reconfigurable antenna using photoconducting switches", *IEEE Transactions on Antennas and Propagation*, vol. 54, no. 2, pp. 449–454, 2006.

[61] S. Kawasaki and T. Itoh, "A slot antenna with electronically tunable length", in *Antennas and Propagation Society Symposium 1991 Digest*, 130–133 vol.1.

[62] N. Behdad and K. Sarabandi, "A varactor-tuned dual-band slot antenna", *IEEE Transactions on Antennas and Propagation*, vol. 54, no. 2, pp. 401–408, 2006.

[63] O. O. Tade, P. Gardner, and P. S. Hall, "Broadband matching of small antennas using negative impedance converters", in *Proceedings of the 2012 IEEE International Symposium on Antennas and Propagation*, 2012.

[64] C. Fan, B. Wu, Y. Hu, Y. Zhao, and T. Su, "Millimeter-wave pattern reconfigurable vivaldi antenna using tunable resistor based on graphene", *IEEE Transactions on Antennas and Propagation*, vol. 68, no. 6, pp. 4939–4943, 2020.

[65] Q. Zhou, X. Shao, P. Jiang, Z. Gao, C. Wang, and L. Shu, "An active learning metamodeling approach by sequentially exploiting difference information from variable-fidelity models", *Advanced Engineering Informatics*, vol. 30, no. 3, pp. 283–297, 2016.

[66] P. Jiang, Q. Zhou, and X. Shao, "Surrogate-model-based design and optimization", in *Springer Tracts in Mechanical Engineering*, Springer International Publishing, 2020, pp. 135–236.

[67] M. O. Akinsolu, B. Liu, V. Grout, P. I. Lazaridis, M. E. Mognaschi, and P. Di Barba, "A parallel surrogate model assisted evolutionary algorithm for electromagnetic design optimization", *IEEE Transactions on Emerging Topics in Computational Intelligence*, vol. 3, no. 2, pp. 93–105, 2019.

[68] B. Liu, H. Yang, and M. J. Lancaster, "Global optimization of microwave filters based on a surrogate model-assisted evolutionary algorithm", *IEEE Transactions on Microwave Theory and Techniques*, vol. 65, no. 6, pp. 1976–1985, 2017.

[69] M. O. Akinsolu, B. Liu, P. I. Lazaridis, K. K. Mistry, M. E. Mognaschi, P. D. Barba, and Z. D. Zaharis, "Efficient design optimization of high-performance mems based on a surrogate-assisted self-adaptive differential evolution", *IEEE Access*, vol. 8, pp. 80 256–80 268, 2020.

[70] B. Can and C. Heavey, "A comparison of genetic programming and artificial neural networks in metamodeling of discrete-event simulation models", *Computers and Operations Research*, vol. 39, no. 2, pp. 424–436, 2012.

[71] S. Grivet-Talocia and B. Gustavsen, *Passive macromodeling: Theory and applications*, ser. Passive Macromodeling: Theory and Applications. Wiley, 2015, pp. 1–872.

[72] J. W. Bandler, R. M. Biernacki, C. Shao Hua, P. A. Grobelny, and R. H. Hemmers, "Space mapping technique for electromagnetic optimization", *IEEE Transactions on Microwave Theory and Techniques*, vol. 42, no. 12, pp. 2536–2544, 1994.

[73] H. Schantz, *The art and science of ultrawideband antennas / hans schantz*, Second edition., ser. Ultrawideband antennas. Boston : Artech House, 2015, 2015.

[74] K. Wu, "Substrate integrated circuits (sics)–a new paradigm for future ghz and thz electronic and photonic systems", *IEEE Circuits and Systems Society Newsletter*, vol. 3, no. 2, p. 1, 2009.

[75] M. H. Bakr, "A hybrid aggressive space-mapping algorithm for em optimization", *IEEE Transactions on Microwave Theory and Techniques*, vol. 47, no. 12, pp. 2440–2449, 1999.

[76] M. H. Bakr, J. W. Bandler, R. M. Biernacki, S. Hua, and K. Madsen, "A trust region aggressive space mapping algorithm for em optimization", *IEEE Transactions on Microwave Theory and Techniques*, vol. 46, no. 12 PART 2, pp. 2412–2425, 1998.

[77] S. Amari and C. Ledrew, "Space-mapping optimization of planar coupled-resonator microwave filters", *IEEE Transactions on Microwave Theory and Techniques*, vol. 54, no. 5, pp. 2153–2159, 2006.

[78] S. Koziel and S. Ogurtsov, "Rapid design optimization of antennas using space mapping and response surface approximation models", *International Journal of RF and Microwave Computer-Aided Engineering*, vol. 21, no. 6, pp. 611–621, 2011.

[79] J. Ouyang, F. Yang, H. Zhou, Z. Nie, and Z. Zhao, "Conformal antenna optimization with space mapping", *Journal of Electromagnetic Waves and Applications*, vol. 24, no. 2-3, pp. 251–260, 2010.

[80] J. Zhu, J. W. Bandler, N. K. Nikolova, and S. Koziel, "Antenna optimization through space mapping", *IEEE Transactions on Antennas and Propagation*, vol. 55, no. 3 I, pp. 651–658, 2007.

[81] J. W. Bandler, R. M. Biernacki, S. H. Chen, R. H. Hemmers, and K. Madsen, "Electromagnetic optimization exploiting aggressive space mapping", *IEEE Transactions on Microwave Theory and Techniques*, vol. 43, no. 12, pp. 2874–2882, 1995.

[82] E. C. Robert, "Circuit theory for waveguiding systems", in *Foundations for Microwave Engineering*. IEEE, 2001, pp. 220–302.

[83] D. M. Pozar, *Microwave engineering*, Fourth edition. Hoboken, New Jersey : John Wiley and Sons, Incorporated, 2012.

[84] S. Boyd and L. Vandenberghe, *Introduction to applied linear algebra: Vectors, matrices, and least squares*. Cambridge: Cambridge University Press, 2018.

[85] G. Antonini, "Spice equivalent circuits of frequency-domain responses", *IEEE Transactions on Electromagnetic Compatibility*, vol. 45, no. 3, pp. 502–512, 2003.

[86] A. V. Oppenheim, *Signals and systems*, ser. Prentice-Hall signal processing series. Prentice-Hall, 1983.

[87] W.-K. Chen, *Broadband matching : Theory and implementations*, 3rd ed. World Scientific Publishing Company Pte Limited, 2016.

[88] Z. H. Hu, J. Kelly, C. T. P. Song, P. S. Hall, and P. Gardner, "Equivalent circuit modeling of chassis-antenna with two coupling elements", in *2010 IEEE International Symposium on Antennas and Propagation and CNC-USNC/URSI Radio Science Meeting - Leading the Wave, AP-S/URSI 2010*.

[89] Z. H. Hu, P. S. Hall, J. R. Kelly, and P. Gardner, "Uwb pyramidal monopole antenna with wide tunable band-notched behaviour", *Electronics Letters*, vol. 46, no. 24, pp. 1588–1590, 2010.

[90] G. Perez-Palomino, J. E. Page, M. Arrebola, and J. A. Encinar, "A design technique based on equivalent circuit and coupler theory for broadband linear to circular polarization converters in reflection or transmission mode", *IEEE Transactions on Antennas and Propagation*, vol. 66, no. 5, pp. 2428–2438, 2018.

[91] M. Li, L. Jiang, and K. L. Yeung, "Novel and efficient parasitic decoupling network for closely coupled antennas", *IEEE Transactions on Antennas and Propagation*, vol. 67, no. 6, pp. 3574–3585, 2019.

[92] Y. Bai and P. Gardner, "Surrogate model based on a novel approach and its application to a reconfigurable uwb antenna with tunable notched-band", *Submitted to IEEE Transactions on Antennas and Propagation*,

[93] C. Chiu, F. Xu, S. Shen, and R. D. Murch, "Mutual coupling reduction of rotationally symmetric multiport antennas", *IEEE Transactions on Antennas and Propagation*, vol. 66, no. 10, pp. 5013–5021, 2018.

[94] M. Arnold, C. Oikonomopoulos-Zachos, M. Geissler, and I. Wolff, "Applying the n-port network theory to match a symmetrical four-port antenna to a two-port source", *IEEE Transactions on Antennas and Propagation*, vol. 67, no. 5, pp. 2983–2991, 2019.

[95] L. A. Bronckers, A. Roc'h, and A. B. Smolders, "A new design method for frequency- reconfigurable antennas using multiple tuning components", *IEEE Transactions on Antennas and Propagation*, vol. 67, no. 12, pp. 7285–7295, 2019.